

# DNA Origami Structures as Versatile Platforms for Nanophotonics

**Doctoral thesis**

In fulfillment of the requirements for the degree

Doctor rerum naturalium (Dr. rer. Nat.)

In the scientific discipline “Physical Chemistry”

Submitted to the Faculty of Science

Of the University of Potsdam

by

**Youngeun Choi**

Potsdam, September 2018

1. Gutachter : Prof. Dr. Ilko Bald
2. Gutachter : Dr. Ute Resch-Genger
3. Gutachter : Dr. habil. Sébastien Bidault

Ort und Tag der Disputation : Potsdam, 05.12.2018

Published online at the  
Institutional Repository of the University of Potsdam:  
URN urn:nbn:de:kobv:517-opus4-421483  
<https://nbn-resolving.org/urn:nbn:de:kobv:517-opus4-421483>







# Abstract

Nanophotonics is the field of science and engineering aimed at studying the light-matter interactions on the nanoscale. One of the key aspects in studying such optics at the nanoscale is the ability to assemble the material components in a spatially controlled manner. In this work, DNA origami nanostructures were used to self-assemble dye molecules and DNA coated plasmonic nanoparticles. Optical properties of dye nanoarrays, where the dyes were arranged at distances where they can interact by Förster resonance energy transfer (FRET), were systematically studied according to the size and arrangement of the dyes using fluorescein (FAM) as the donor and cyanine 3 (Cy 3) as the acceptor. The optimized design, based on steady-state and time-resolved fluorometry, was utilized in developing a ratiometric pH sensor with pH-inert coumarin 343 (C343) as the donor and pH-sensitive FAM as the acceptor. This design was further applied in developing a ratiometric toxin sensor, where the donor C343 is unresponsive and FAM is responsive to thioacetamide (TAA) which is a well-known hepatotoxin. The results indicate that the sensitivity of the ratiometric sensor can be improved by simply arranging the dyes into a well-defined array. The ability to assemble multiple fluorophores without dye-dye aggregation also provides a strategy to amplify the signal measured from a fluorescent reporter, and was utilized here to develop a reporter for sensing oligonucleotides. By incorporating target capturing sequences and multiple fluorophores (ATTO 647N dye molecules), a reporter for microbead-based assay for non-amplified target oligonucleotide sensing was developed. Analysis of the assay using VideoScan, a fluorescence microscope-based technology capable of conducting multiplex analysis, showed the DNA origami nanostructure based reporter to have a lower limit of detection than a single stranded DNA reporter. Lastly, plasmonic nanostructures were assembled on DNA origami nanostructures as substrates to study interesting optical behaviors of molecules in the near-field. Specifically, DNA coated gold nanoparticles, silver nanoparticles, and gold nanorods, were placed on the DNA origami nanostructure aiming to study surface-enhanced fluorescence (SEF) and surface-enhanced Raman scattering (SERS) of molecules placed in the hotspot of coupled plasmonic structures.

# Zusammenfassung

Nanophotonik bezeichnet die Untersuchung von Licht in Wechselwirkung mit Materie im Nanometermaßstab. Die exakte Kontrolle über den Aufbau und die räumliche Anordnung der beteiligten Komponenten ist ein entscheidender Faktor für die Erforschung der Optik nanoskalierter Systeme. Eine mögliche Lösung bietet die selbstorganisatorische Eigenschaft von DNA-Origami-Nanostrukturen, die im Rahmen dieser Dissertation, insbesondere zur Kopplung verschiedener Farbstoffe bzw. plasmonisch aktiver Nanopartikel, verwendet wurden. Im ersten Teil dieser Dissertation wurden unterschiedliche Förster-Resonanzenergietransfer- (FRET) Farbstoff-Matrizen, bestehend aus Fluorescein (FAM) als FRET-Donor und Cyanine 3 (Cy 3) als FRET-Akzeptor, hergestellt und nachfolgend hinsichtlich des Einflusses ihrer Gesamtgröße und ihrer Anordnung *via* statischer und zeitaufgelöster Fluoreszenzspektroskopie untersucht. Daraufhin erfolgte die Weiterentwicklung der ermittelten optimalen Anordnung der Farbstoffe in einen ratiometrischen pH-Sensor, bestehend aus dem pH stabilen Coumarin 343 (C343) als FRET-Donor und dem pH sensitiven FAM als FRET-Akzeptor. Die erhaltenen Ergebnisse zeigten, dass sich die Sensitivität ratiometrischer Sensoren, insbesondere durch die wohldefinierte Anordnung der beteiligten Farbstoffe in der Matriz, deutlich steigern lassen. Selbige Anordnung konnte auch erfolgreich zur Entwicklung eines Giftstoffsensors, zum Nachweis des Hepatoxins Thioacetamid (TAA), verwendet werden.

Die Möglichkeit der Anordnung mehrerer Farbstoffe, unter Vermeidung ungewollter Farbstoff-Aggregation, ermöglicht außerdem die Verstärkung der Signale sogenannter Fluoreszenzreporter. Dies führte, im Rahmen dieser Arbeit, zur erfolgreichen Entwicklung eines auf Mikroperlen basierenden Oligonukleotid-Sensors, welcher ohne die Notwendigkeit einer vorherigen Zielverstärkung (z.B. durch Polymerase-Kettenreaktion) auskommt. Die anschließende Analyse mittels VideoScan, einer Multiplex-Analyse-Technik basierend auf der Fluoreszenzmikroskopie, ergab deutlich niedrigere Nachweisgrenzen für auf DNA-Origami basierende Reporter im Vergleich zu DNA-Einzelstrang basierenden Reportern.

Abschließend erfolgte die Verwendung der DNA-Origamis als Substrat für die präzise räumliche Anordnung verschiedener plasmonisch aktiver Nanopartikel zur Untersuchung des

optischen Verhaltens von Zielmolekülen im plasmonischen Nahfeld. Die Untersuchung der oberflächenverstärkten Fluoreszenz (SEF) und oberflächenverstärkten Raman-Streuung (SERS) von Molekülen im plasmonischer Hotspots erfolgte insbesondere mit Fokus auf den Einfluss der unterschiedlichen Anordnung von Gold-Nanostäbchen, Gold-Nanopartikel, und Silber-Nanopartikel.



# Contents

## Abbreviations

<b>1. Introduction</b> .....	1
<b>2. Theoretical Background</b> .....	4
<b>2.1. Structural DNA nanotechnology</b> .....	4
2.1.1. DNA.....	4
2.1.2. DNA nanostructures.....	5
2.1.3. DNA origami .....	6
<b>2.2. Fluorescence</b> .....	7
2.2.1. Theory of fluorescence .....	8
2.2.2. Theory of Förster Resonance Energy Transfer .....	9
2.2.3. Ratiometric sensing.....	12
<b>2.3. Microbead-based assays</b> .....	15
2.3.1. Microbeads.....	15
2.3.2. Detection schemes .....	16
<b>2.4. Plasmonics</b> .....	18
2.4.1. Optical properties of metals .....	18
2.4.2. LSPR of nanoparticles.....	19
2.4.3. Local Field Intensity Enhancement Factor (LFIEF).....	21
2.4.3. Coupled LSPR.....	22
2.4.2. Surface enhanced Raman scattering (SERS).....	23
2.4.3. Surface enhanced fluorescence (SEF).....	25
2.4.4. DNA assisted plasmonics .....	26
<b>3. Materials and methods</b> .....	29

<b>3.1. Materials and chemicals</b> .....	29
<b>3.2. Sample preparation</b> .....	32
<b>3.2.1. DNA origami nanostructure fabrication</b> .....	32
<b>3.2.2. Microbead preparation</b> .....	36
<b>3.2.3. AuNR synthesis</b> .....	37
<b>3.2.4. Nanoparticles and DNA</b> .....	39
<b>3.3. Methods</b> .....	42
<b>3.3.1. Steady-state fluorescence spectroscopy</b> .....	42
<b>3.3.2. Time-correlated single photon counting</b> .....	42
<b>3.3.3. VideoScan technology</b> .....	44
<b>3.3.4. Atomic force microscopy</b> .....	45
<b>3.3.5. Raman spectroscopy</b> .....	46
<b>3.3.6. UV-Vis extinction spectroscopy</b> .....	46
<b>3.3.7. Transmission electron microscopy (TEM)</b> .....	47
<b>4. Results</b> .....	48
<b>4.1. FRET nanoarrays and ratiometric sensing</b> .....	48
<b>4.1.1. FRET nanoarray analysis</b> .....	49
<b>4.1.2. Application as a ratiometric pH sensor</b> .....	55
<b>4.1.3. Application as ratiometric thioamide sensor</b> .....	60
<b>4.1.4. Conclusions</b> .....	65
<b>4.2. A new reporter design for microbead-based assay</b> .....	66
<b>4.2.1. Comparison of the two reporters</b> .....	67
<b>4.2.2. Proof-of-concept multiplex analysis</b> .....	68
<b>4.2.3. Strategies to improve the measured signal</b> .....	70
<b>4.2.4. Conclusion</b> .....	74
<b>4.3. DNA coated metal nanoparticles with tailored optical properties</b> .....	75

4.3.1. AuNP and AgNP dimers on DNA origami nanostructure .....	75
4.3.1. AuNRs .....	82
4.3.3. Conclusion .....	89
5. Conclusion and Outlook .....	91
Bibliography .....	96
Appendix .....	107
Acknowledgements	





# Abbreviations

$E_0$	intensity of the incoming field
$F_{D\lambda}(\lambda)$	donor fluorescence at each wavelength interval unit
$I_L$	laser intensity
$P_i$	geometrical depolarization factor
$\hat{a}$	acceptor absorption transition moment
$\hat{d}$	donor emission transition moment
$\hat{r}$	donor-acceptor connection line
$\varepsilon_M$	dielectric constant of the medium
$\theta_A$	angle between the acceptor absorption transition moment
$\theta_D$	angle between the donor emission transition moment
$\theta_T$	angle between $\hat{d}$ and $\hat{a}$
$\kappa^2$	orientation factor (0 – 4)
$\sigma_0$	standard deviation of blank
$\sigma_{ads}^R$	Raman cross section of molecules adsorbed on the metal surface
$\epsilon_\lambda$	extinction coefficient at given wavelength $\lambda$
A	adenine
A	absorption
a	radius of the particle
A'	slope of calibration curve
AA	acetic acid
Ac	acceptor
AFM	atomic force microscopy
Ag	silver
AgNP	silver nanoparticle
$A_{ovlp}$	area of overlap
AR	aspect ratio

$A_{\text{tot}}$	total area
Au	gold
AuNP	gold nanoparticle
AuNR	gold nanorod
$B$	intercept of calibration curve
BSPF	bis( <i>p</i> -sulfonatophenyl)phenylphosphine
Bt	biotin
$c$	concentration
C	cytosine
C343	coumarin 343
CI	Coulombic interaction
CTAB	cetyltrimethylammonium bromide
cy3	cyanine 3
DNA	deoxyribonucleic acid
<i>DNA origami<sub>R</sub></i>	DNA origami nanostructure based reporter
Do	donor
Do*	excited donor
dsDNA	double stranded DNA
DTT	dithiothreitol
$E$	FRET efficiency
EC50	half maximal effective concentration
EDTA	ethylenediaminetetraacetic acid
EF <sub>F</sub>	enhancement factor for fluorescence
ESIPT	excited state intramolecular proton transfer
FAM	fluorescein
$f_D(\lambda)$	normalized fluorescence spectrum of the donor
FRET	Förster resonance energy transfer
G	guanine
HOMO	highest occupied molecular orbital

IC	internal conversion
$Im(\varepsilon(\lambda))$	imaginary part of the dielectric function
IR	internal relaxation
ISC	intersystem crossing
$J$	spectral overlap integral
$k_D$	emission rate constant of the donor
$k_F$	energy transfer rate constant for FRET
$k_{nr}$	the rate of non-radiative de-excitation
$k_r$	rate of radiative de-excitation
LFIEF	local field intensity enhancement factor
LoD	limit of detection
LoQ	limit of quantification
LSPR	localized surface plasmon resonance
LUMO	lowest unoccupied molecular orbital
miRNA	micro RNA
MW	molecular weight
$n$	refractive index of the medium
N	number of molecules
$N_A$	Avogadro's constant
nb	nucleobase
NSET	nanometal surface energy transfer
PCR	polymerase chain reaction
PEPY	phenylethynylpyrene
PET	photoinduced electron transfer
PMMA	polymethylmethacrylat
PS	polystyrene
$r$	distance between the donor and the acceptor
$R_0$	Förster distance
$Re(\varepsilon(\lambda))$	real part of the dielectric function

RNA	ribonucleic acid
RT	room temperature
$S_0$	electronic ground state
$S_1, S_2$	singlet excited states
SDS	sodium dodecyl sulfate
SEF	surface enhanced fluorescence
SERS	surface enhanced Raman scattering
SPR	surface plasmon resonance
ssDNA	single stranded DNA
<i>ssDNA_R</i>	ssDNA reporter
T	thymine
$T_1, T_2$	triplet excited states
TAA	thioacetamide
TAE	Tris-acetate-EDTA
TAMRA	carboxytetramethylrhodamine
TEM	transmission electron microscopy
TICT	twisted intramolecular charge transfer
$\nu$	frequency
$\Phi$	quantum yield
$\Phi_D$	quantum yield for the donor in the absence of the acceptor
$\epsilon_A(\lambda)$	molar extinction coefficient of the acceptor
$\lambda$	wavelength of the light
$\lambda'_{\text{emi}}$	maximum emission wavelength
$\lambda_{\text{abs}}$	maximum absorption wavelength
$\lambda_{\text{emi}}$	emission wavelength recorded for time-resolved fluorescence data
$\lambda_{\text{exc}}$	excitation wavelength
$\tau_D$	fluorescence lifetime of the donor in the absence of the acceptor
$\tau_{DA}$	fluorescence lifetime of the donor in the presence of the acceptor
$\tau_s$	fluorescence decay time

$\omega$	angular frequency
$E(z, \omega)$	electric field amplitude at the surface of the metal particle
$l$	optical path length
$n(\omega)$	refractive index
$p$	dipolar polarizability
$\alpha$	polarizability tensor
$\varepsilon(\omega), \varepsilon(\lambda)$	dielectric function
$\eta$	radiative efficiency
$\kappa'$	shape factor



# 1. Introduction

In 1959, physicist Richard Feynman introduced to the world the ideas and concepts behind nanotechnology, when he gave his famous talk at the American Physical Society meeting at the California Institute of Technology <sup>1</sup>. A decade later, Professor Norio Taniguchi coined the term nanotechnology <sup>2</sup>. Finally in 1981 with the development of the scanning tunneling microscope, individual atoms could be 'seen' and thus began the field of modern nanotechnology <sup>3</sup>. Nanotechnology is therefore defined as the science, engineering and technology conducted at the nanoscale, which is approximately between 1 nm and 100 nm. Nanotechnology has now become a part of our everyday life ranging from fast computers, lab-on-a-chip point of care diagnostics, nanoparticles in sunscreen, to name but a few.

Nanomaterials exhibit properties that are different from bulk materials and single atoms or molecules, with exceptional chemical and physical properties. Manufacturing at the nanoscale is done either in a top-down or bottom-up approach. Top-down fabrication reduces large pieces of materials down to the nanoscale, usually involving photolithography or nanoimprint lithography techniques. This approach however requires the use of costly equipment and suffers from low throughput <sup>4,5</sup>. The bottom-up approach on the other hand creates products by building them up from atoms and molecules, eliminating the need for expensive equipment and making the scaling-up process potentially straightforward <sup>4</sup>. Nevertheless, the most attractive approach is based on self-assembly methods, of which DNA-based self-assembly has attracted incredible interest due to its specific base pairing that occurs naturally <sup>6</sup>.

DNA nanotechnology, first introduced by Nadrian Seeman in 1982 <sup>7</sup> and later revolutionized by Paul Rothemund in 2006 <sup>8</sup>, utilizes the self-assembling nature of DNA to create two-dimensional and three-dimensional DNA origami nanostructures <sup>9</sup>. In the latter technique, a long circular DNA single strand (the 'scaffold strand') is folded into arbitrary structures *via* short DNA single strands (the 'staple strands'). This technique is particularly attractive as these

short strands can be addressed individually, which makes it possible to arrange different chemical moieties such as dye molecules, and even plasmonic nanoparticles with nanoscale spatial control, allowing one to study optical properties of molecules in the nanoscale.

Fluorescence is a widely used technique for detection of analytes in life and material sciences due to the ease of use, sensitivity down to the single molecule level, as well as suitability for *in vitro* and *in vivo* imaging<sup>10,11</sup>. This has encouraged many developments towards a more sensitive and brighter fluorescent reporter, and a common method to achieve this is by using multichromophore based strategies. However, in developing such multichromophore reporters it is necessary to construct systems where fluorescence diminishing dye-dye interactions, such as H-type dimers and aggregates<sup>12,13</sup>, can be avoided. The analyte selectivity of such a fluorescent reporter can be provided by different approaches; a) by the fluorescent dye molecule that is responsive to the analyte of interest such as fluorescein (FAM) which is a pH sensitive fluorophore<sup>14</sup>, as well as toxins such as thioacetamide (TAA)<sup>15</sup>, or b) by target recognizing sites such as DNA or microRNA (miRNA) that has a complementary sequence to the target oligonucleotide. A powerful technique to address these aspects of developing a sensor is the DNA origami technology. It provides both the ability to place dye molecules close enough to synthesize a nanoscale multichromophore system but also far enough to avoid dyes from forming aggregates. In addition, DNA target recognition sites can be easily incorporated into the structure by extending the short staple strands with target complementary sequences.

In this work, the programmability of DNA origami nanostructures has been extensively utilized to study nanophotonics, both for fluorescence and plasmonics, and to develop nanoscale multichromophore sensors for biologically relevant molecules. Firstly, analysis of Förster-resonance energy transfer (FRET)-based nanoarrays according to the size and dye pattern and their application as ratiometric sensors are discussed in section 4.1. The distance-dependent nature of FRET prompted development of many analytical tools for sensing, in particular, biologically relevant molecules<sup>16,17</sup>. Here, FRET is utilized in developing a self-referenced ratiometric sensor as it provides dual wavelengths based on donor emission and acceptor emission where the acceptor emission is analyte-responsive<sup>18</sup>. This eliminates the analyte-independent signal distortions that are often a limiting factor for single-wavelength emission based fluorescent reporters<sup>19</sup>. By selectively arranging a multichromophore nanoarray of the FRET pairs on the DNA origami nanostructure, not only could the overall fluorescence signal



be enhanced but increase in the emission intensity ratio of donor to acceptor <sup>20,21</sup> and enhanced FRET efficiency <sup>22</sup> could be utilized for this novel ratiometric sensor.

As mentioned earlier, target oligonucleotide specificity can be incorporated into the DNA origami nanostructure, as staple strands can be extended with target specific sequences (section 4.2). Commonly, miRNA profiling methods require amplification of the targets which could introduce errors and lead to false results <sup>23</sup>. Therefore, establishing strategies to increase the reporter signal is a key step in developing a sensor that bypasses this target amplification step. Strategies were therefore explored to develop a reporter for microbead-based assays, where the emission signal generated by multiple fluorophores on the DNA origami nanostructure is referenced back to the fluorescence emission from the microbeads <sup>24</sup>.

In addition to developing fluorescence sensors, utilizing the spatial addressability of DNA origami nanostructures allows for studies of plasmonic nanostructures (section 4.3). When plasmonic nanostructures interact with light, the local electromagnetic field is enhanced which influences near-field optical processes leading to effects such as surface enhanced Raman scattering (SERS) <sup>25</sup> and surface enhanced fluorescence (SEF) <sup>26</sup>. The placement of metal nanoparticles and analytes can be achieved through the use of DNA origami nanostructures <sup>27,28</sup>. Especially interesting are structures where the analyte is sandwiched between metal nanoparticles, as the electromagnetic field enhancement at this site is extraordinarily high <sup>29</sup>. Here, plasmonic substrates such as gold nanoparticles, silver nanoparticles, and gold nanorods, are arranged on DNA origami nanostructures to observe optical properties of molecules in the vicinity of the surface of these particles.

## 2. Theoretical Background

### 2.1. Structural DNA nanotechnology

Our understanding of DNA has been revolutionized in 1953 by James Watson and Francis Crick<sup>30</sup>. Based on experimental data obtained by Rosalind Franklin<sup>31</sup>, they proposed the double helix structure providing us the chemical basis to understand the unique interactions between the DNA molecules. Structural DNA nanotechnology was founded upon these unique interactions, where DNA molecules can be used as building blocks to assemble larger and more complex nanoscale structures<sup>32</sup>. The first concepts were introduced by Seeman in 1982<sup>7</sup>, and in 2006 Rothemund introduced the DNA origami technique<sup>8</sup> which led to a huge leap in the development of this field.

#### 2.1.1. DNA

DNA is a polymer that encodes biological information of an organism. The repeating monomers of this polymer chain are called nucleotides that are made up of three primary components: a nitrogen-containing nucleobase (nb), a carbon-based deoxyribose, and a phosphate group. The deoxyribose unit contains five carbons arranged in a ring, of which 1' carbon is attached to the nucleobase, and 5' and 3' carbons to the phosphate groups (5'- and 3' end, respectively) *via* phosphodiester bonds (Figure 2.1). The resulting structure is a single stranded DNA (ssDNA) with a negatively charged sugar-phosphate backbone and a directionality. The genetic information of an organism is stored *via* the sequence of the nucleotides, deriving from this directionality, with each sequence characterized by four different nucleobases: adenine (A), cytosine (C), guanine (G) and thymine (T).

Two antiparallel ssDNA can selectively hybridize to form one double stranded DNA (dsDNA) strand *via* nucleobase pairing named Watson-Crick base pairing (Figure 2.1)<sup>30</sup>. Here, A binds

## 2. Theoretical background

to T via two hydrogen bonds and C to G via three hydrogen bonds. If the two single strands are complementary, a double helix can be formed. The most common form of dsDNA in physiological solutions is the right-handed double helix (B-DNA) with a diameter of 2 nm, a distance of 0.34 nm between each nb, and a full helical twist every 10.5 nb of approximately 3.5 nm in length. The helical structure is stabilized dominantly through  $\pi$ - $\pi$  stacking interactions between the nbs through attractive Van der Waals forces <sup>33</sup>. A fine balance between the electrostatic repulsion between the negatively charged phosphate groups, entropy loss from conformational rigidity, base stacking interactions, and Watson-Crick hydrogen bonding allows for the double helix to retain its unique structure.

### 2.1.2. DNA nanostructures

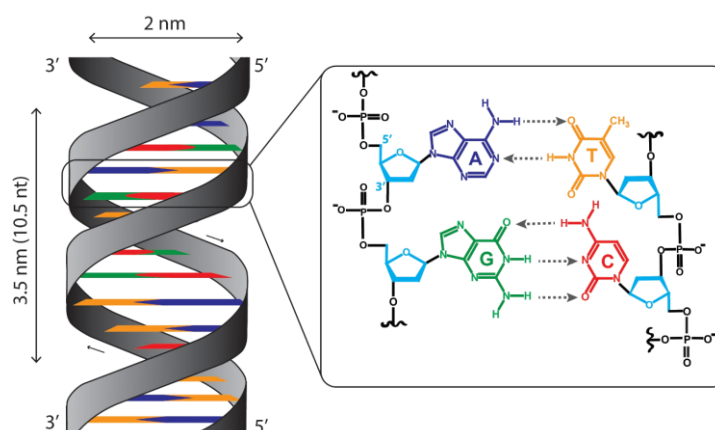


**Figure 2.1.:** Schematic representation of the B-DNA and chemical structure of the Watson-Crick base pairs, with hydrogen bonds shown in grey arrows. The phosphate group is shown in black, the sugar ring is shown in light blue with the four different nucleobases in different colors (A: adenine, T: thymine, G: guanine, C: cytosine).

Based on the specific interaction between the base pairs, DNA strands are glued together to construct DNA nanostructures. Two main design strategies are used for the fabrication: DNA tile and the DNA origami. The first DNA tile was reported by Seeman and Kallenbach <sup>34</sup>, named immobile four-way junction, which was constructed using four ssDNA strands. The structure mimics the naturally existing Holliday junction <sup>7</sup>, but is stabilized by reducing repeating sequences within the junction and thus preventing the branching point from migrating along the strand. From here, junctions with higher branches (three-, five-, six-, eight-, and 12- way junctions) have been constructed using similar principles <sup>35-37</sup>. However, it was not until the rigid DNA double-crossover (DX) structures were proposed <sup>38</sup> that higher order structures of DNA tiles could be assembled. The first example of a two dimensional (2D) DNA crystal

## 2.1. Structural DNA nanotechnology

structure was fabricated by introducing sticky ends (unbound ssDNA) to the DNA tiles<sup>39</sup>. The DNA tile technique provided a method to fabricate various higher-order DNA nanostructures<sup>40–42</sup> as well as three-dimensional DNA crystals<sup>43–45</sup>.

### 2.1.3. DNA origami

Although DNA nanostructures were created since the early 1980s, the complexity involved in creating the structures hindered the field to move forward. These early structures were constructed using multiple short DNA strands that were precisely engineered, and required specific stoichiometry as well as numerous reactions and purification steps. Furthermore, construction of arbitrary structures with well-defined geometry was not possible as they produced highly periodic and symmetric structures<sup>8</sup>. These limitations were overcome by using a long ssDNA instead of multiple short DNA strands<sup>46</sup>. Inspired by this discovery, Rothemund developed the DNA origami technique (published in 2006)<sup>8</sup>, which was a major turning point in structural DNA nanotechnology. In a folding process of DNA origami nanostructures, a long ssDNA (scaffold DNA) is folded into arbitrary shapes through self-assembly, by hundreds of short synthetic ssDNAs (staple strands) of 20-60 nbs. Each staple strand is designed to bind to different sites along the scaffold, which collectively folds the circular shaped scaffold into the desired geometry. By using commercially available M13mp18 bacteriophage (circular ssDNA with ~ 7,000 nbs) with a known sequence, and short artificial staple strands, the necessity to precisely engineer randomized DNA sequences was eliminated. A schematic representation of the self-assembled folding process of a triangular DNA origami nanostructure is shown in Figure 2.2.

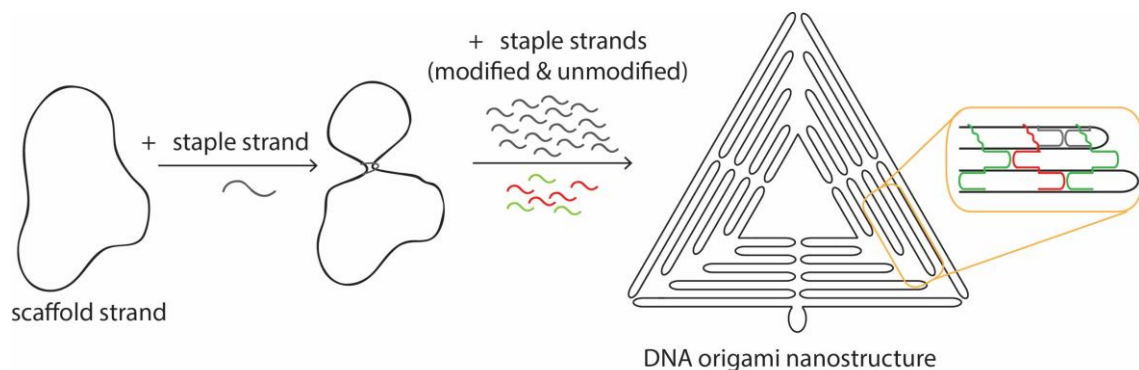


**Figure 2.2.:** Illustration of the folding process of a DNA origami nanostructure. Short staple strands glue together the circular scaffold strand into arbitrary shapes, in this case a triangular DNA origami nanostructure based on the design by Rothemund<sup>5</sup>. Desired functionalities can be introduced to the structure *via* replacing certain staple strands during the folding process.

DNA origami design programs such as *Tiamat*<sup>47</sup>, *SARSE*<sup>48</sup>, and *caDNAo*<sup>49</sup> can generate staple strand sequences according to the shape desired by the user. As such, the position of each staple strand is known, allowing the DNA origami nanostructure to be thought of as a nanoscale pegboard. Each end of the staple strand is addressable and can be modified with a variety of chemical moieties (NH<sub>2</sub>-, SH-, biotin-, alkyne etc.), organic dye molecules, and extra nucleotides to use as ssDNA overhangs that protrude from the DNA origami plane. This functional versatility and spatial addressability make DNA origami a great platform to be utilized for numerous applications. Just to name a few of the applications, nanoscopic rulers for super resolution microscopy were developed by labeling DNA origami with fluorescent dyes at specific distances<sup>50</sup>, a new single molecule fluorescence technique termed DNA-PAINT (DNA-point accumulation for imaging in nanoscale topography) was developed using the rate of association and dissociation of the oligos on extended staples<sup>51</sup>, complex Förster resonance energy transfer (FRET) constructs were assembled to study energy pathways from donor molecule to the acceptor molecule<sup>20,21,52</sup>, ion sensors were developed using G-quadruplex structures on DNA origamis<sup>17</sup>, DNA damage towards electron and UV radiations were visualized using biotin modified staples *via* presence or absence of bound streptavidin molecules<sup>53–55</sup>, plasmonic nanostructures were assembled and used for highly sensitive surface-enhanced Raman scattering (SERS)<sup>27,56,57</sup> substrates as well as surface-enhanced fluorescence (SEF)<sup>58,59</sup>.

## 2.2. Fluorescence

Sir George Gabriel Stokes published a hallmark paper in 1852, in which he reported that the wavelength of dispersed light is always longer than that of the original light<sup>60</sup>. This became later the Stoke's Law and eventually he termed this phenomenon fluorescence<sup>61</sup>. Since its discovery, the application of fluorescence has been highly versatile and has even become nowadays the method of choice in studying biological phenomena by spectroscopy or imaging, as well as detection of biomolecules<sup>10</sup>. Such preferential selection is attributed to its ease of use, stability, nanoscale resolution, and sensitivity down to the single-molecule level<sup>11,62</sup>.

## 2.2. Fluorescence

### 2.2.1. Theory of fluorescence

Light absorption by a substance induces electronic excitation of the molecule, followed by multiple de-excitation processes that can be categorized into radiative and non-radiative processes<sup>63</sup>. Radiative processes, termed luminescence, include fluorescence and phosphorescence according to the lifetime of their excited state. Non-radiative processes include internal conversion (IC), internal relaxation (IR), and intersystem crossing (ISC). All the different processes that follow light absorption can be visualized in a Jablonski diagram as illustrated in Figure 2.3.

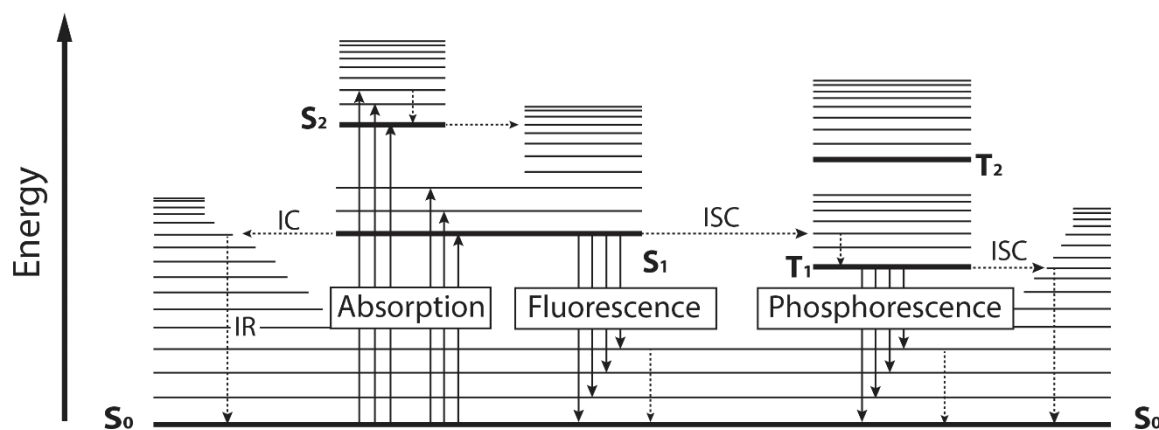


**Figure 2.3.:** Jablonski diagram illustrating the electronic transitions. Solid arrows depict radiative processes (absorption, fluorescence, phosphorescence) and dashed arrows are non-radiative processes (internal relaxation (IR), internal conversion (IC), and intersystem crossing (ISC) ( $S_0$  : singlet ground state,  $S_1$  and  $S_2$  : singlet excited state,  $T_1$  and  $T_2$  : triplet excited state).

The singlet electronic states are  $S_0$  (electronic ground state),  $S_1$ ,  $S_2$ ,... and the triplet states are  $T_1$ ,  $T_2$ ,.... Electronic transitions occur without significant displacement of the nuclei according to the Born Oppenheimer approximation. This way the transitions occur vertically ( $< 10^{-15}$  s), which is described by the Franck-Condon principle.

When a molecule is excited to an energy level higher than  $S_1$  (e.g.,  $S_2$  at higher vibrational levels), vibrational relaxation towards the lowest vibrational state occurs (internal relaxation, IR) which is then followed by a non-radiative IC ( $10^{-14} - 10^{-10}$  s) to  $S_1$ . From here, further IR ( $10^{-12} - 10^{-10}$  s) can occur to relax the molecule towards the 0 vibrational level of the  $S_1$  singlet state. From  $S_1$  there can be IC to  $S_0$  as well, but since this has a much larger energy gap than that between  $S_2$  to  $S_1$  it is therefore much less efficient. Emission of photons due to de-excitation of  $S_1 \rightarrow S_0$  is called fluorescence. As fluorescence emissions (for typical organic

## 2. Theoretical background

dyes:  $10^{-9} - 10^{-7}$  s) occur mainly from the vibrational ground state of  $S_1$ , the excitation wavelength does not influence the emission spectrum (Kasha's Rule). Fluorescence emission occurs at higher wavelength than that of the absorbed light due to the energy loss in the excited state *via* vibrational relaxation (Stokes shift). It should be noted that a small fraction of light can be emitted at shorter wavelengths than the absorbed light. This is due to a small fraction of the molecules being in a higher vibrational state of  $S_0$  at room temperature (Boltzmann Law). Another de-excitation process that can occur is the ISC from  $S_1$  to  $T_1$ . ISC ( $10^{-10} - 10^{-8}$  s) is a non-radiative process and can take place between two isoenergetic vibrational levels of a singlet state to a triplet state e.g.,  $S_1 \rightarrow T_1$ . From here, through IR the molecules relax from a higher vibrational level to the vibrational ground state of  $T_1$ . This can be followed by radiative de-excitation to  $S_0$ , which is termed phosphorescence ( $10^{-3} - 10^2$  s).

Two of the most important characteristics of a fluorescent molecule are fluorescence decay time and quantum yield. Quantum yield ( $\phi$ ) is the relative number of emitted photons compared to that of the absorbed photons and is given by,

$$\phi = \frac{k_r}{k_r + k_{nr}}, \quad (2.1)$$

where  $k_r$  is the rate of the radiative de-excitation and  $k_{nr}$  the rate of non-radiative de-excitation.

The average time that the molecule spends in the excited state before de-activation down to ground state is called fluorescence decay time ( $\tau_s$ ) and is defined using equation 2.2,

$$\tau_s = \frac{1}{k_r + k_{nr}}. \quad (2.2)$$

### 2.2.2. Theory of Förster Resonance Energy Transfer

In addition to all the intramolecular de-excitation pathways described above, other intermolecular de-excitation pathways exist where the energy from the excited molecule (donor) is transferred to a second molecule (acceptor). If the donor (Do) and the acceptor (Ac) are chemically different, this is called heterotransfer and can only occur if the emission spectrum of Do overlaps partially with the absorption spectrum of Ac. If, on the other hand, the energy transfer occurs between identical molecules, this is called homotransfer. This energy transfer can either be radiative or non-radiative. Radiative transfer is a two-step process where the photon emitted by a Do is absorbed by an Ac (or Do in case of

## 2.2. Fluorescence

homotransfer), and occurs when the distance between Do and Ac is larger than the wavelength of the emitted light and depends on the spectral overlap as well as the concentration. A non-radiative process on the other hand does not involve the emission of the photon from the Do, but requires some interaction between the Do and Ac as well as the spectral overlap. Of particular interest is the Förster resonance energy transfer (FRET) process. FRET is a long-range dipole-dipole interaction and is efficient in the ranges 1 nm to 10 nm for organic chromophores (Figure 2.4).

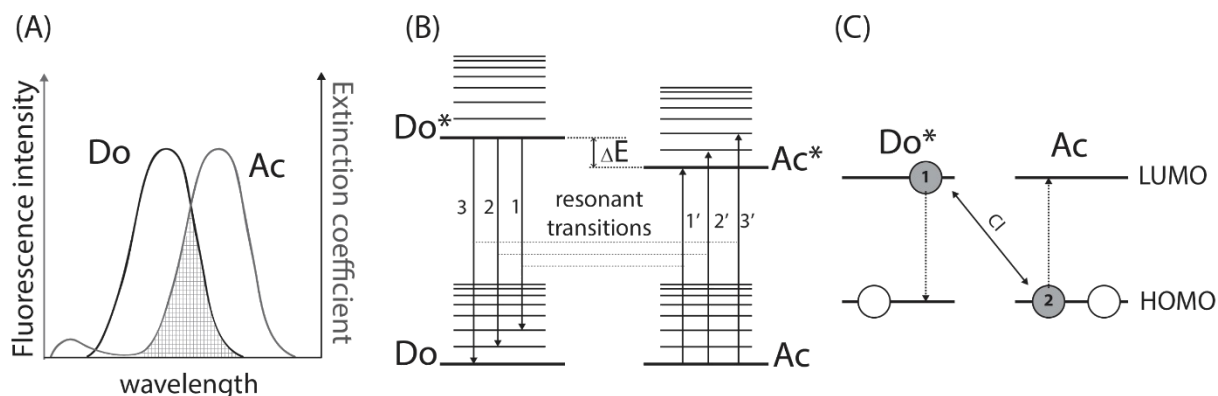


**Figure 2.4.:** Schematic representation of a few pre-requisites for FRET. (A) Illustration of the overlap between the emission spectrum of the donor Do and the absorption spectrum of Ac. (B) Energy level scheme of Do and Ac with several vibrational transitions of Do practically the same as the corresponding transitions in Ac (resonant transitions). (C) Coulomb interaction (CI) between excited Do (Do\*) and Ac allows for FRET (LUMO; lowest unoccupied molecular orbital, HOMO; highest occupied molecular orbital).

The energy transfer rate constant  $k_F$  for FRET was derived from classical and quantum-mechanical grounds and can be expressed as,

$$k_F = k_D \left[ \frac{R_0}{r} \right]^6 = \frac{1}{\tau_D} \left[ \frac{R_0}{r} \right]^6, \quad (2.3)$$

where  $k_D$  is the emission rate constant of the Do, and  $\tau_D$  the lifetime of the Do in the absence of the acceptor,  $r$  the distance between the donor and the acceptor, and  $R_0$  the Förster distance. Förster distance is the distance at which the spontaneous decay and transfer of the excited donor are equally probable ( $k_F = k_D$ ).

$R_0$  can be determined from spectroscopic data and is given by,

$$R_0^6 = \frac{9(\ln 10)\kappa^2\Phi_D J}{128\pi^5 n^4 N_A}, \quad (2.4)$$



## 2. Theoretical background

where  $\kappa^2$  is the dipole orientation factor,  $\Phi_D$  the quantum yield for the donor in the absence of the acceptor,  $J$  the spectral overlap integral,  $n$  the refractive index of the medium, and  $N_A$  the Avogadro's constant (here, it is  $6.0221415 \times 10^{23} \text{ mol}^{-1}$ )<sup>64</sup>.

The overlap integral calculated using wavelength can be defined as,

$$J = \int f_D(\lambda) \varepsilon_A(\lambda) \lambda^4 d\lambda, \quad (2.5)$$

where  $\lambda$  is the wavelength of the light usually expressed in nanometers,  $\varepsilon_A(\lambda)$  is the molar extinction coefficient of the acceptor usually expressed in  $\text{M}^{-1} \text{ cm}^{-1}$ , and  $f_D(\lambda)$  is the normalized fluorescence spectrum of the Do (on the wavelength scale) and can be expressed as,

$$f_D(\lambda) = \frac{F_{D\lambda}(\lambda)}{\int F_{D\lambda}(\lambda) d\lambda}, \quad (2.6)$$

where  $F_{D\lambda}(\lambda)$  is the donor fluorescence at each wavelength interval unit.

The orientation factor  $\kappa^2$  in equation 2.4 can be defined as,

$$\kappa^2 = (\cos \theta_T - 3 \cos \theta_D \cos \theta_A)^2, \quad (2.7)$$

where  $\theta_D$  is the angle between the donor emission transition moment ( $\hat{d}$ ) and the donor-acceptor connection line ( $\hat{r}$ ),  $\theta_A$  is the angle between the acceptor absorption transition moment ( $\hat{a}$ ) and the donor-acceptor connection line, and  $\theta_T$  is the angle between the donor emission and acceptor absorption transition moments.  $\kappa^2$  values range from 0 and 4, with an average value of 2/3 when molecules are free to rotate at a rate much faster than the de-excitation rate of the Do<sup>63</sup> (Figure 2.5 (A), (B)).

Lastly, FRET efficiency  $E$  is defined as,

$$E = \frac{R_0^6}{R_0^6 + r^6}, \quad (2.8)$$

and  $E$  is 50 % when  $r$  is equal to  $R_0$  (Figure 2.5 (C)). The efficiency can also be written in the following form,

$$E = 1 - \frac{\tau_{DA}}{\tau_D}, \quad (2.9)$$

## 2.2. Fluorescence

where  $\tau_{DA}$  and  $\tau_D$  are the donor excited-state lifetimes in the presence and absence of the acceptor, respectively.

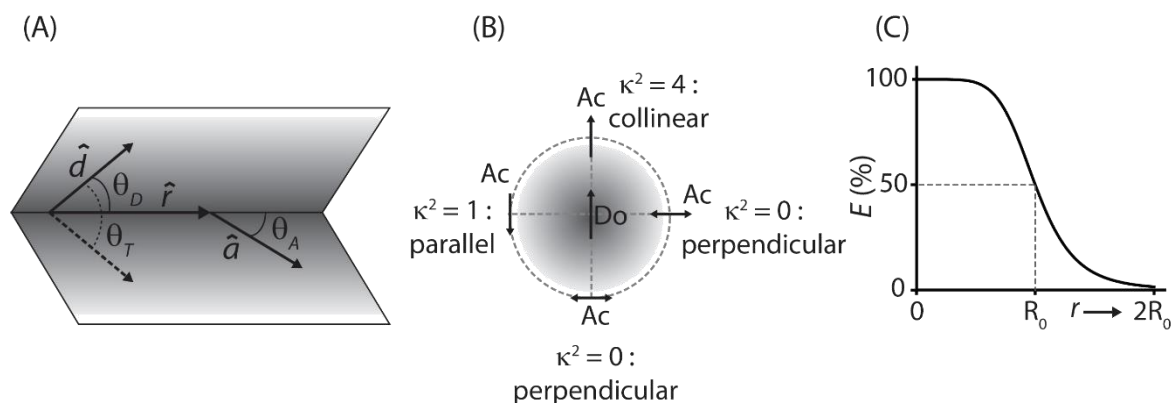


**Figure 2.5.:** (A) Schematic representation of angles and transition moments and angles involved in the definition of the orientation factor ( $\kappa^2$ ). (B) Example values of  $\kappa^2$  ranging from 0 to 4. If molecules are free to rotate,  $\kappa^2$  is 2/3. (C) FRET efficiency  $E$  as a function of  $r$ , with  $E = 50\%$  when  $r = R_0$ .

### 2.2.3. Ratiometric sensing

As mentioned in the introductory section of this chapter, fluorescence-based sensing is the method of choice for biological sciences these days. However, detection methods relying on single emission intensity has some significant drawbacks due to analyte-independent signal modifications, especially if a fluorophore is used as a probe. Some of these drawbacks include self-quenching, photobleaching, light scattering, auto fluorescence from biological samples, and other changes in the emission intensity due to the local environment of the dye <sup>65</sup>. To overcome such factors, ratiometric sensing can be utilized where the fluorescence intensities of two wavelengths is simultaneously recorded and their ratio is used rather than the intensity of single emission. Different methods of ratiometric sensing exist such as dual wavelength probes based on a single fluorophore, or energy transfer mechanisms between two different fluorophores <sup>66</sup>.

Ratiometric sensing based on a single emitter can be observed by shifts in the excitation or emission spectra, or the change of relative intensities of two or more bands. In order for the latter ratiometric sensing to be possible, spectrally recognizable ground state and/or excited state forms must exist as well as the switching between these forms must happen. Switching between fluorescent and phosphorescent emission <sup>67</sup> can be used for ratiometric sensing as the Stokes shift is strong (Figure 2.3). Other single emitter ratiometric sensors include

## 2. Theoretical background

ICT-based<sup>68</sup>, twisted intramolecular charge-transfer (TICT)-based<sup>69</sup>, and inhibition of excited state intramolecular proton transfer (ESIPT)-based ratiometric sensing<sup>70,71</sup>, where the resulting spectral shifts are sufficient to clearly distinguish between the two emission bands (Figure 2.6)<sup>72</sup>.

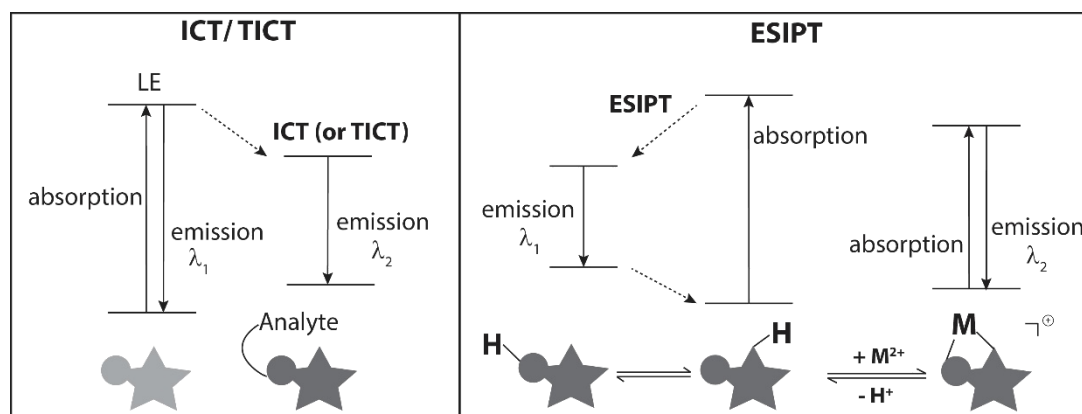


**Figure 2.6.:** Ratiometric sensors based on single emitters. In ICT-based ratiometric sensing, binding of an analyte to the fluorophore leads to switching from locally excited (LE) to ICT state thus leading to two different emission wavelengths. This is similar to the TICT-based sensing as the binding of analyte leads to a change in the geometry of the fluorophore, generating a TICT state. In ESIPT-based ratiometric sensing, the inhibition of ESIPT *via* chelating of the metal ion results in a different emission wavelength than that without the metal ion.

The best known single fluorophore ratiometric sensors are pH sensors with both dual emission and excitation properties such as benzoxanthene dyes<sup>73–75</sup>, and fura-2 and indo-1 for Ca<sup>2+</sup> sensing<sup>76,77</sup> where the ground state ICT is modulated by the binding of the ion.

When two different fluorophores are used, the hetero-FRET mechanism is exploited. The most common strategies to detect analytes include the use of a conformational change between the two fluorophores<sup>78,79</sup>, splitting of the linker between the fluorophores<sup>80</sup>, and analyte binding induced modulation of FRET efficiency<sup>81</sup> (Figure 2.7).

## 2.2. Fluorescence

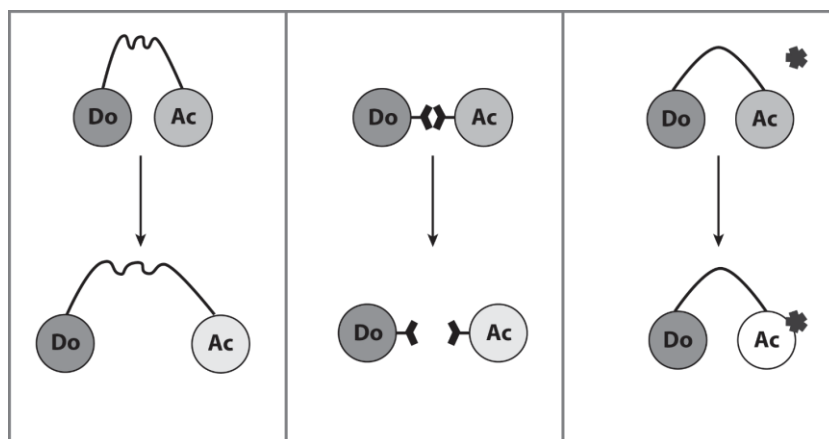


**Figure 2.7.:** Illustration of the most common methods of generating hetero-FRET based sensor response including; conformational change between Do and Ac which leads to changes in FRET efficiency, strategies such as splitting the linker between Do and Ac, and modulation of emission or excitation of the Do or the Ac *via* binding of the analyte.

An already popular method of utilizing the conformational change between the FRET pair is the molecular beacon technique<sup>79</sup>. A single-stranded DNA is folded into a hairpin (FRET-ON). Upon binding of the target, the distance between the Do and Ac is elongated, turning the FRET signal OFF. Such hairpin loops can be designed to conduct thermal analysis in which the loop opens according to the temperature<sup>82</sup>. As well, the strategy of using competitive substitution is widely used in DNA assays including techniques to follow DNA amplifications in PCR such as TaqMan probes, and Scorpion primers<sup>83</sup>.

By splitting the linker between the Do and Ac, FRET efficiencies can also be modulated. Detection of phosphodiesterase I activity can be observed by the enzymatic splitting<sup>80</sup> of the phosphodiester link between Do and Ac, turning the FRET signal OFF. Cysteine (Cys) concentrations can be tracked using a thiol induced cleavage of thioester linker between Do and Ac, which also leads to the FRET signal being turned OFF<sup>84</sup>.

Another method of using hetero-FRET for ratiometric sensing is based on emission or excitation modulation of one of the fluorophores. This technique has an advantage that the analyte unresponsive dye can be used as an internal reference. Using a pH sensitive acceptor and a pH-insensitive Do, a ratiometric pH sensor could be developed<sup>81</sup>. Other examples include a Cys sensor where the Cys cleaves off protective groups from the acceptor (analyte sensitive acceptor and analyte unresponsive donor)<sup>85</sup>, and a Hg<sup>2+</sup> sensor using spectral shifts of a fluorophore that is linked to the ion ligand<sup>86</sup>.

## 2.3. Microbead-based assays

In 2001 when the majority of the human genome was published by the Human Genome Project, the then director of the National Human Genome Research Institute Francis Collins said it was “the end of the beginning”. He explained that with the immense data sets of DNA sequences being available, the goal of better diagnosis, treatment and prevention of diseases could be finally pursued<sup>87</sup>. Since then, many techniques were developed that allow to obtain maximum information from minimum sample volume including planar-arrays and microbead-based assays. Microbead-based assays, compared to conventional planar arrays, have a high degree of multiplexing, high throughput applicability, smaller sample consumption, and reduced analysis time<sup>88</sup>.

### 2.3.1. Microbeads

Microbeads are spherical objects with a diameter of 0.5 to 500  $\mu\text{m}$  that are synthesized from various different materials such as polystyrene (PS)<sup>89</sup>, polymethylmethacrylat (PMMA)<sup>90</sup>, and silica<sup>91</sup>. The surface of a microbead can be coated with many different functional groups such as carboxyl groups, amines, thiols, and alkynes for further probe conjugation. The importance of the bead surface chemistry (functional group type, density, charge) is worth noting as it hugely influences the assay performance<sup>90</sup>.

Using such microbeads as the solid phase in assays has many advantages compared to planar arrays. The high surface area of the microbeads provides larger analytical surfaces, allowing for fast binding kinetics between the DNA probe on the surface and the target DNA. The binding kinetics become faster with smaller size of the bead, reaching similar reaction rates as in solution. Also, fabrication scale of planar arrays has a relatively lower upper limit compared to that of microbeads that can be fabricated at the same time<sup>92</sup>. An illustration comparing planar array to microbead based target detection is shown in Figure 2.8.

### 2.3. Microbead-based assays

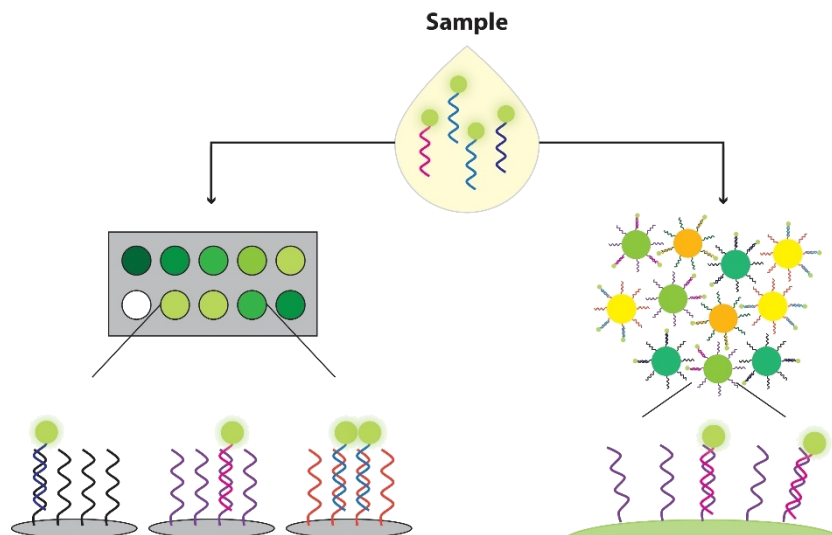


**Figure 2.8.:** Illustration of the difference between planar microarray and microbead-based assay. For a planar array, each spot is deposited with one target capture strand. Its location represents the identifying code in multiplexed analysis. Multiplexing in a microbead-based assay can be achieved by encoding the microbeads.

To perform multiplexed assays, each microbead must be encoded to identify each probe. Many different strategies exist to encode microbeads including optical encoding with fluorescence<sup>93,94</sup> or Raman signals<sup>95</sup>, chemical encoding with nucleic acid codes<sup>96</sup>, graphical encoding with barcodes<sup>97</sup>, and physical encoding using their physical characteristics such as size<sup>24</sup>. The most commonly used strategy is to use polymer microbeads doped with fluorescent dyes with different emission wavelength that can be excited with a single excitation wavelength<sup>98</sup> and using the ratio of the two dyes as the code.

#### 2.3.2. Detection schemes

Microbead detection schemes can be largely divided into three formats: suspensions using a flow cytometer, suspensions using microfluidic devices, and imaging based systems (Figure 2.9)<sup>88</sup>. A flow cytometer is a widely used instrument in biology to detect cells and particles that are fluorescently labeled<sup>92</sup>. The luminescent microbead is decoded and the fluorescent reporter bound to their surface is detected as the particle passes through the sensing point. A typical flow cytometer consists of three functional units: a light source and sensing system, a hydraulic system that focuses the particle to the center of the sensing system, and a data collection system<sup>99</sup> (Figure 2.9 (A)). The most well-known example of suspension arrays is probably the Luminex system<sup>93</sup> with numerous publications demonstrating the suitability of the technique for multiplex analysis. More than 500 targets

## 2. Theoretical background

can be analyzed with this system. The main disadvantage of using this technique, however, is that they are bulky and expensive leading to the shift of interest to microfluidic based devices. Microfluidics is essentially flow cytometry in a microscopic scale, which allows the process or manipulation of small volume ( $10^{-9}$  ~  $10^{-18}$  L) of fluids using micrometer sized channels (Figure 2.9 (B)). This technique allows for smaller use of samples, higher resolution, better sensitivity, lower cost, better temperature control, as well as shorter analysis times <sup>100</sup>. The third method of microbead detection is based on fluorescence microscopy imaging techniques <sup>101-103</sup> (Figure 2.9 (C)). These techniques are based on automatic capture and analysis of two-dimensional fluorescence images. One of the techniques named VideoScan decodes randomly dispersed microbeads in microwell plates, identifying the microbead by the specific dye ratio and size and grouping them in one microbead population. This population is then assigned to one specific analyte, allowing for real-time decoding of the microbeads within a mixture of multiple microbead populations <sup>24</sup>. This technique has been successfully applied for detecting nucleic acids <sup>24</sup>, epitope mapping <sup>104</sup>, and serotyping of *E. coli*. <sup>105</sup>, and quantification of carboxyl groups on the surface of a microbead <sup>90</sup>.

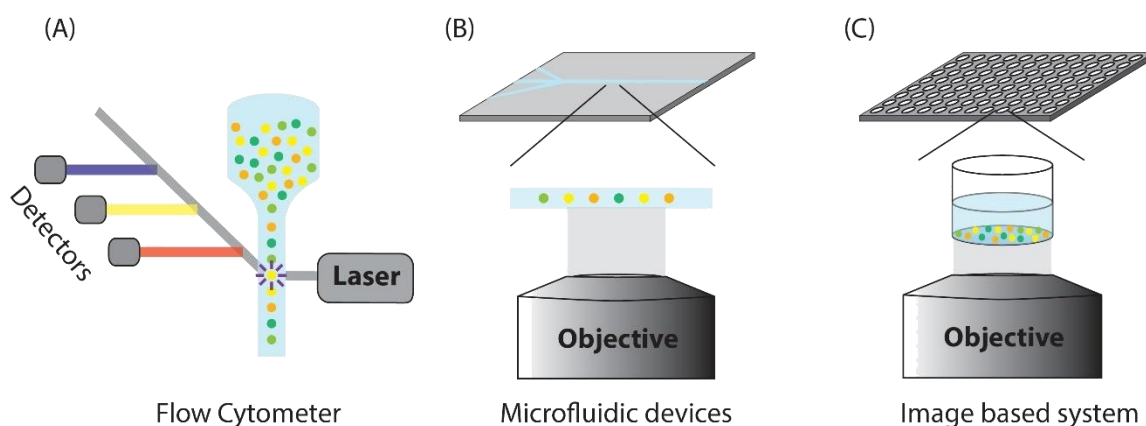


**Figure 2.9.:** Different detection schemes of encoded microbeads. (A) Flow cytometers. The fluorescence of microbeads in suspension are read as they flow past the sensing point. (B) Microfluidic devices. The reduction of sample volume allows not only for miniaturization of the instrument but also for advantages over detection using flow cytometry such as higher resolution and better sensitivity. (C) Image based system. This technique allows for identification of randomly dispersed microbeads at the bottom of a microwell plate using automatic capture and analysis of two-dimensional fluorescence images.

## 2.4. Plasmonics

Plasmonics is a field of nanophotonics where the interaction between light and conduction electrons at metallic interfaces or metal structures in the nanoscale is explored. Although this phenomenon has been documented as early as 1900s<sup>106</sup>, the fascination continued and inspired many scientists to discover various applications of this field.

### 2.4.1. Optical properties of metals

The optical properties of bulk metal can be characterized by their dielectric function  $\epsilon(\omega)$  where  $\omega$  is the frequency of the light. The dielectric function is related to the refractive index  $n(\omega)$  as  $n(\omega) = \sqrt{\epsilon(\omega)}$ . Since  $\omega = 2\pi c/\lambda$ , where  $c$  is the speed of light and  $\lambda$  the wavelength, the dielectric function can be considered either as a function of  $\omega$  ( $\epsilon(\omega)$ ) or  $\lambda$  ( $\epsilon(\lambda)$ ) and is used throughout the following sections accordingly. The dielectric function is given as a complex number since most materials are not transparent, with silver (Ag) and gold (Au) attracting particular interest due to their distinct optical properties<sup>107</sup>. The characteristics of bulk Ag and Au can be shown as in Figure 2.10 with the real part of the dielectric function  $Re(\epsilon(\lambda))$  having negative values and the imaginary part  $Im(\epsilon(\lambda))$  having positive values in the visible range<sup>108</sup>. The  $Im(\epsilon(\lambda))$  is related to the absorption of the material, with Au showing a more complicated behavior due to additional contributions from interband electronic transitions around 400 nm<sup>109</sup>.

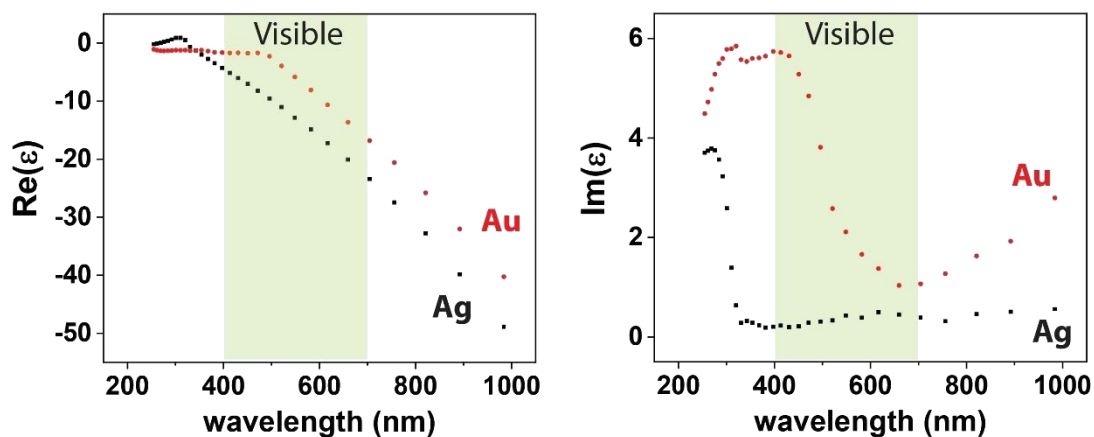


**Figure 2.10.:** Real and imaginary parts of the dielectric function for bulk Ag and Au, as described by Johnson and Chritsy<sup>1</sup>. The real parts are negative over a larger range and the imaginary parts are positive over a small range.



## 2.4. Plasmonics

It is this particular aspect of the two metals, the  $Re(\epsilon(\lambda))$  with large negative values and  $Im(\epsilon(\lambda))$  with very small positive values that results in many optical effects such as surface plasmon resonance (SPR) <sup>25</sup>. SPR is the coherent oscillations of the surface conduction electrons that are excited by electromagnetic radiation <sup>25</sup>. These plasmons can either propagate along the metal-dielectric interface on the order of tens to hundreds of microns which is called surface plasmon polariton (or propagating plasmon). For light interacting with particles much smaller than the incident wavelength, the plasmons oscillate locally around the nanoparticle at a frequency which is known as localized surface plasmon resonance (LSPR).

### 2.4.2. LSPR of nanoparticles

As mentioned above, for light that interacts with finite structures the plasmons oscillate in a non-propagating manner due to the spatial confinement, as illustrated in Figure 2.11 for spherical gold nanoparticles (AuNPs).

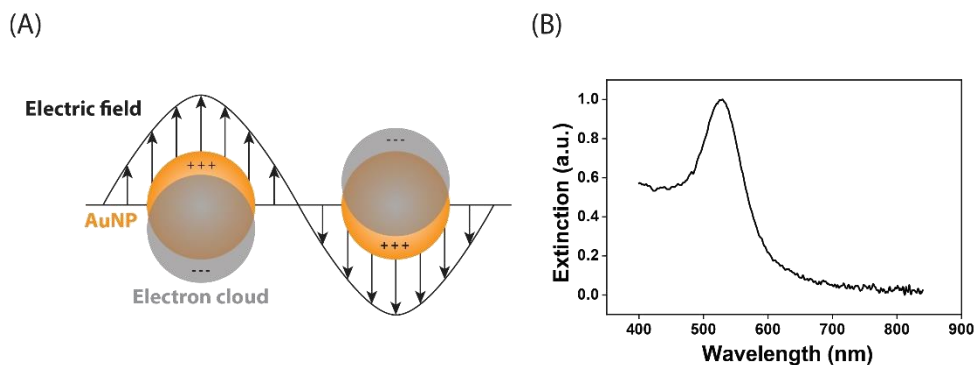


**Figure 2.11.:** Schematic illustration of localized surface plasmon for AuNP. (B) Typical LSPR absorption band of a gold nanoparticle with one extinction maximum.

To calculate the electromagnetic field around the spherical metallic nanostructures, an electrostatic approximation scheme is widely used <sup>25</sup>. This approximation works well when the nanoparticles are significantly smaller than the incident wavelength, where the electric field of the light will be approximately constant over the volume of the interacting particles <sup>109</sup>. For larger particles, fully solving Maxwell's equation (Mie theory <sup>106</sup>) is required as the approximation does not work very well <sup>107</sup>. For smaller particles, which are of primary interest within the scope of this thesis, the collective response of the electrons of the metal nanoparticles to the electric field of the light can be described by the dipolar polarizability  $p$  and is given as <sup>25</sup>,

## 2. Theoretical background

$$p = 4\pi a^3 \left( \frac{\varepsilon(\lambda) - \varepsilon_M}{\varepsilon(\lambda) + \kappa \varepsilon_M} \right), \quad (2.10)$$

where  $a$  is the radius of the particle,  $\varepsilon_M$  the medium of the dielectric constant, and  $\kappa$  the shape factor. The value of  $\kappa$  changes according to the geometry of the particles and for spheres  $\kappa = 2$ . Other geometries are explained further in the latter part of this section. It is worth taking further note of the denominator of equation 2.10 here. Since  $\varepsilon(\lambda)$  is a complex number, it is not possible to satisfy  $\varepsilon(\lambda) = -2\varepsilon_M$ . But an interesting phenomenon arises if conditions are met so that  $Re(\varepsilon(\lambda)) = -2\varepsilon_M$ . At the wavelength where this criterion is met, the magnitude of  $p$  is limited by how small  $Im(\varepsilon(\lambda))$  is, and this results in a resonance called the dipolar LSPR of the sphere. It is important to note that this resonance is induced solely by geometrical aspects. The extinction spectrum of the metal sphere is also dependent on the dielectric function of the metal and shows resonance at  $Re(\varepsilon(\lambda)) = -\kappa\varepsilon_M$  as shown in Figure 2.11 (B) <sup>25</sup>.

Compared to spherical particles, the polarizability of nanorods is more complicated to calculate due to their anisotropic shape. A schematic illustration of light interacting with gold nanorods (AuNRs) is shown in Figure 2.12 (A) along with typical LSPR bands shown in Fig.2.12 (B).

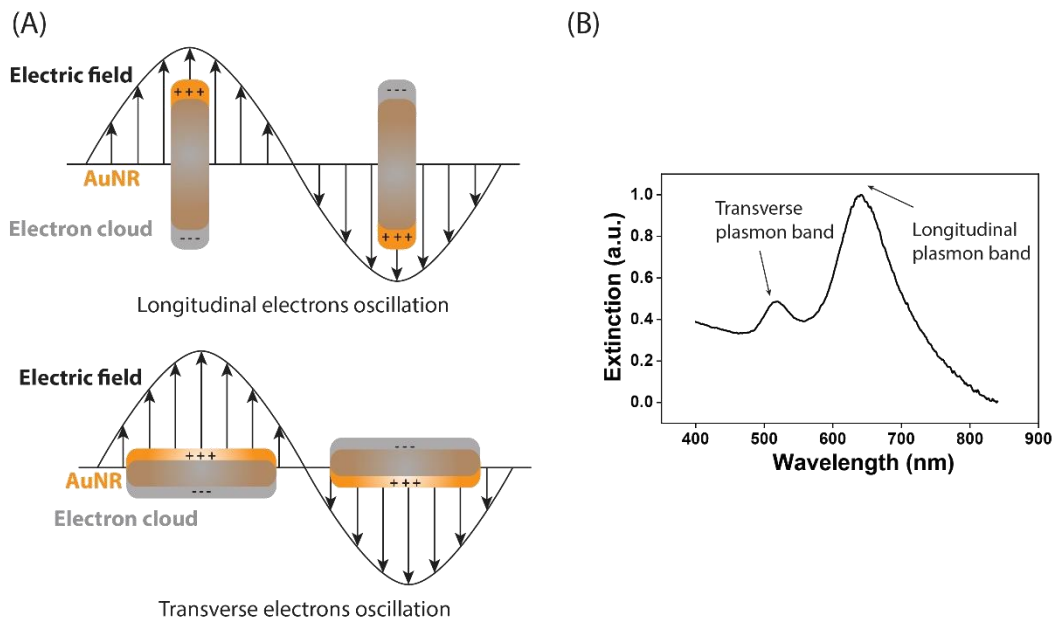


**Figure 2.12.:** (A) Schematic illustration of localized surface plasmon resonances for AuNRs with longitudinal and transverse oscillation according to the polarization of the incident light. (B) Typical LSPR absorption bands of AuNRs with two extinction maxima.

## 2.4. Plasmonics

The solution to solving this complex shape was to treat rods as small spheroids, which was developed by Gans in 1912<sup>25</sup>. For simplicity, only rods that are much smaller than the wavelength of incident light is considered (within the electrostatic approximation). If the prolate spheroid has two different axes lengths ( $a > b$ ), the  $p_i$  in the field parallel to one of its axes is given as<sup>25</sup>,

$$p_i = 4\pi ab^2 \left( \frac{\varepsilon(\lambda) - \varepsilon_M}{3\varepsilon_M + 3P_i(\varepsilon(\lambda) - \varepsilon_M)} \right), \quad (2.11)$$

where  $i$  indicates the different polarizations of light with respect to the axis, and  $P_i$  is the geometrical depolarization factor<sup>25</sup>. The depolarization factor for the spheroids can be described as,

$$P_a = \frac{1 - e^2}{e^2} \left[ \frac{1}{2e} \ln \left( \frac{1 + e}{1 - e} \right) - 1 \right], \quad (2.12)$$

$$P_b = \frac{1 - P_a}{2}, \quad (2.13)$$

where  $e$  is given by,

$$e^2 = 1 - \left( \frac{b}{a} \right)^2 = 1 - \left( \frac{1}{AR} \right)^2, \quad (2.14)$$

where  $AR$  is the aspect ratio of the rod. The LSPR for nanorods appears if  $Re(\varepsilon) = -\left(\frac{1-P_i}{P_i}\right)\varepsilon_M$ , where  $P_i=P_a$  for the longitudinal plasmon resonance and  $P_i=P_b$  for the transverse plasmon resonance. It is worth noting here that the aspect ratio of the nanorods have significant impact on the polarizability as shown in equations 2.11 and 2.14. The extinction spectrum naturally depends on the polarizability, resulting in two extinction maxima; around 500 nm for the transverse and at a longer wavelength for the longitudinal plasmon resonance (Figure 2.12 (B)). Interestingly for these nanorods, the longitudinal absorption maxima can be calculated according to the aspect ratio and dielectric constant instead of calculating the whole absorption spectrum<sup>110</sup>.

### 2.4.3. Local Field Intensity Enhancement Factor (LFIEF)

Another interesting aspect of light interacting with metal is the local field intensity enhancement factor (LFIEF) at the surface. This is given at a specific point  $z$  (with local field depending on  $\omega$ ) as,

## 2. Theoretical background

$$\text{LFIEF}(z, \omega) = \frac{|E(z, \omega)|^2}{|E_0(z, \omega)|^2}, \quad (2.15)$$

where  $E(z, \omega)$  is the electric field amplitude at the surface of the metal particle (or near-field), and  $E_0(z, \omega)$  the intensity of the incoming field <sup>109</sup>. The magnitude of LFIEF indicates if the local electric field will be enhanced (LFIEF >1) or quenched (LFIEF <1) and will directly indicate the specific optical processes that occur at that specific point. The near-field ( $E(z, \omega)$ ) of a nanoparticle in the dipolar limit is given as <sup>111</sup>,

$$E(z, \omega) = \frac{(1 + \kappa)\epsilon_M}{\epsilon(\omega) + \kappa\epsilon_M} E_0(z, \omega), \quad (2.16)$$

with  $E_0$  being the incident field. At resonant conditions for spherical particles ( $\text{Re}(\epsilon(\omega)) = -2\epsilon_M$ ), LFIEF will reach its maximum (equation 2.10). For nanorods, the shape factor can be given as  $\kappa = \left(\frac{1-P_i}{P_i}\right)$  with resonant conditions met at  $\text{Re}(\epsilon(\omega)) = -\kappa\epsilon_M$ . This near-field influences optical processes that occur close to the nanoparticle resulting in effects such as surface enhanced Raman scattering (SERS) <sup>25</sup> and surface enhanced fluorescence (SEF) <sup>112</sup>. These are further explained in latter sections (section 2.4.5 and section 2.4.6)

### 2.4.4. Coupled LSPR

If two nanoparticles are in close proximity to each other, the near-field of the two particles can interact with each other resulting in coupling of the plasmon oscillations of the particles. The plasmon coupling interaction of two nanoparticles can be described as hybridization of plasmon modes, analogous to the coupling of molecular orbitals <sup>29</sup>. The plasmon modes supported by the two nanoparticles hybridize, resulting in a lower energy bonding plasmon mode and a higher energy anti-bonding plasmon mode. These modes are determined by the orientation of the particles in relation to the incident light polarization. For plasmon coupling of two spherical particles, a lower energy bonding plasmon mode (polarization along dimer axis, longitudinal) and a higher energy anti-bonding mode (polarization perpendicular to the dimer axis, transverse) is excited. For plasmon coupling of two nanorods, the longitudinal plasmon mode is excited for an end-to-end dimer whereas the anti-bonding mode is excited for a side-to-side dimer (Figure 2.13) <sup>111</sup>. As is for the case in the molecular analog of the

## 2.4. Plasmonics

bonding modes, the resulting electric field intensity peaks in the so called ‘hot-spots’ between the dimers.

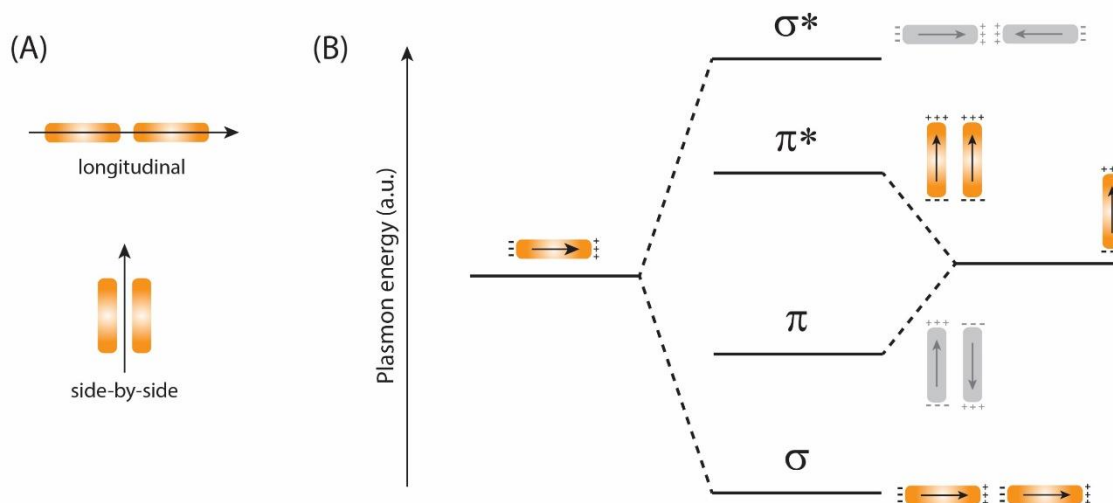


**Figure 2.13.:** Plasmon hybridization model for AuNRs. (A) Different assembly of AuNRs (longitudinal and side-by-side) with light polarization shown in black arrow. (B) Bonding and anti-bonding mode according to plasmon hybridization model. Bright modes (nonzero dipole moment) are shown in color and dark modes (zero dipole moment) are shown in grey.

## 2.4.5. Surface enhanced Raman scattering (SERS)

Raman scattering is the simultaneous absorption of an incident photon and emission of another photon with a different energy than that of the incident photon <sup>113</sup>. This is different to fluorescence (section 2.2), where the absorption of an incident photon and emission of a photon happen in two separate steps. Upon interaction with light, the molecule occupies a ‘virtual state’, from which it relaxes down to the ground state either with the same energy (elastic Rayleigh scattering) or different energy (inelastic Raman scattering) as the incident photon (Figure 2.14) <sup>114</sup>.

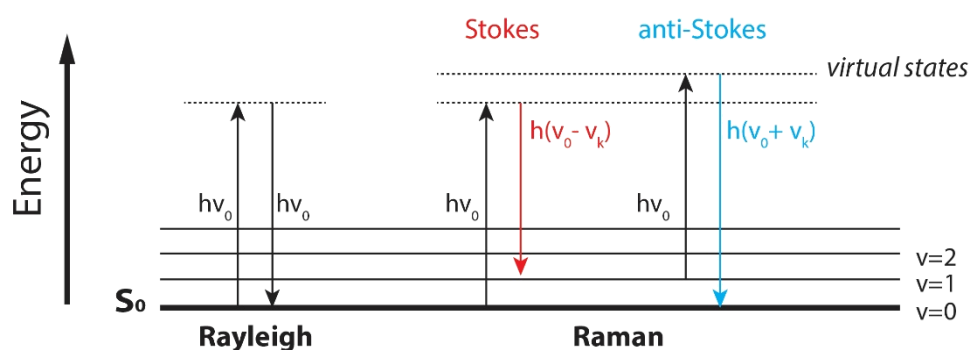


**Figure 2.14.:** Jablonski diagram of the scattering processes Rayleigh and Raman. Molecules are excited via incident photon to a virtual state, and is simultaneously relaxed to the ground state either with the same energy ( $h\nu_0$ ), less energy ( $h(\nu_0 - \nu_k)$ ), or more energy ( $h(\nu_0 + \nu_k)$ ).

## 2. Theoretical background

Scattering can also be classically described as the radiation emitted by an oscillating electric dipole. Within a phenomenological approach, the induced dipole moment  $P$  is proportional to the incident electromagnetic field  $E$  with an angular frequency  $\omega_0$  (or frequency  $\nu_0$ ) and an amplitude  $E_0$ :

$$P = \alpha E = \alpha E_0 \cos(\omega_0 t) = \alpha E_0 \cos(2\pi\nu_0 t), \quad (2.17)$$

where  $\alpha$  is the polarizability tensor, and  $t$  is time. The  $\alpha$  is affected by molecular vibrations and its dependence on the normal coordinate  $Q$  of a vibration. This can be approximated by the first two terms of the Taylor expansion as,

$$\alpha = \alpha_0 + \left( \frac{\partial \alpha}{\partial Q} \right)_{Q=0} Q, \quad (2.18)$$

where the subscript  $Q = 0$  refers to the equilibrium position of the vibration. A vibrating molecule experiences changes in the normal coordinate (with amplitude  $Q_0$ ) which is described as,

$$Q = Q_0 \cos(2\pi\nu_0 t). \quad (2.19)$$

Using equations 2.17, 2.18, and 2.19  $P$  can now be described as,

$$\begin{aligned} P &= \alpha_0 E_0 \cos(2\pi\nu_0 t) && \} \text{Rayleigh} && (2.20) \\ &+ \frac{1}{2} \left( \frac{\partial \alpha}{\partial Q} \right)_{Q=0} Q_0 E_0 \cos(2\pi(\nu_0 + \nu_k)t) && \} \text{anti - Stokes} \\ &+ \frac{1}{2} \left( \frac{\partial \alpha}{\partial Q} \right)_{Q=0} Q_0 E_0 \cos(2\pi(\nu_0 - \nu_k)t) && \} \text{Stokes.} \end{aligned}$$

The three distinct frequencies of  $P$  describes the oscillation frequencies of the scattered light, of which the first term describes Rayleigh scattering with the same frequency as the incident light ( $\nu_0$ ). The two following terms describe Raman scattering with either increased frequency (anti-Stokes) or decreased frequency (Stokes). Equation 2.20 also tells us the selection rule for Raman scattering, that is, that the molecule is only Raman-active if  $\left( \frac{\partial \alpha}{\partial Q} \right)_{Q=0} \neq 0$ .

Cross sections  $\sigma$  of Raman scattering represent the efficiency of the scattering process<sup>25</sup>. Typically, Raman cross sections are on the order of  $10^{-30} \text{ cm}^2 - 10^{-25} \text{ cm}^2$  per molecule whereas the fluorescence cross sections are on the order of  $10^{-16} \text{ cm}^2$ <sup>115</sup>. Resonance Raman scattering is observed if the virtual state overlaps with an electronic state of the molecule, increasing the

## 2.4. Plasmonics

Raman cross section. However, this process also results in fluorescence which will overshadow the Raman scattered light.

As mentioned, the cross sections of Raman scattering are extremely low. A method to overcome this problem is by using SERS<sup>116</sup>, where the Raman signal of the molecule is enhanced in the vicinity of a metal surface. As Raman scattering is an instantaneous process, both the absorbed ( $\omega_L$ ) and scattered ( $\omega_S$ ) light are subject to local field enhancement. In many cases, the difference between the two LFIEF are ignored ( $\omega_L \approx \omega_S$ ). The enhancement factor EF at a given point therefore can be written as<sup>109</sup>,

$$EF = \text{LFIEF}(\omega_L) \times \text{LFIEF}(\omega_S) \sim \text{LFIEF}^2(\omega_L) = \frac{|E(z, \omega)|^4}{|E_0(z, \omega)|^4}, \quad (2.21)$$

and is often referred to as the E<sup>4</sup>-approximation (electromagnetic enhancement). In addition to these electromagnetic enhancements, chemical enhancement can have an effect if the molecule is adsorbed directly on the metal surface. The resulting overall SERS intensity  $P_{\text{SERS}}$  can be written as<sup>115</sup>,

$$P_{\text{SERS}} \sim N \cdot I_L \cdot EF \cdot \sigma_{\text{ads}}^R, \quad (2.22)$$

where N is the number of molecules involved in SERS,  $I_L$  the laser intensity, and  $\sigma_{\text{ads}}^R$  the Raman cross section of molecules adsorbed on the metal surface. As mentioned, resonance Raman scattering increases the cross section and fortunately for molecules very close to the metal surface their fluorescence is quenched. Such process is termed surface enhanced resonance Raman scattering (SERRS).

### 2.4.6. Surface enhanced fluorescence (SEF)

Like SERS, fluorescence of a molecule is influenced by the metal surface. The LFIEF leads to an enhancement in absorption just as was the case for SERS. However, since the absorption and emission are two separate steps in fluorescence, the relaxation process only experiences modification in the decay rates (section 2.2). Therefore, the modification of fluorescence near a metal surface is also termed radiative decay engineering<sup>117</sup>. A modified quantum yield termed radiative efficiency ( $\eta$ ) is introduced to describe the relative contribution of radiative to non-radiative decays. The EF for fluorescence can be thus described as,

$$EF_F = \text{LFIEF}(\omega_L) \times \eta. \quad (2.23)$$

## 2. Theoretical background

The contributions of LFIEF( $\omega_L$ ) and  $\eta$  compete with each other and depend on the distance between the fluorophore and the metal surface. In contrast to FRET where quenching of the donor by energy transfer to the acceptor has a  $r^{-6}$  (equation 2.3) dependency, energy transfer from a dipole to a surface is written as <sup>118</sup>,

$$E_{NSET} = \frac{R_0^4}{R_0^4 + r^4}, \quad (2.24)$$

where *NSET* stands for nanometal surface energy transfer. Quenching of the fluorophore therefore occurs with a  $r^{-4}$  dependency near a metal nanoparticle <sup>119</sup>. This competition of SEF and quenching of the fluorescence near metal surfaces results in the variety of effects that is observed for a fluorophore near a metal surface including SEF <sup>58,120–124</sup>, and fluorescence quenching <sup>119,125–127</sup>. In addition, as the decay rates are modified, FRET efficiencies (explained in section 2.2.2) can also be enhanced near metallic nanoparticles <sup>128,129</sup>.

### 2.4.7. DNA assisted plasmonics

It is clear from previous sections that the location of the analyte of interest with respect to the particle, as well as the assembly of the particles is of great significance when it comes to plasmonics. DNA is a great way of controlling these parameters, thus many studies have been dedicated to coating and assembling nanoparticles with DNA.

Strategies to rationally assemble AuNPs were developed by Mirkin <sup>130</sup> and Alivisatos <sup>131</sup> by functionalizing the particles with thiolated ssDNA. Since then, work has been extended to coating silver nanoparticles (AgNPs) <sup>132–134</sup> and AuNRs <sup>135–138</sup>. Once the nanoparticles are coated with DNA, they can be further assembled on DNA origami platforms by using complementary capture strands.

In general, the DNA coating of particles relies on the relatively strong metal-thiol bond. However, for citrate stabilized particles the attachment is not straightforward as both the surface of the particle and the DNA are negatively charged and thus repelling each other. This problem can be addressed by using salt-aging methods, where NaCl is gradually added over a long period of time (1-2 days) <sup>139</sup>. By increasing the salt concentration, the repulsion between the negatively charged DNA strands is also reduced. This process, however, does not work well for AuNPs that are over 50 nm in size <sup>140</sup>, or for AgNPs with a weaker Ag-thiol bond <sup>141</sup>. Many alternative methods were developed to facilitate functionalization of such particles



## 2.4. Plasmonics

including the use of DNA containing multiple thiol groups<sup>132</sup>, growing a monolayer of gold after the synthesis of AgNP<sup>138,142</sup>, using longer thiolated ssDNA strands<sup>134</sup>, or by using a low pH buffer during coating steps<sup>133,140</sup>. Also, using a longer thiol-DNA for coating (more than 20 nb) reduces the tendency for aggregation by setting a minimum distance between the particles<sup>143</sup>. For strategies using low pH, coating is assisted as A and C bases are protonated, phosphate groups in the DNA backbone are partially protonated, and some of the citrate groups on the particles are protonated thereby reducing the repulsion between the particles and the DNA strands as well as among the DNA strands themselves<sup>140</sup>.

DNA functionalization becomes more tricky for AuNRs since they require a shape-directing surfactant, cetyltrimethylammonium bromide (CTAB), for synthesis<sup>144,145</sup>. Two problems arise from this surfactant, the first being that the CTAB forms a very tight bilayer on the surface of the AuNR, therefore hindering the accessibility of the thiol groups to reach the metal surface. The second problem is that the positively charged CTAB electrostatically attracts the negatively charged ssDNA nonspecifically, which leads to irreversible aggregation of AuNRs. Again, several approaches have been developed to coat the nanorods, such as using low pH buffers<sup>136</sup>, growing a thin layer of Au on the AuNR surface<sup>146</sup>, but also different approaches such as ligand exchange *via* round-trip phase transfer<sup>147</sup>, and carboxylic acid-containing polymer coating using a layer-by-layer approach<sup>148</sup>. The basic problem however still prevails. Using low pH buffers does not sufficiently replace the adsorbed CTAB thus making the density of the thiol-ssDNA on the surface not high enough<sup>149</sup>. The latter approaches are unfortunately complex and very time consuming.

It is also worth noting that the seed-mediated synthesized nanorods with short aspect ratios of 3-7 have mainly {111} and {100} faces of Au at the ends, and {110} faces along the length of the AuNRs. This therefore leads to preferentially binding of CTAB along the length of the rods since the {110} facet has a higher surface energy and greater tendency to bind to surfactant<sup>150,151</sup> (Figure 2.15 (A)). This subsequently leads to the thiol group preferentially binding to the ends of the nanorods and less along the sides of the rods<sup>150,152,153</sup> (Figure 2.15 (B)).

It is also worth mentioning that the surface coverage of the particle must be high in order to prevent particles from aggregating in the magnesium buffer that is required for DNA origami nanostructures. For maximizing the surface coverage the salt concentration must be high, a spacer region for the coating sequence must exist, and the sequence of this coating DNA

## 2. Theoretical background

should contain bases that have low affinity to the metal surface for reducing nonspecific adsorption<sup>154</sup>. For Au the affinity is highest for A and lowest for T<sup>155</sup>, whereas for Ag the affinity is highest for T and lowest for A<sup>156</sup>.

Finally, assembling nanoparticles can be achieved by having several capture strands on the DNA origami that are complementary to the coating strands of the nanoparticles (Figure 2.15 (C)). Precise assembly of nanoparticles and analyte molecules of interest can be achieved on DNA origami platforms, and vast number of studies such as SERS of single molecules<sup>27,28</sup>, SEF of single molecules<sup>59,157</sup>, circular dichroism studies of chiral plasmonic structures<sup>158</sup>, and plasmonic waveguides<sup>159,160</sup> amongst many others can be conducted<sup>161</sup>.

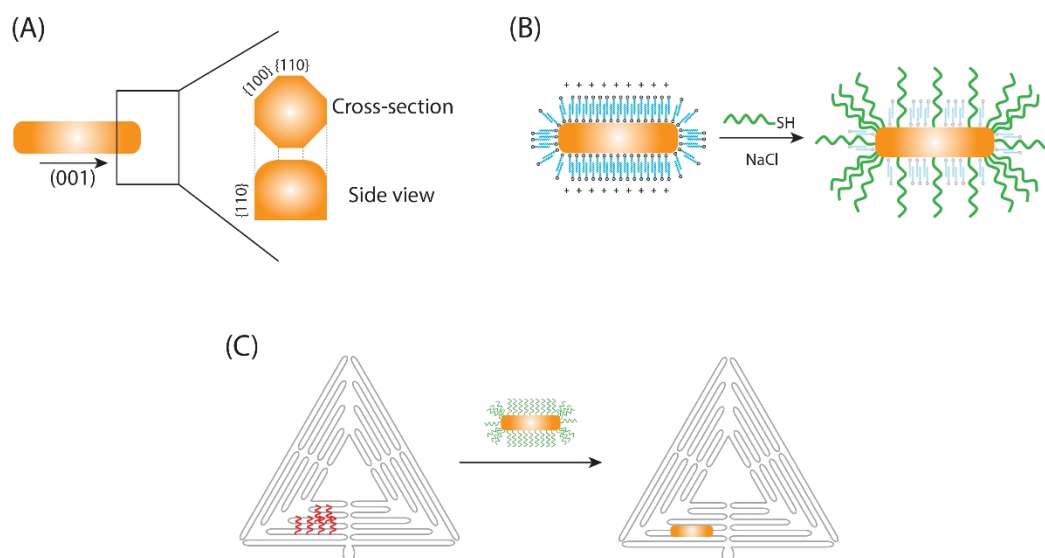


**Figure 2.15.:** DNA coating of AuNRs. (A) Crystalline structure of short AuNRs with growing direction (001), and different facets along the edge and the end. (B) Coating of CTAB bilayer covered positively charged AuNRs with thiol-DNA, with preferential binding of DNA to the ends. (C) Illustration of AuNR immobilization on DNA origami using capture strands and DNA coated AuNRs.

## 3. Materials and methods

### 3.1. Materials and chemicals

All DNA strands used here were purchased from IDT technologies for un-modified staple strands, from Metabion for modified staple (fluorophore-, thiol-, or extended) strands, and from tilibit nanosystems for the M13mp18 scaffold strand. Fluorophores used here are coumarin 343 (C343), fluorescein (FAM), cyanine3 (Cy3), ATTO 647N, carboxytetramethylrhodamine (TAMRA), and phenylethynylpyrene (PEPY). All DNA sequences are written from 5'- to 3'-. DNA sequences are listed in Table 3 (more information is given in Appendix).

**Table 3.1.:** List of DNA sequences used (Metabion). Further details including target sequences for microbead-based assay studies are given in the Appendix (dT(x): T that is modified with x).

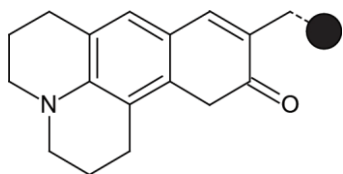
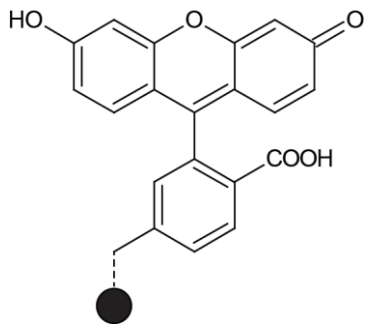
<b>FRET nanoarrays</b>	<b>function</b>	<b>Complementary strands</b>
(C343)-(TTG) <sub>7</sub>	pH sensor, donor	(CAA) <sub>7</sub> -(staple)
(FAM)-(ATT) <sub>7</sub>	pH sensor, acceptor nanoarray, donor	(AAT) <sub>7</sub> -(staple)
(Cy3)-(TTG) <sub>7</sub>	nanoarray, acceptor	(CAA) <sub>7</sub> -(staple)
<b>Microbead-based assay</b>	<b>function</b>	
(ATTO 647N)-(ATT) <sub>7</sub>	Dye-label	(AAT) <sub>7</sub> -(staple)
(Staple)-T <sub>40</sub>	Probe strand	(target strand)-A <sub>40</sub>
<b>Coating strands</b>	<b>particles</b>	
SH-A <sub>4</sub> (ATT) <sub>3</sub>	AuNR	(TAMRA)-(AAT) <sub>3</sub> T <sub>3</sub> (AAT) <sub>3</sub> T <sub>3</sub> -(TAMRA)
(ATT) <sub>7</sub> T <sub>7</sub> -SH	AuNR	(TAMRA)-A <sub>7</sub> (AAT) <sub>7</sub>
(TAMRA)-T <sub>4</sub> (GGG ATT) <sub>4</sub> T <sub>4</sub> -SH	AuNR	X

### 3. Materials and Methods

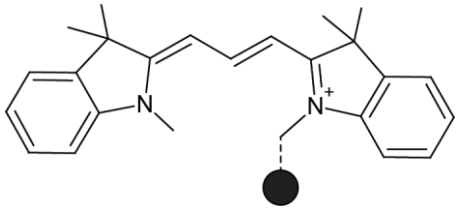
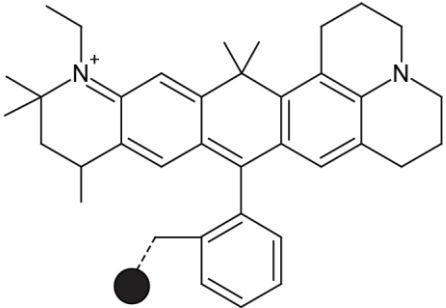
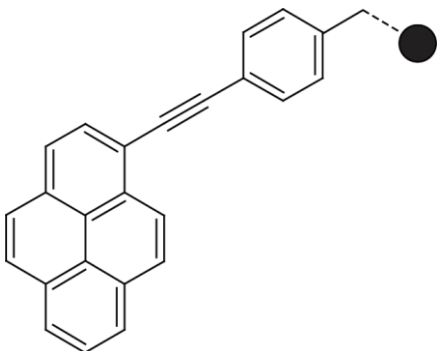
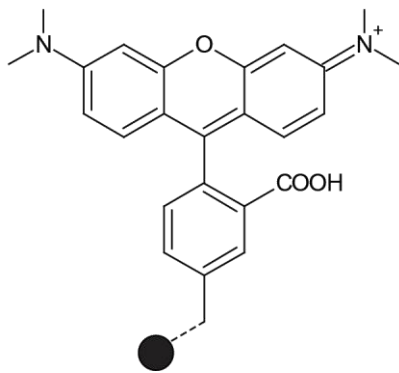
(TTT) <sub>8</sub> T <sub>4</sub> -SH	AuNR	(AAA) <sub>8</sub> T <sub>4</sub> -(staple), (TAMRA)-A <sub>4</sub> (AAA) <sub>7</sub> , (AAA) <sub>7</sub> A <sub>4</sub> -(TAMRA)
SH-dT(TAMRA)T <sub>3</sub> (TTT) <sub>8</sub>	AuNP, AgNP	(AAA) <sub>8</sub> T <sub>4</sub> -(staple)
SH-dT(PEPY) T <sub>3</sub> (TTT) <sub>8</sub>	AuNP, AgNP	
SH-T <sub>4</sub> (TTT) <sub>8</sub>	AuNP, AgNP	

Fluorophores used in this work are listed in Table 3.2 with their chemical structures, maximum absorption wavelengths ( $\lambda_{abs}$ ), and maximum emission wavelengths ( $\lambda'_{emi}$ ) of each fluorophore. Fluorescence decay lifetimes ( $\tau_s$ ) for C343, FAM, and Cy3 are also given in the table.

**Table 3.2.:** List of fluorophores (C343, FAM, Cy3, ATTO 647N, PEPY, TAMRA) with chemical structures and spectral properties ( $\lambda_{abs}$ : maximum absorption wavelength,  $\lambda'_{emi}$ : maximum emission wavelength,  $\tau_s$ : fluorescence decay lifetime). The black circle on the chemical structure is the attachment point for the DNA.

Fluorophore	Chemical structure	$\lambda_{abs}(nm)$	$\lambda'_{emi}(nm)$	$\tau_s(ns)$
<b>C343</b>		451	493	5.0
<b>FAM</b>		480	520	4.5

### 3.1. Materials and Chemicals

<p><b>Cy3</b></p>	 <p>The structure shows two indole rings connected by a trimethine chain. The right-hand nitrogen is positively charged and is linked via a dashed line to a black circle representing a bead.</p>	<p>550</p>	<p>564</p>	<p>2.2</p>
<p><b>ATTO 647N</b></p>	 <p>The structure features a central xanthene core with a trimethylammonium group on the left and a piperidine ring on the right. A phenyl ring is attached to the core, which is further linked via a dashed line to a black circle representing a bead.</p>	<p>650</p>	<p>664</p>	
<p><b>PEPY</b></p>	 <p>The structure consists of a perylene core connected via an ethynyl group to a para-substituted phenyl ring. The phenyl ring is further linked via a dashed line to a black circle representing a bead.</p>	<p>370, 392</p>	<p>399, 421</p>	
<p><b>TAMRA</b></p>	 <p>The structure is a xanthene derivative with a trimethylammonium group on the left and a trimethylammonium group on the right. It has a carboxylic acid group (COOH) and a phenyl ring attached to the core. The phenyl ring is further linked via a dashed line to a black circle representing a bead.</p>	<p>557</p>	<p>580</p>	

Buffers for synthesizing and storing DNA origami nanostructures were diluted to the appropriate concentration from 10x TAE composed of 40 mM tris(hydroxymethyl)aminomethane (Tris), 20 mM acetic acid, 1mM ethylenediaminetetraacetic acid (EDTA) purchased from Sigma-Aldrich. Magnesium chloride

### 3. Materials and Methods

(MgCl<sub>2</sub>), sodium chloride (NaCl), hydrochloric acid (HCl), and sodium hydroxide (NaOH) were also purchased from Sigma-Aldrich. Thioacetamide (TAA) used as one of the analytes for ratiometric sensing was purchased from Fluka. Chemicals required for nanoparticle coating such as sodium dodecyl sulfate (SDS), and bis(p-sulfonatophenyl)phenylphosphine (BSPP) were also purchased from Sigma-Aldrich. For detection of oligonucleotides using microbead-based assays, the dual colored fluorescence stained carboxylated PMMA microbeads were purchased from PolyAn. For AuNR synthesis, chloroauric acid (HAuCl<sub>4</sub>·xH<sub>2</sub>O), sodium borohydride (NaBH<sub>4</sub>), and silver nitrate (AgNO<sub>3</sub>), were purchased from Sigma-Aldrich, hexadecyltrimethylammonium bromide (CTAB) was purchased from SERVA, and ascorbic acid (AA) was purchased from Carl Roth. As for spherical particles used in this work, AuNPs (OD<sub>520nm</sub> = 0.1) were purchased from BBI solutions and AgNPs (0.02 mg/mL) from Sigma-Aldrich. In order to determine the DNA strand density on the particle, dithiothreitol (DTT) was used which was also purchased from Sigma-Aldrich.

## 3.2. Sample preparation

### 3.2.1. DNA origami nanostructure fabrication

DNA origami nanostructure fabrication differed according to the application they were designed for. Generally speaking, two types of methods were utilized where the DNA origami nanostructures were designed for 1) FRET based ratiometric sensing and microbead-based assays, or 2) for nanoparticle assembly. The triangular DNA origami nanostructures were fabricated as described by Rothmund (Figure 2.2) <sup>8</sup>. The structure was self-assembled using the circular scaffold strand (5 nM) and 208 short oligonucleotides (modified and un-modified, 150 nM) in TAE buffer (10 x concentrated) containing 150 mM MgCl<sub>2</sub> and ultrapure water (Merck Millipore). The solution was subsequently annealed by rapidly heating to 80 °C and slowly cooling down to 8 °C over 2 hours using a thermal cycler (PEQLAB/VWR). Once fabricated, the DNA origami nanostructures are further hybridized either with dye-labeled ssDNA strands or with DNA coated nanoparticles complementary to the capture strands (Figure 3.1).

### 3.2. Sample preparation

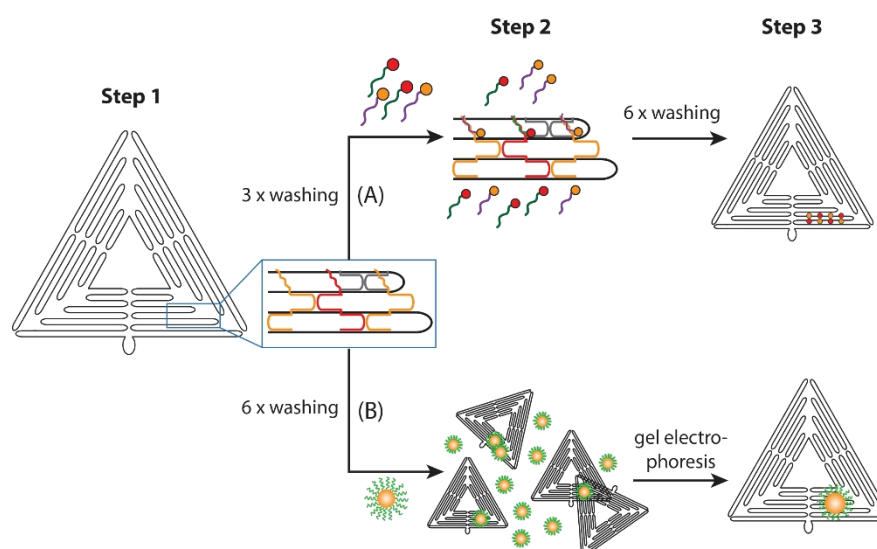


**Figure 3.1.:** DNA origami nanostructure fabrication. After fabricating the triangular DNA origami structure with the modified and un-modified staple strands (step 1) and first purification step using centrifugal filters, they are subsequently hybridized with (A) dye-labeled DNA strands for FRET based ratiometric sensing and microbead-based assay or (B) DNA coated nanoparticle for plasmonic studies (step 2). Final DNA origami nanostructures were obtained (step 3) after final purification step, either another 6 x washing step using centrifugal filters or by gel electrophoresis.

#### FRET nanoarray DNA origami fabrication

The fabricated DNA origami nanostructure solution with modified capture strands, either with  $(AAT)_7$  or  $(CAA)_7$  (from Step 1 in Figure 3.1), was purified three times using centrifugal filters (100 kDa MWCO, Merck Millipore; 6000 rpm, 7 min) with 1 x TAE, 15 mM  $MgCl_2$  solution (Figure 3.1 (A)). For the subsequent hybridization step, dye-labeled complementary ssDNA strands (either with FAM- $(ATT)_7$  or Cy3- $(TTG)_7$  sequence) were mixed (at a minimum excess of 20 folds). This was heated up and kept at 45 °C for 41 min and cooled down to 25 °C over 20 min using again the thermal cycler. The final DNA origami solution was purified again using centrifugal filters 6 times. Final concentration of DNA origami in solution was set to approximately 5 nM for fluorescence measurements, and checked using UV-Vis absorption spectroscopy (NanoDrop 2000, Thermo Scientific). The designs of the FRET nanoarrays are shown in Figure 3.2 with five different nanoarray sizes from **(2x1)** to **(3x4)**.

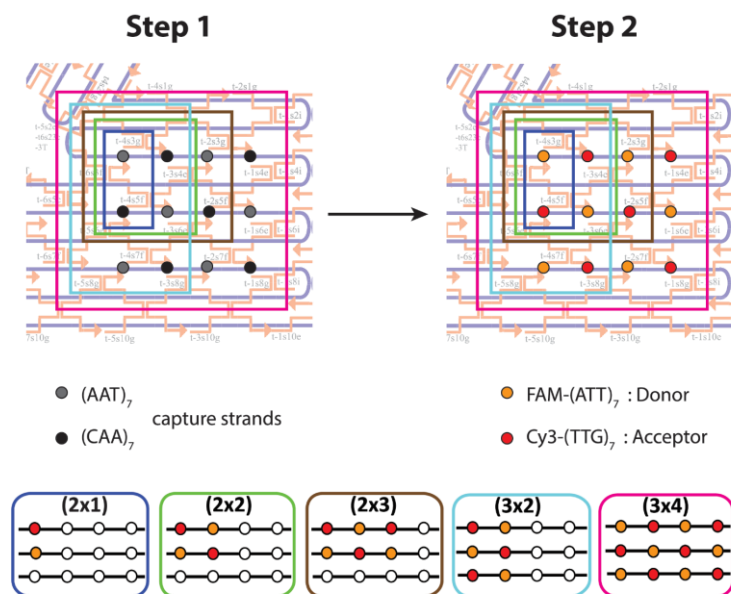


**Figure 3.2.:** DNA origami design for fabrication of FRET nanoarrays. DNA origami nanostructures were synthesized with capture strands either with (AAT)<sub>7</sub> or (CAA)<sub>7</sub> modified staples. Depending on which modified staples mixed within synthesis Step 1 in (A), the resulting fabricated nanoarrays are shown in (B). FAM is used as donor and Cy3 is used as acceptor in these nanoarrays.

For proof-of-concept of pH ratiometric sensing, each pH buffer (1x TAE, 15 mM MgCl<sub>2</sub>) was prepared by adding appropriate amounts of HCl and NaOH, and the pH measured using a pH meter (Orion 3 Star, Thermo Scientific). Buffers for the DNA origami nanostructures were exchanged during the 6 x washing step (Figure 3.1 (A)) of DNA origami nanostructure folding to have the desired pH. Here the pH unresponsive C343 and pH sensitive FAM were used as donor and acceptor ((C343)-(TTG)<sub>7</sub>, and FAM-(ATT)<sub>7</sub>), respectively (Figure 3.3). All pH

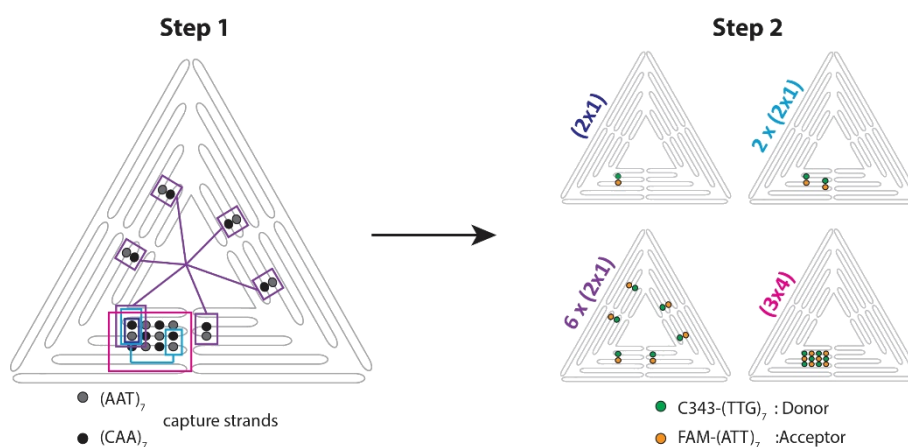


**Figure 3.3.:** DNA origami design for fabrication of FRET nanoarray for pH ratiometric sensing. Depending on the capture strands modified in step 1, the resulting nanoarrays are as shown in step 2. Here, C343 is used as the donor molecule and FAM is used as the acceptor molecule.



### 3.2. Sample preparation

ratiometric sensing related fabrication and measurements were conducted by Lisa Kotthoff within her Masters thesis.

In search of other proof-of-principle ratiometric sensing applications with the DNA origami nanoarrays, TAA was used as an analyte with the same donor and acceptor FRET pair as for pH ratiometric sensing (C343 and FAM, respectively) using the **(3x4)** arrangement as shown in Figure 3.3. An aliquot of concentrated TAA (1 M) was sequentially added to the prepared DNA origami nanostructures for concentration dependent measurements.

#### DNA origami reporter for microbead-based assays

For these reporters, DNA origami nanostructures were synthesized with the probe strands (extended on the 3'- end of the staple strand with T<sub>40</sub>) or dye labeled handles ((AAT)<sub>7</sub>) as the modified staple strands. The fabricated DNA origami nanostructure solution was purified (following the route illustrated in Figure 3.1 (A)) and the dye labeled handles were hybridized with ATTO 647N labeled oligonucleotides (ATTO 647N-(ATT)<sub>7</sub>) using the same method as for the FRET nanoarray assemblies. The dyes are 11-12 nm apart from each other, preventing self-quenching of the dyes <sup>162</sup>.

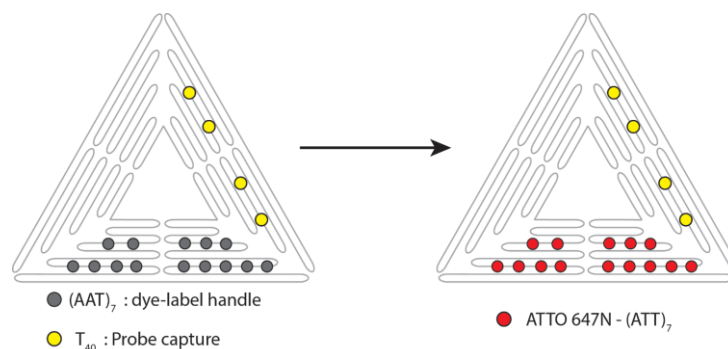


**Figure 3.4.:** DNA origami design for fabrication of a reporter system for microbead-based assays. This process also follows the synthesis route in Figure 3.1 (A), using T<sub>40</sub> extended staples as probe strands to detect oligonucleotides of interest and (AAT)<sub>7</sub> extended staple strands used as dye-labeled handles (ATTO 647N-(ATT)<sub>7</sub>) in the subsequent hybridization step.

#### DNA origami nanostructures for metal nanoparticle assembly

DNA origami nanostructures were prepared to assemble nanoparticles for the plasmonics section of this thesis (Figure 3.1 (B)). For AuNP and AgNP dimer assembly, particle capture

strands ((AAA)<sub>8</sub>T<sub>4</sub> extended staple strands) were placed where the complementary thiol-modified ssDNA coated nanoparticles were to attach by hybridization in the following step. For AuNR dimer assembly, (AAT)<sub>7</sub>-extended staple strands were also used as capture strands and the AuNRs were coated with (ATT)<sub>7</sub>T<sub>7</sub>-SH (Figure 3.5).

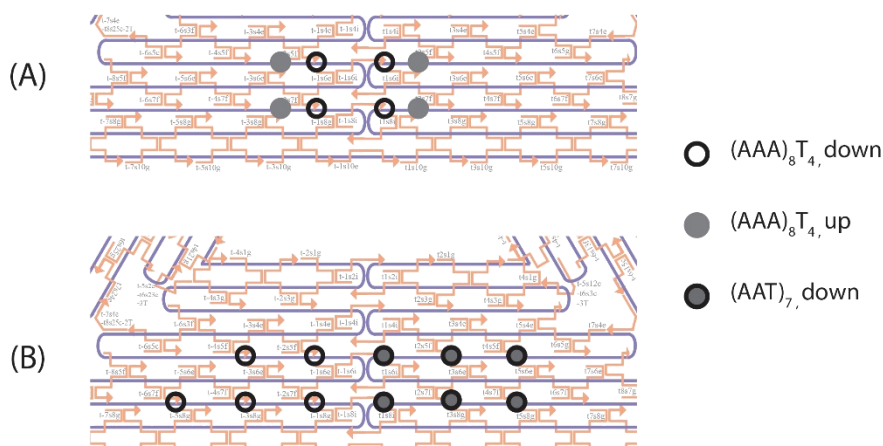


**Figure 3.5.:** DNA origami design for nanoparticle assembly. (A) For assembling dimers of AuNP or AgNP, four particle capture strands faced downwards and four faced upwards of the triangular plane of the origami both with a ((AAA)<sub>8</sub>T<sub>4</sub>) sequence. (B) For assembling dimers of AuNRs, five particle capture strands had a ((AAT)<sub>7</sub>) sequence and six strands had a ((AAA)<sub>8</sub>T<sub>4</sub>), all facing the same direction.

#### 3.2.2. Microbead preparation

Detection of oligonucleotides using a microbead-based assay was conducted in collaboration with Dr. Stefan Rödiger at BTU Senftenberg, Germany. Microbead preparation and the subsequent fluorescence measurements using VideoScan were conducted by Dr. Carsten Schmidt at BTU Senftenberg. Briefly, the streptavidin coupled microbeads (10 - 11 μm) were prepared as previously described by Rödiger et al<sup>90</sup>. The streptavidin used here were recombinantly generated by Dr. Carsten Schmidt according to Gallizia et al<sup>163</sup>. More detailed description of the microbead preparation is given in the Appendix.

Once the microbeads have the target capture strand (Bt-capture) on the surface, they are ready for oligonucleotide detection. The target oligonucleotides (target-A<sub>40</sub>) have a specific sequence of 20 – 22 nb and are extended at the 3'-end with A<sub>40</sub>, for hybridization with Bt-capture and the reporter, respectively. The reporter has a probe sequence (T<sub>40</sub>, probe) and a label (ATTO 647N). The reporter is either a ssDNA strand having one dye label per probe, or a DNA origami structure carrying 14 ATTO 647N dye molecules and a varying number of probe

### 3.2. Sample preparation

strands. Each hybridization step is done for 1 hr at 25 °C in a shaker, followed by three washing steps using centrifugation at 2250 g for 3 min (the supernatant was carefully removed and the remaining pellet was re-suspended in buffer).

Once the samples were ready, they were kept at 4 °C (more details on microbead surface preparation including streptavidin preparation, coupling to the microbeads, and subsequent incubation with biotinylated capture strands can be found in the Appendix).

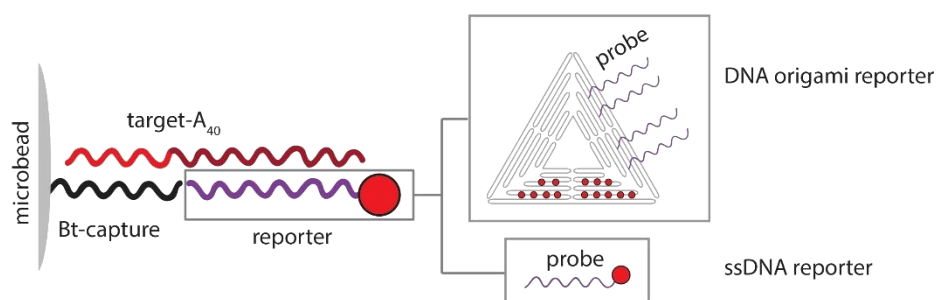


**Figure 3.6.:** Scheme of functionalized microbeads for oligonucleotide detection. Streptavidin coated microbeads are coupled with Bt-capture strand, followed by hybridization of the target-A<sub>40</sub>. Lastly, the reporter is hybridized, and the fluorescence intensity is measured.

#### 3.2.3. AuNR synthesis

Synthesis of the AuNRs was done according to the well-established silver-assisted, seed-mediated methods published by Nikoobakht *et al.*<sup>164</sup> where Au seeds (1-2 nm in size) are first prepared and then grown with directionality into a rod shape. As mentioned in section 2.4.2 the wavelength of LSPR (especially the longitudinal LSPR) is governed by the aspect ratio (AR) of the AuNRs. For the anisotropic growth, AuNRs are CTAB stabilized, which is known to form micelles that are shaped like rods thus promoting anisotropic growth of the spherical seeds<sup>165</sup>. AgNO<sub>3</sub> is also added for the asymmetric growth of the particle<sup>166</sup>.

For the synthesis, a seed solution was prepared by mixing CTAB solution (5 mL, 0.2 M) with HAuCl<sub>4</sub> (5 mL, 0.5 mM) while being stirred. To this solution, freshly prepared ice-cold reducing agent NaBH<sub>4</sub> (0.6 mL, 10 mM) was added after which the solution turns into a brownish yellow color. After vigorous stirring for 2 min, the solution is left at 25 °C for at least 1 h. Growth of the nanorods then follows by preparing the growth solution. This solution is made by adding the appropriate amounts of 4 mM AgNO<sub>3</sub> (0.05 mL or 0.1 mL) solution to CTAB solution (5 mL, 0.2 M) at 25 °C. With the increase of AgNO<sub>3</sub> (100 µl to 150 µl), the AR increases with the wavelength of the longitudinal LSPR. To this solution, HAuCl<sub>4</sub> (5 mL, 1 mM) was added.

### 3. Materials and Methods

After mixing it gently, AA (70  $\mu\text{L}$ , 78.8 mM) was added as a mild reducing agent which turns the growth solution from dark-yellow to colorless<sup>167</sup>. The last step was to add 12  $\mu\text{L}$  of the prepared seed solution to this growth solution at 28  $^{\circ}\text{C}$  and kept overnight at constant temperature. The solution changed its color slowly over time producing a final solution with a blue color. Purification is done by centrifugation (6000 rpm, 10 min, 5 times), discarding the supernatant and resuspending the solution in ultrapure water.

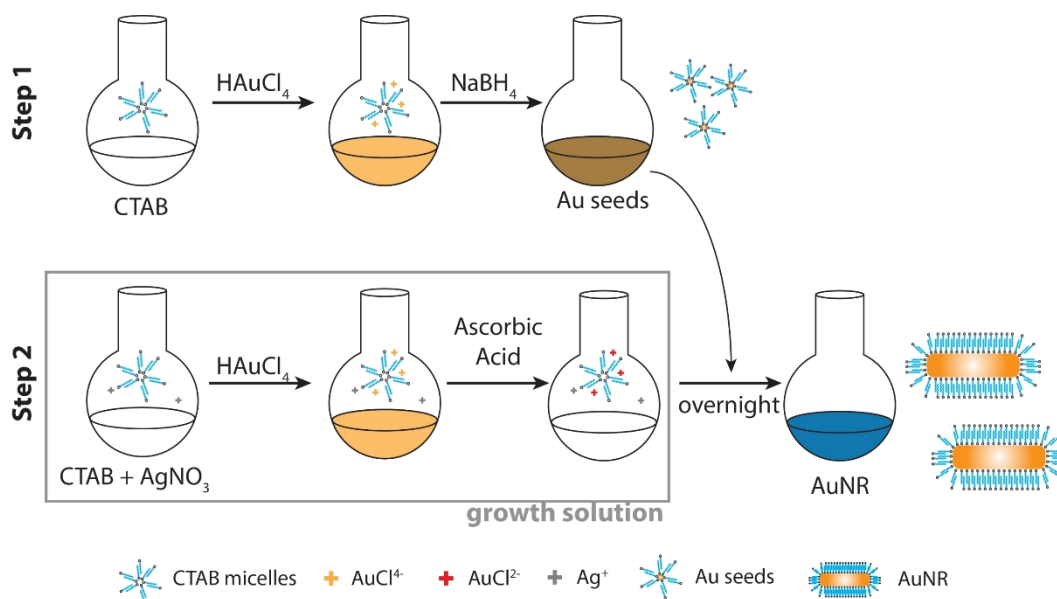


**Figure 3.7.:** Illustration of Ag-assisted, seed-mediated AuNR synthesis process. Step 1 is for Au seed preparation, where  $\text{HAuCl}_4$  is reduced very quickly *via*  $\text{NaBH}_4$  in a CTAB solution. In step 2, this seed solution is added into the growth solution (CTAB,  $\text{HAuCl}_4$ , AA, and the desired amount of  $\text{Ag}^+$ ) to grow into a rod shape.

It is worth noting that sticking rigorously to the protocol and making fresh solutions is very important. Particularly,  $\text{NaBH}_4$  must be prepared in ice-cold water and used within 30 s. As for the surfactant CTAB, it is important to use it from a particular provider as the impurities play a complex role in the synthesis<sup>168,169</sup>. In this work, we used CTAB purchased from SERVA, which was demonstrated before to produce decent AuNRs<sup>170</sup>.  $\text{HAuCl}_4$  is sensitive to light and absorbs water from the air and thus should be kept in a glove box and only be handled using a glass spatula as it is very corrosive<sup>171</sup>. It is also worth noting that scaling-up is not easy and would require many attempts to verify all parameters since this synthesis requires both thermodynamic and kinetic control. Further notes on the synthesis of AuNRs are well documented by Scarabelli *et al*<sup>172</sup>.

## 3.2. Sample preparation

### 3.2.4. Nanoparticles and DNA

All nanoparticles were coated with a thiol-modified ssDNA, utilizing the thiol-metal bond. The coatings are slightly different for the three types of particles (AuNP, AgNP, and AuNR) as the surfaces of the three particles are different from each other. Once the particles are well-coated, they are very stable and can stay as is for months in the fridge and can even be frozen in the case of AuNPs.

#### **AuNP coating**

AuNPs were coated using a modified protocol from Vietz *et al.*<sup>134</sup> where the coating was done at an elevated temperature using the salt-aging method. Citrate stabilized AuNPs were concentrated by 10 fold from the purchased solution and a minimum of 6,000 fold thiol modified ssDNA (100 mM used as provided by the manufacturer) was added along with SDS (final concentration of 0.02 %) and incubated for 30 min at 40 °C in a shaker. 2.5 M NaCl is added in small steps every 3 min until reaching a concentration of 200 mM, then in larger steps until reaching a final concentration of 750 mM. This solution was mixed with an equal volume of buffer (1x TAE, 15 mM MgCl<sub>2</sub>, 0.1 % SDS) and left to shake for another 1 hr. The solution was then washed *via* centrifugation (6000 rpm, 5 min) four times with the last washing step using a different buffer (1x TAE, 15 mM MgCl<sub>2</sub>) to reduce the amount of SDS in the solution.

#### **AgNP coating**

AgNP coating was more difficult than AuNP coating, due to the weaker Ag-sulfur bond compared to that of the Au-sulfur bond<sup>173</sup>. A modified version of the previously described method by Heck *et al.*<sup>28</sup> was used for the coating. Generally speaking, a pre-coating procedure of BSPP at higher concentration of SDS, and sonication between the salt addition steps were required. The pre-coating step was done by mixing the 10 x concentrated citrate stabilized AgNPs (60 nm) with a freshly prepared 2.5 mM BSPP solution (reaching a final BSPP concentration of 0.5 mM). This solution was shaken at 40 °C for 45 min. To this, SDS was added (with a final concentration of 0.2 % SDS) and shaken for 10 min before adding a minimum of 10,000 fold of the thiol-modified ssDNA for at least 1 h. 2.5 M NaCl was added in very small steps every 10 min until reaching 200 mM, then in larger steps until reaching 750 mM. This solution was again mixed with equal volume of buffer (1x TAE, 15 mM MgCl<sub>2</sub>, 0.1 % SDS) and

left to shake for another 1 hr. Purification was done with the same procedure as for AuNPs, but with the same buffer (1x TAE, 15 mM MgCl<sub>2</sub>, 0.1 % SDS) all five times. It is important to note that SH- dT(TAMRA)T<sub>3</sub>(TTT)<sub>8</sub> sequence is very difficult to coat, as TAMRA is charged thereby inducing more aggregation of the particles. In contrast, SH-dT(PEPY)T<sub>3</sub>(TTT)<sub>8</sub> was not as difficult to coat as the dye is not charged.

#### **AuNR coating**

AuNRs were the most difficult of all the different particles that were used in this thesis to coat with thiol-modified ssDNA. As was explained in section 2.4.4, coating of the AuNRs is especially difficult due to the tight CTAB bilayer formed on the surface. A modified version of a protocol published by Shi *et al.*<sup>136</sup>, using low pH buffers for coating was used here. Coating buffer was prepared with a final concentration of 1 x TAE, 0.2 % SDS which was then adjusted to pH 3 using HCl. Concentration of the AuNR was adjusted to 5 nM (concentration determination will be explained in section 3.3.6) and a 10,000 fold thiol modified ssDNA was added along with SDS (final concentration 0.1 %) and shaken at 40 °C for 30 min. Coating buffer was added so that the final concentration of the AuNR is 1 nM and left to shake again at 40 °C for 30 min. Salt was then slowly added in very small steps until reaching a final salt concentration of 500 mM and then left to shake for a minimum of 1 h. This solution was purified using 1x TAE, 15 mM MgCl<sub>2</sub>, 0.1 % SDS five times. As was the case for AgNP coating, multiple sonication steps were required between each salt addition. It is worth noting that coating worked better for freshly synthesized AuNRs, longer ssDNA strands ( > 20 nb), and sequences that only contain T.

#### **Determination of DNA density on nanoparticles**

Determining the number of DNA strands on particles can be done if the thiol-modified DNA also has a dye label that can be detected by measuring the fluorescence emission. A protocol introduced by Hurst *et al.*<sup>154</sup> was used here, especially for the dsDNA coated AuNRs. (TTT)<sub>8</sub>T<sub>4</sub>-SH coated AuNRs were hybridized with a (AAA)<sub>7</sub>A<sub>4</sub>-TAMRA sequence. First, the concentration was determined using the longitudinal LSPR of the synthesized AuNR specific for the synthesis used in this thesis<sup>174</sup>. The DNA coated AuNRs were then exposed to an excess of DTT (0.5 M), which replaces the DNA on the AuNRs and therefore releases the dsDNA into the solution. After centrifuging out the nanoparticles, the supernatant is diluted and the concentration of TAMRA is determined by measuring the fluorescence intensity. A calibration

### 3.2. Sample preparation

curve is determined (0 – 30 nM, with 12 data points in total) and the measured TAMRA fluorescence intensity is plotted against the calibration curve to determine the concentration (Figure A.11).

### Nanoparticle assembly on DNA origami nanostructures

Assembly of DNA coated nanoparticles was done by hybridization with the capture strands that protrude from the DNA origami plane (designs were explained in section 3.2.1). This was done in solution by mixing the DNA origami solution and DNA coated particles in a 1:3 ratio and using the same thermal cycler program as used in step 2 for FRET nanoarray assembly.

### Gel electrophoresis

As mentioned, an excess of DNA coated nanoparticles is given to a solution of DNA origami nanostructures to assemble the nanoparticle dimer structures. The unbound nanoparticles were removed by agarose gel electrophoresis (Biorad Mini-Sub Cell GT electrophoresis chamber). A 0.5 % agarose gel (in 1x TAE with 15 mM MgCl<sub>2</sub>, 60 mL) was used and was run at 40 V for 2.5 h in a cold water bath. Loading of the sample was done with a 5 part 6x loading buffer (30 % Glycerine, 1x TAE, 15 mM MgCl<sub>2</sub>) and 1 part sample to make sure the sample stays inside the pocket of the gel. The band of interest is then cut out and placed on a parafilm wrapped microscopy slide and a second parafilm wrapped microscopy slide is used to squeeze out the solution (red for AuNP and blue for AuNR). A gentle centrifugation was done to remove all the gel particles and the supernatant was collected. Figure 3.9 shows an example of the gel electrophoresis of AuNP dimers and AuNR dimers on DNA origami nanostructure.

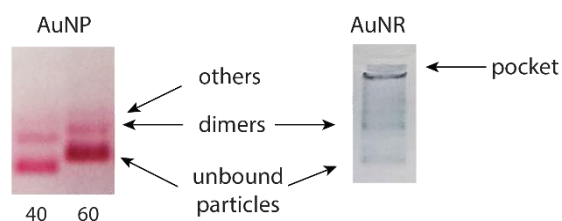


**Figure 3.8.:** Gel electrophoresis of AuNP (40, 60 nm) and AuNR dimers assembled on DNA origami nanostructures. The strongest band contains the unbound particles which is followed by the dimer structures. The next band includes structures with more than one DNA origami nanostructure per particle.

It must be noted that DNA origami nanostructures with dimers cannot be separated from DNA origami nanostructure with one nanoparticle and appear within one band. Separation happens according to the number of DNA origami nanostructures per cluster that forms. In

addition, it can be postulated that the nanoparticle is not coated fully if there is a band that is left in the pocket as shown for AuNRs.

## 3.3. Methods

### 3.3.1. Steady-state fluorescence spectroscopy

Steady-state fluorescence spectroscopy measurements were performed with a spectrophotometer (Fluoromax P, HORIBA Jobin Yvon) with 3 mm quartz cuvettes (Hellma Analytics). Fluorescence emission was collected at a right angle to the excitation beam using an internal quantum correction system. For FRET nanoarray analysis using FAM and Cy3 as the dye molecules, an excitation wavelength ( $\lambda_{\text{ex}}$ ) of 450 nm was chosen, and for ratiometric pH sensing with C343 and FAM,  $\lambda_{\text{ex}} = 400$  nm was chosen. For collecting excitation spectra, the emission wavelengths ( $\lambda_{\text{em}}$ ) were set to 600 nm and 550 nm, respectively. For quantification of TAMRA (for calculating DNA density on nanoparticles), emission spectra were collected at  $\lambda_{\text{ex}} = 545$  nm. For all spectra, acquisition at an increment of 1 nm, integration time of 0.2 s, and bandpass of 5 nm were used.

### 3.3.2. Time-correlated single photon counting

Time-correlated single photon counting (TCSPC) measurements were performed to obtain fluorescence decay lifetimes of the fluorophores. Due to its unique measurement technique, a brief description is given here.

In a TCSPC measurement, the sample is repetitively excited with a short-pulsed laser which is followed by precise timed registration of single photons. The time difference between the excitation of the sample and the resulting photon is then stored in a histogram where the x-axis is the time difference and the y-axis is the number of photons detected for that time difference. It is therefore important to detect only one photon per excitation laser pulse, which leads to a detection rate of typically 1 photon per 100 excitation pulses<sup>10</sup> and multiple repetition ( $10^5 - 10^7$ ). This technique can be thought of as a stop watch, with the excitation pulse starting the clock and the detection of emitted photon stopping the clock. A typical setup of a TCSPC is shown in Figure 3.9.

A measurement starts with the excitation pulse exciting the sample and sending a signal to the electronics. This signal is then passed through a constant function discriminator (CFD)



### 3.3. Methods

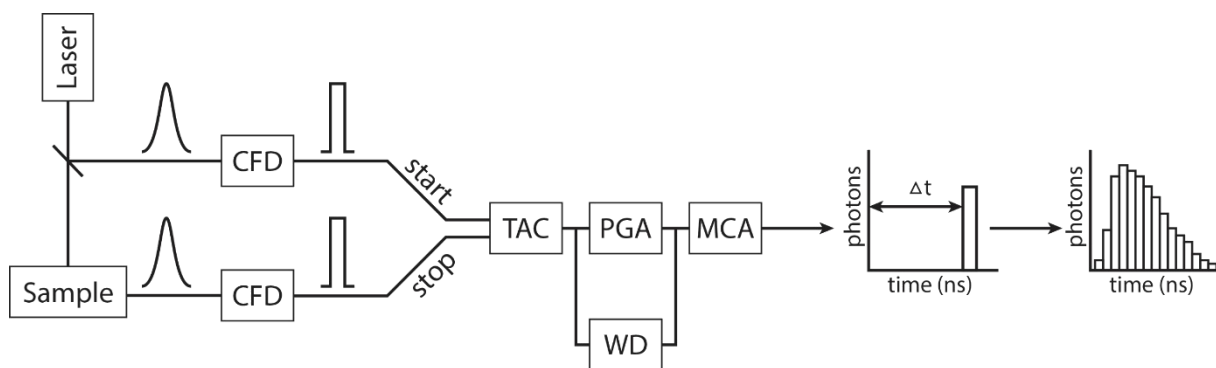


**Figure 3.9.:** Schematic illustration of a TCSPC setup (CFD: constant function discriminator, TAC: time-to-amplitude converter, PGA: programmable gain amplifier, WD: window discriminator, MCA: multichannel analyzer).

which measures the time of the pulse arriving (start). This is then passed to a time-to-amplitude converter (TAC) which generates a growth of a voltage ramp signal that linearly increases with time. A second channel detects the single photon emitted from the sample, which again is passed through a CFD sending a stop signal to the TAC. The TAC holds the information regarding the time delay between sample excitation and photon detection. The voltage generated by TAC can be amplified by a programmable gain amplifier (PGA) and further sent to a multichannel analyzer (MCA). Signals that do not fall in a given range of voltages is sent through a window discriminator (WD) to reduce false readings.

Measurements were conducted in this work using the FLS920 fluorescence lifetime spectrometer (Edinburgh Instruments, F900 software) equipped with a supercontinuum laser SC-400-PP (0.5-20 MHz,  $400 \text{ nm} < \lambda < 24\,000 \text{ nm}$ , pulse width *ca.* 30 ps, Fianium/NKT Photonics A/S), with the same quartz cuvette as used in obtaining steady-state fluorescence spectra. Fluorescence emission was collected at a  $90^\circ$  angle to the excitation beam using a multichannel plate (ELDY EM1-132/300, Europhoton). The excitation wavelength for FRET nanoarray analysis (FAM - Cy3) was set to 490 nm and the emission wavelength to 520 nm. For proof-of-concept ratiometric pH sensing (C343 - FAM), an excitation wavelength of 450 nm and an emission wavelength of 490 nm were chosen. The fluorescence decay curves can be written as an intensity-time function,

$$I(t) = \sum_{i=1}^n A_i e^{-\frac{t}{\tau_i}} \quad (3.1)$$

Where  $\tau_i$  is the decay time component and  $A_i$  the amplitude of each component. The amplitude averaged decay time is then given as,

$$\bar{\tau}_{DA} = \frac{\sum_{i=1}^n A_i \tau_i}{\sum_{i=1}^n A_i}. \quad (3.2)$$

When analyzing the fluorescence decay curves, the instrument response function (IRF) must be taken into account, as the excitation pulse is not infinitely short. IRF is taken using a scattering sample, and this represents the shortest time profile that can be measured by the instruments.

#### 3.3.3. VideoScan technology

Oligonucleotide detection using microbead-based assays were conducted using a patented technology termed VideoScan (Based at BTU Senftenberg). The setup consists of an inverse fully motorized fluorescence microscope (Olympus IX81, Olympus) with at least three fluorescence channels that is illuminated by a xenon arc lamp (75  $\mu$ W), a motorized scanning stage (SCAN IM 120 x 100, Märzhäuser), and a grayscale DX2HC digital camera (Kappa) equipped with a Sony ICX285AL charge-coupled device (CCD) chip. For microbead measurements the 10x objective (Olympus, NA = 0.3) is used. This hardware component is coupled with the software package *FastFluoScan* developed by Rödiger *et al.* <sup>24</sup>.

The three fluorescence channels of the microscope are necessary as the first two channels are required to identify the dual color encoded microbeads (color 1:  $\lambda_{\text{ex}} = 420 - 480$  nm,  $\lambda_{\text{em}} = 485-540$  nm and color 2:  $\lambda_{\text{ex}} = 515 - 540$  nm,  $\lambda_{\text{em}} = 535-570$  nm), and the third channel is responsible for the analyte fluorescence which in this thesis was ATTO 647 N ( $\lambda_{\text{ex}} = 625 - 660$  nm,  $\lambda_{\text{em}} = 660 - 700$  nm).

The measurement was done by first taking an image with the filter set matched to color 1 after automatic focusing. Microbeads could be identified by their circular shape, whilst all other shapes were excluded from further processing. A second image of the same area was then taken with the filter set to match color 2. Gray values (white and black is given as 0 % and 100 % on the greyscale, respectively) of each channel were then determined in the center of each detected microbead and used for identification. The identified microbeads were then grouped into one microbead population. This eliminates the problem of the fluctuation of fluorescence excitation intensity as the ratio of the intensity is used, never the absolute value. Lastly, the fluorescence intensity of the labeled analyte is determined by taking a third image of the same area but with the third channel with the filter set to match ATTO 647N. A typical

### 3.3. Methods

integration time is 500 ms. As these dyes are only on the surface of the microbeads, in contrast to the encoding dyes that are inside, it creates a halo around the microbead.

A minimum of 100 microbeads were prepared for each target oligonucleotide, and once ready for measurement are transferred into microtiter plates (96-well plate) with a clear bottom. Measurements were conducted after waiting for 10 min for the microbeads to settle to the bottom of the well.

#### 3.3.4. Atomic force microscopy

Atomic force microscopy (AFM) imaging was performed with a Nanosurf FlexAFM with a C3000 controller (Nanosurf). Tapping mode was used, and imaging was done under dry conditions using a Tap 150 Al-G cantilever (Budget Sensors) with a resonance frequency of 150 kHz and spring constant of  $5 \text{ Nm}^{-1}$  with a tip size of 10 nm. Two different substrates were used for imaging, mica (Plano) or silicon (CrysTec, (100)-orientation, p-doped with boron). A quick check to confirm the DNA origami nanostructure shapes were mostly done on mica by adsorbing 2  $\mu\text{L}$  of sample and 28  $\mu\text{L}$  of buffer (1 x TAE, 15 mM  $\text{MgCl}_2$ ) and incubated for 30 s. This was washed with ultrapure water (3 mL) and dried with compressed air. Nanoparticle assemblies on DNA origami nanostructures were imaged on silicon substrates. This requires pre-treating the Si wafers, by cutting them in 0.5 cm x 0.5 cm squares, washing them with 1:1 ethanol:ultrapure water mixture, drying them with compressed air then and finally exposing them to air plasma (Zepto, Diener electronic) for 5 min. 1  $\mu\text{L}$  of sample was adsorbed on the substrate along with 30  $\mu\text{L}$  of 1x TAE 50 mM  $\text{MgCl}_2$  buffer in a wet chamber for 1 h. This was washed with 3 mL of 1:1 EtOH:ultrapure water mixture and dried with compressed air. This substrate was then very gently scratched with a diamond cutter in order to be able to correlate the AFM image with Raman mapping. For the quick DNA origami nanostructure shape check, the images were recorded for an area of 4  $\mu\text{m}$  x 4  $\mu\text{m}$ , 512 data points/line, with a scan speed of  $\sim 0.6 \text{ s/line}$ . P-Gain (proportional gain) and I-Gain (integral gain) were in the ranges of 500 – 800. For imaging nanoparticle assemblies, an image size of 10  $\mu\text{m}$  x 10  $\mu\text{m}$  was recorded at a slower scan speed (0.9 – 1.2 s/line). The recorded images were analyzed and visualized using Gwyddion 2.42 software (open-source).

### 3.3.5. Raman spectroscopy

Raman measurements were performed with a WITec alpha 300 confocal Raman microscope using a 100x objective (Olympus MPlanFL N, NA = 0.9), with a 50  $\mu\text{m}$  pinhole, 600 gr/mm grating at an excitation wavelength of 532 nm. An area of 25  $\mu\text{m}$  x 25  $\mu\text{m}$  was typically scanned at an end of a scratch made on the silicon chip with a laser power of 25  $\mu\text{W}$  and an integration time of 4 s (with a step size of 0.833  $\mu\text{m}$ ). The diffraction limited spot size was 1.3  $\mu\text{m}^2$  as was determined by Dr. Julia Prinz. A notch filter was used to suppress the Rayleigh scattering intensity. Scattered light was coupled into a multi-mode optical fiber and directed into the spectrometer (UHTS 300) and detected by a CCD camera (DV401-BV). As the scratch made on the silicon chip can be detected by a sharp decrease in the silicon Raman scattering intensity, the resulting Raman map can be overlaid with the AFM image.

### 3.3.6. UV-Vis extinction spectroscopy

In order to determine the concentration of the DNA origami nanostructures, AuNPs, AgNPs, and AuNRs, extinction spectra were obtained using Nanodrop200c spectrophotometer (Thermo Fisher Scientific) with an optical path of 1 mm. Using the Beer-Lambert law, concentration can be determined as,

$$A = \epsilon_{\lambda} \cdot l \cdot c \quad (3.1)$$

where  $A$  is the extinction,  $l$  the optical path length ( $\text{cm}^{-1}$ ),  $\epsilon_{\lambda}$  the extinction coefficient ( $\text{nM}^{-1}\text{cm}^{-1}$ ) at a given wavelength  $\lambda$  (nm), and  $c$  the concentration (nM).

For DNA origami nanostructures, nucleic acid data for the scaffold strand M13mp18 was used as was given by the provider ( $\text{MW} \approx 4.4 \times 10^6$  g/mol, dsDNA  $\epsilon_{260} = 0.02$   $\mu\text{L}/\text{ng}\cdot\text{cm}$ ).

AuNP concentrations were determined according to the  $\epsilon_{\lambda}$  determined by Liu *et al.*<sup>175</sup>, AgNP according to Paramelle *et al.*<sup>176</sup>, and AuNR according to Orendorff *et al.*<sup>174</sup>. The used  $\epsilon_{\lambda}$  in this thesis according to material and size of the particles are listed in Table 3.2.

**Table 3.2.:** Extinction coefficients  $\epsilon_{\lambda}$  at wavelengths  $\lambda$  used for concentration determinations.

	AuNP			AgNP	AuNR
	40 nm	60 nm	80 nm	60 nm	LSPR 680
$\epsilon_{\lambda}$ ( $\text{nM}^{-1}\text{cm}^{-1}$ )	10.3	39.6	103	73.9	2.92
$\lambda$ (nm)	508	508	508	432	680

### *3.3. Methods*

#### **3.3.7. Transmission electron microscopy (TEM)**

TEM measurements for AuNR characterization were carried out by Dr. Dennis Klier, using the core facility for electron microscopy at the Charité - Universitätsmedizin Berlin, with the Leo EM 906 (Carl Zeiss). Typical gold nanoparticle measurements are done at an acceleration voltage of 200 kV. At least 3 images were taken for each batch of synthesized AuNRs, and a minimum of 100 particles were analyzed.

# 4. Results

## 4.1. FRET nanoarrays and ratiometric sensing

As was explained earlier in section 3.2.1, the dye molecules were arranged on the DNA origami nanostructures and their optical properties of the arrays were studied in relation to the size of the array. The arrays were constructed on the DNA origami nanostructure by extending selected staple strands at their 5'-end either with a (AAT)<sub>7</sub> or (CAA)<sub>7</sub> sequence that acted as handles to place dye molecules. Compared to directly modifying the staple strand with the dye molecule, this strategy allows for construction of a large number of different FRET nanoarrays without having to modify each staple strand with the dye molecule (Figure 4.1).

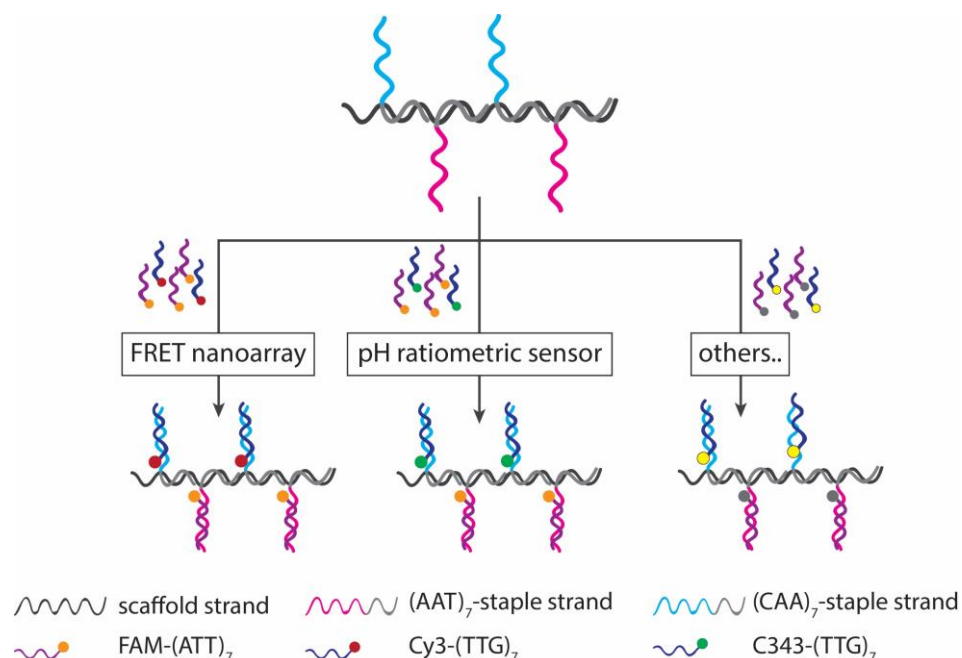


**Figure 4.1.:** Illustration of the versatility of the DNA origami nanostructure design. Once the DNA origami nanostructure is folded with the extended dye handles, various dye molecules can be arranged by hybridizing with complementary strands that are modified with the dye molecule (FAM: orange circle, Cy3: red circle, C343: green circle, other dyes : yellow and blue circles).

#### 4.1. FRET nanoarrays and ratiometric sensing

This folding process is therefore more flexible, efficient, and cost-effective. In this study, optical properties of the FRET nanoarrays of different sizes (ranging from a **(2x1)** array to a **(3x4)** array, with a Do to Ac ratio held at 1:1) were analyzed using fluorescein (FAM) and cyanine 3 (Cy3) as the FRET pair (arrays shown in Figure 3.2). The ssDNA strands (ATT)<sub>7</sub> and (TTG)<sub>7</sub> were labeled with FAM and Cy3 respectively, and hybridized to protruding handles of the DNA origami nanostructure. Using the optimum design determined using this FRET pair, the system was tested out as an internally referenced ratiometric sensor using an appropriate dye pair coumarin 343 (C343) and FAM (extended by (TTG)<sub>7</sub> and (ATT)<sub>7</sub>, respectively). Analysis of the nanoarrays and ratiometric sensors was conducted using both steady-state emission spectroscopy and time-resolved fluorescence studies <sup>177</sup>.

##### 4.1.1. FRET nanoarray analysis

For studying the influence of the size and the pattern of the dye nanoarray on their optical properties, a systematic study was conducted using FAM as the Do and Cy3 as the Ac. By arranging the dye molecules in arrays, with the ratio of the Do and Ac kept at 1:1 in a checkerboard pattern, a combination of effects happen that lead to a change in the FRET efficiency and the emission intensity ratio of Do and Ac. A Light-harvesting effect will take place by arranging multiple donors around one acceptor, which allows for energy from the donor to be funneled into the acceptor leading to an enhanced acceptor emission <sup>20</sup>. On the other hand, FRET efficiencies will increase if multiple acceptors are placed around one donor as the number of energy transfer pathways increases <sup>10</sup>. By increasing the size of the nanoarray whilst keeping the checkerboard pattern, the number of Ac molecules surrounding a Do molecule increases up to four (and vice versa) within the spatial dimensions where FRET can take place.

The excitation and emission spectra of FAM and Cy3 are shown in Figure 4.2 (A), with the spectral overlap shown in grey. The Förster radius of this FRET pair is 6.7 nm <sup>178</sup>. The distances between the dye molecules shown in Figure 4.2 (B) are 6 nm for the two closest dye molecules (same plane), 7.7 nm for neighboring Do and Ac along the same DNA double helix, and 9.7 nm for the two dye molecules that are 'diagonal' to each other (given that the interhelix distance is 1 nm <sup>8</sup>).

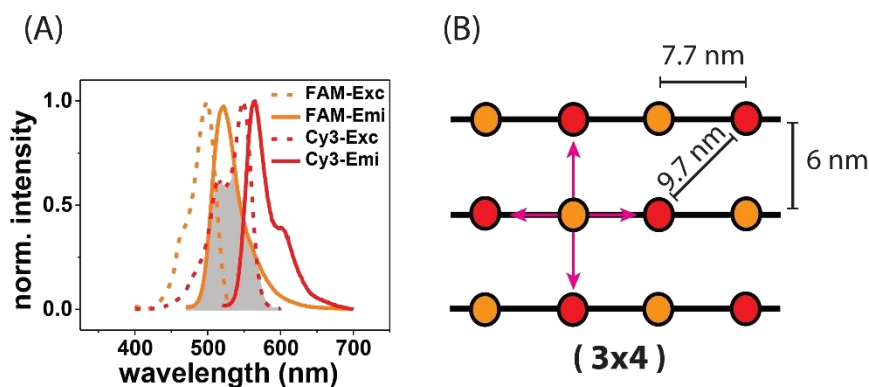


**Figure 4.2.:** FRET nanoarray design. (A) Excitation and emission spectra of the FRET pair FAM ( $\lambda_{\text{exc}} = 450 \text{ nm}$ ,  $\lambda'_{\text{emi}} = 580 \text{ nm}$ ) and Cy3 ( $\lambda_{\text{exc}} = 500 \text{ nm}$ ,  $\lambda'_{\text{emi}} = 620 \text{ nm}$ ) with the spectrum overlap colored in grey. (B) FRET nanoarray with 1:1 ratio of FAM : Cy3 in a checkerboard pattern of a **(3x4)** nanoarray. Pink arrows show the energy transfer pathways for one donor to four acceptors. The different distances between the dye molecules are shown that are within the dimensions where FRET can take place (6 nm, 7.7 nm, and 9.7 nm with an interhelix distance of 1 nm<sup>8</sup>).

The normalized emission spectra ( $\lambda_{\text{exc}} = 450 \text{ nm}$ ) of the different nanoarrays, ranging from a simple FRET pair **(2x1)** to a nanoarray of 6 FRET pairs **(3x4)** are shown in Figure 4.3 (A) (all the arrays assembled are shown in Figure 4.3 (D) that are color coded and used throughout accordingly). By exciting the Do, energy is transferred to the Ac resulting in an emission profile with two distinct peaks. Here, the profiles showed a high fluorescence intensity at 515 nm arising from FAM (the D) and a second rise in the intensity at 565 nm from Cy3 (the A). As the array grew larger, the intensity ratio  $I(565 \text{ nm})/I(515 \text{ nm})$  increased from  $0.9 \pm 0.01$  by 44 % to  $1.6 \pm 0.03$ . The increase in the overall fluorescence of the nanoarray was reflected by the relative decrease of the contribution of the water Raman peak that could be observed as a sharp peak at 520 nm (marked with an asterisk) to the measured fluorescence signal as the array became larger.

Subsequently, time-resolved studies with the FRET nanoarrays were also performed with the resulting decay curves shown in Figure 4.3 (B). The decay analysis was conducted using a multi-exponential fit with four decay components with the last decay component fixed to unquenched FAM fluorescence decay time ( $\tau_D = 4.5 \text{ ns}$ ). The decay profiles rapidly decreased in the donor fluorescence lifetime between the **(2x1)** array (dark blue,  $\bar{\tau}_{DA} = 2.8 \pm 0.2 \text{ ns}$ ) and **(2x2)** array (light blue,  $\bar{\tau}_{DA} = 1.8 \pm 0.02 \text{ ns}$ ). After this point, the change in the fluorescence lifetime is not as significant reaching a minimum value for the **(3x4)** array (magenta,



#### 4.1. FRET nanoarrays and ratiometric sensing

$\bar{\tau}_{DA} = 1.5 \pm 0.01$  ns). The average lifetimes determined here account for the multiple energy transfer pathways due to arranging the dyes in this checkerboard pattern, as well as the labeling yield being inevitably less than 100 %.

These determined averaged lifetimes were used for calculating FRET efficiencies ( $E$ ) according to equation 2.9. As shown in Figure 4.3 (C) the  $E$  values increased by 22 % from  $0.52 \pm 0.01$  for the **(2x1)** array to  $0.67 \pm 0.001$  for the **(3x4)** array. The intensity ratio  $I(565 \text{ nm})/I(515 \text{ nm})$  showed increasing values without reaching a plateau. This discrepancy between the saturating trend of  $E$  and the continuously increasing emission intensity ratio can be attributed to a light harvesting effect taking place since this effect, whilst enhancing the emission intensity of the acceptor does not affect the  $E$  <sup>21</sup>.

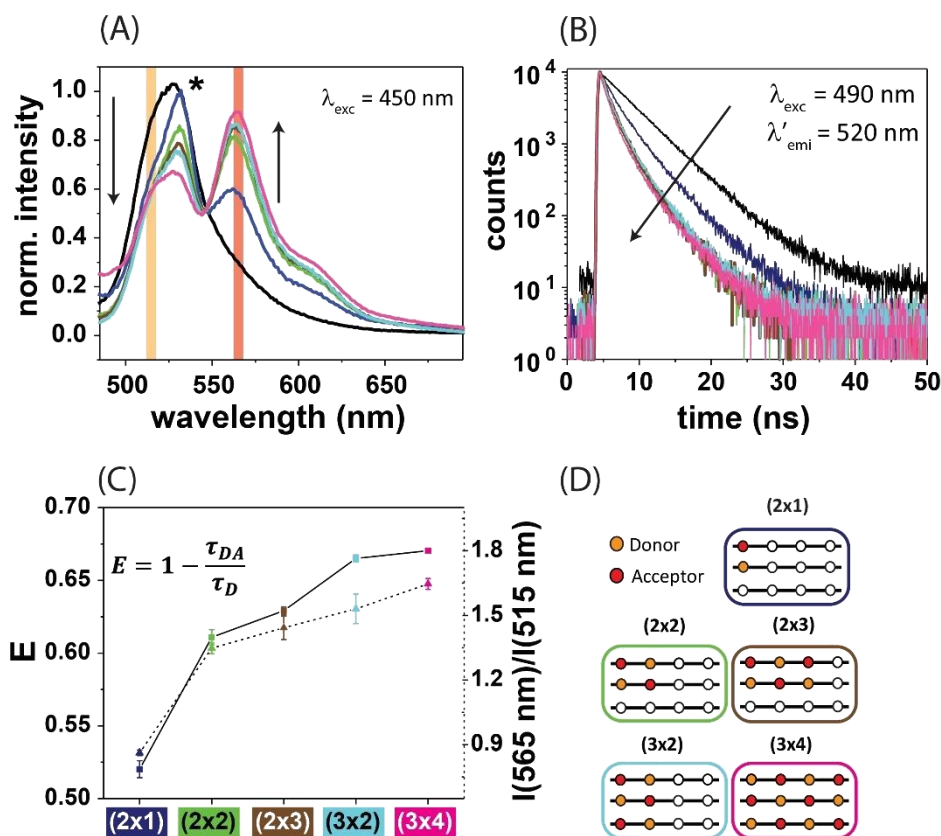


**Figure 4.3.:** FRET nanoarray analysis. (A) Normalized emission spectra for FRET nanoarrays on DNA origami nanostructures ( $\lambda_{exc} = 450$  nm). The emission intensity at 515 nm (FAM) decreased and the intensity at 565 nm (Cy3) increased as the size of the nanoarray increased. The black line represents emission of FAM in absence of Cy3. A sharp water Raman peak at 520 nm was visible for smaller nanoarrays, which indicated the relatively low fluorescence intensity of those nanoarrays. (B) Fluorescence decay curves obtained for FAM ( $\lambda_{exc} = 490$  nm,  $\lambda'_{emi} = 520$  nm). Lifetimes of FAM decreased as the size of the nanoarray increased. (C) FRET efficiencies ( $E$ ) and intensity ratio. FRET efficiencies were calculated based on amplitude averaged decay times, which reached a saturation point at a **(3x2)** array (light blue). The intensity ratio between FAM and Cy3 increases further. (D) The nanoarrays used here ranging from the simple FRET pair **(2x1)** array to **(3x4)** array which are color coded as used in (A)-(C).

Analytical and complex numerical solutions were developed as early as 1980s for FRET in two and three dimensions with many efforts dedicated to verify them experimentally<sup>179–181</sup>. The significant advantage of using DNA origami nanostructures to arrange dye molecules is that the exact locations of the dyes are known. In fact for the **(3x4)** array, the estimated FRET efficiency corresponds well with the Monte Carlo simulations performed for two-dimensional FRET array where the distribution of dye molecules were chosen at random<sup>180</sup>. Using the advantage of utilizing DNA origami nanostructures, a simple method to estimate the behavior

#### 4.1. FRET nanoarrays and ratiometric sensing

of  $E$  of the nanoarrays with predetermined locations of Do and Ac is proposed. As illustrated in Figure 4.4,  $E$  is estimated using equation 2.8. For predicting the behavior of  $E$ , a circle with a radius of 10 nm which corresponds to a FRET efficiency of 10 % is drawn with the dye molecule placed in the center. The ratio of the overlapping area ( $A_{ovlp}$ ) of the circles (area within the dotted lines) over the total area ( $A_{tot}$ ) is then determined.

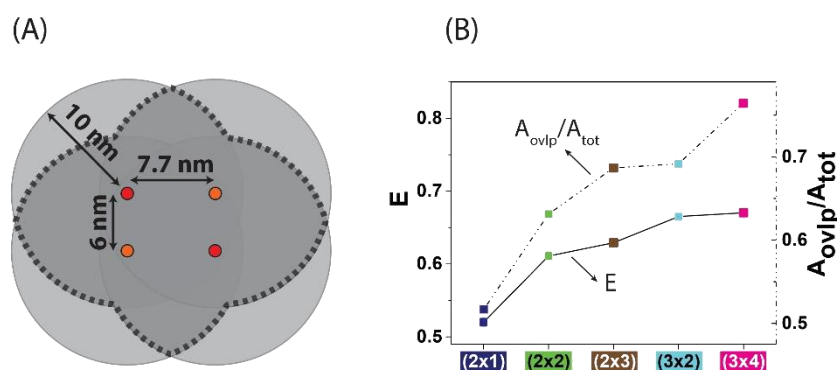


**Figure 4.4.:** Estimation of  $E$  according to the size of the nanoarrays. (A) (2x2) array is taken here as an example of the estimation method. Red and orange circles represent the dye molecules in the center of the light grey circle. The distances between the dye molecules are as they would be on the DNA origami nanostructures (6 nm and 7.7 nm). The grey circle drawn around the dye molecule as the center point, with a radius of 10 nm where  $E$  would be less than 10 % for the given FRET pair. The total area for this array is the total grey area ( $A_{tot}$ ) and the overlapping area is the darker grey area within the dotted line ( $A_{ovlp}$ ). (B)  $E$  calculated from donor decay lifetimes (solid line) and  $A_{ovlp}/A_{tot}$  is plotted according to the array.

This proposed approach provides a quick insight into the changes of  $E$  as a function of the number of total dye molecules that are at a known fixed position on a two-dimensional platform. This can be easily adapted to larger arrays with multiple dye molecules and various Do-Ac distances. It must be noted however that this method does not provide an exact solution for  $E$  of the nanoarrays, since it cannot accurately represent the  $R^{-6}$  distance dependence of  $E$  between the Do and the Ac.

In addition to the effect of increasing size of the nanoarray, the effect of arranging the dye molecules in a different pattern than a checkerboard on the optical properties have been studied (Figure 4.5). For smaller arrays, up to three FRET pairs, the arrangement that could provide best light harvesting effect (maximum number of Do surrounding one Ac) as well as maximum  $E$  (maximum number of Ac surrounding one Do) is a checkerboard pattern of the Do and Ac. However, if the nanoarray size increases to six FRET pairs the energy transfer

pathways become more complex. This can also be postulated from the  $E$  saturating, whereas the emission intensity ratio of Do and Ac kept increasing with the increase of the nanoarray size (Figure 4.3 (C)). Therefore, the effect of the arrangement of the dye molecules on the optical properties of the nanoarrays were studied (while still keeping the Do:Ac at 1:1) for the **(3x4)** array. The least efficient arrangement showed similar  $E$  to **(2x1)** array, also proving that at a distance of 9.7 nm there is minimum energy transfer between the Do and Ac. One of the arrays, **(3x4)\_g**, showed a larger intensity ratio than the checkerboard pattern, **(3x4)\_f**, however there was no significant difference in  $E$ .

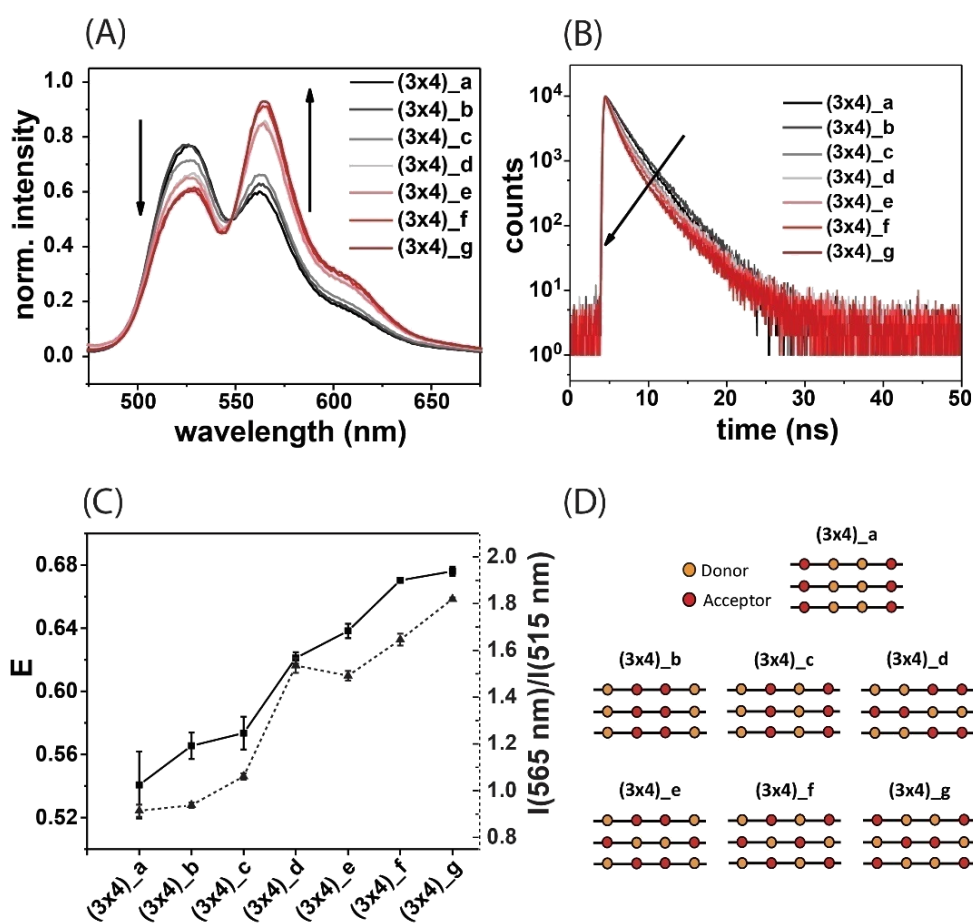


**Figure 4.5.:** Effects of arranging the dye molecules of the **(3x4)** array in various patterns. (A) Steady-state emission spectra recorded showing a decrease of the Do emission at 515 nm and increase of the Ac emission at 565 nm according to the dye arrangement. (B) Lifetime decay curves of Do were obtained, showing a decreasing trend. (C) The  $E$  values obtained from averaged lifetimes and the emission intensity ratio of Do and Ac plotted according to the array. The  $E$  reaches maximum for the **(3x4)\_f** array but the intensity ratio is higher for **(3x4)\_g** than the checkerboard patterned **(3x4)\_f**. (D) The seven different Do and Ac arrangements of the **(3x4)** array. Measurements were conducted using same parameters as in Figure 4.3.

## 4.1. FRET nanoarrays and ratiometric sensing

### 4.1.2. Application as a ratiometric pH sensor

Based on the FRET-analysis of the nanoarrays, the **(3x4)** array with a checkerboard pattern (the **(3x4)\_f** array as was shown in Figure 4.5) was the optimum design to test out as a ratiometric sensor. Although the **(3x4)\_g** array (Figure 4.5) showed higher intensity ratio than the checkerboard pattern, the checkerboard design is expected to have no self-quenching as the closest distance between the same type of dyes is 9.7 nm. C343 and FAM were chosen as the FRET Do and Ac, respectively, to determine the pH in the range of 5-8. This pH range is of particular interest as it is biologically relevant<sup>6</sup>, e.g., pH of intracellular compartments differing from pH 4.7 (lysosome) to pH 8 (mitochondria)<sup>182</sup>. The Förster radius of C343-FAM is 5.0 nm, which was determined using PhotochemCAD. C343 is a pH unresponsive dye and therefore acts as an internal reference signal for the ratiometric sensor<sup>183</sup>. FAM is a pH responsive dye and therefore acts as the indicator of the proton concentration in the solution<sup>184</sup>. It forms different acid-base equilibria in the ground state, with one particular form of the dye predominating at each pH. This leads to different absorption spectra of FAM according to the pH (Figure A.2)<sup>185</sup>. The normalized excitation and emission spectra of the FRET pair are shown in Figure 4.6 (A) along with the different FRET pair arrangements on the DNA origami nanostructure in Figure 4.6 (B) ranging from a simple FRET pair array **(2x1)** and their multiples, to the checkerboard patterned **(3x4)** array. DNA origami nanostructures with two FRET pairs are referred to as **2 x (2x1)**. DNA origami nanostructures with six FRET pairs not interacting with other are referred to as **6 x (2x1)**, which also has the same number of dye molecules as for the **(3x4)** array. These FRET pairs within the two arrays **2 x (2x1)** and **6 x (2x1)** were not expected to interact with each other as they were at least 18 nm apart from each other.

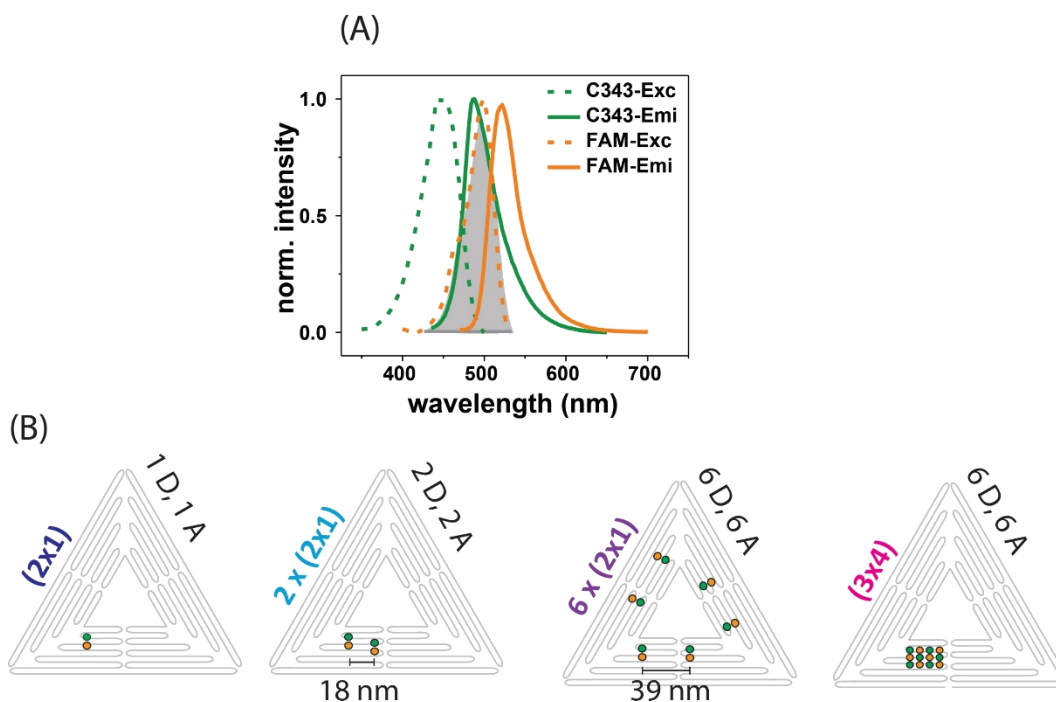


**Figure 4.6.:** Ratiometric pH sensing was conducted using C343 and FAM as the Do and Ac, respectively. (A) Normalized excitation and emission spectra were recorded here with the spectral overlap shown in grey. (B) Dye arrangements on the DNA origami nanostructure ranging from **(2x1)** to multiples of this, **2 x (2x1)** and **6 x (2x1)**, to a checkerboard patterned **(3x4)** array. The nanoarrays are also color-coded and used throughout this section, with green circles representing C343 and orange circles FAM. Each array is noted with the number of Do and Ac, and the distance between the FRET pairs (18 nm and 39 nm).

The normalized emission spectra ( $\lambda_{exc} = 400$  nm) of the nanoarrays are shown in Figure 4.7 (A)-(D). All arrays showed a single peak in the emission spectrum at 490 nm at pH 5 arising from C343, since FAM is quenched at low pH. The pH independent fluorescence emission of C343 and pH dependent fluorescence emission of FAM is shown in Figure A.3. With increasing pH, the peak at 490 nm decreased and a second more pronounced peak at 520 nm appeared due to the acceptor FAM recovering its fluorescence emission. As is shown in Figure 4.7 (A) the sharp water Raman peak (marked with an asterisk) at 464 nm decreased relatively as the array became larger, indicating that the overall fluorescence intensity increased. The emission spectra changed their profile with the increase in pH, more dramatically for the **(3x4)** array than the **2 x (2x1)** array. The intensity ratio between the Do at 487 nm and Ac at 520 nm are plotted according to the pH values for the different nanoarrays (Figure 4.7 (E)), which increased with increasing pH value. The data was also fitted with an exponential function to indicate the different sensitivities of each nanoarray, showing an

## 4.1. FRET nanoarrays and ratiometric sensing

increasing trend in the sensitivity with the increasing number of FRET pairs. As expected, a significant increase in the sensitivity was shown by arranging the dye molecules in a checkerboard pattern as can be seen by directly comparing the **6 x (2x1)** array to **(3x4)** array.

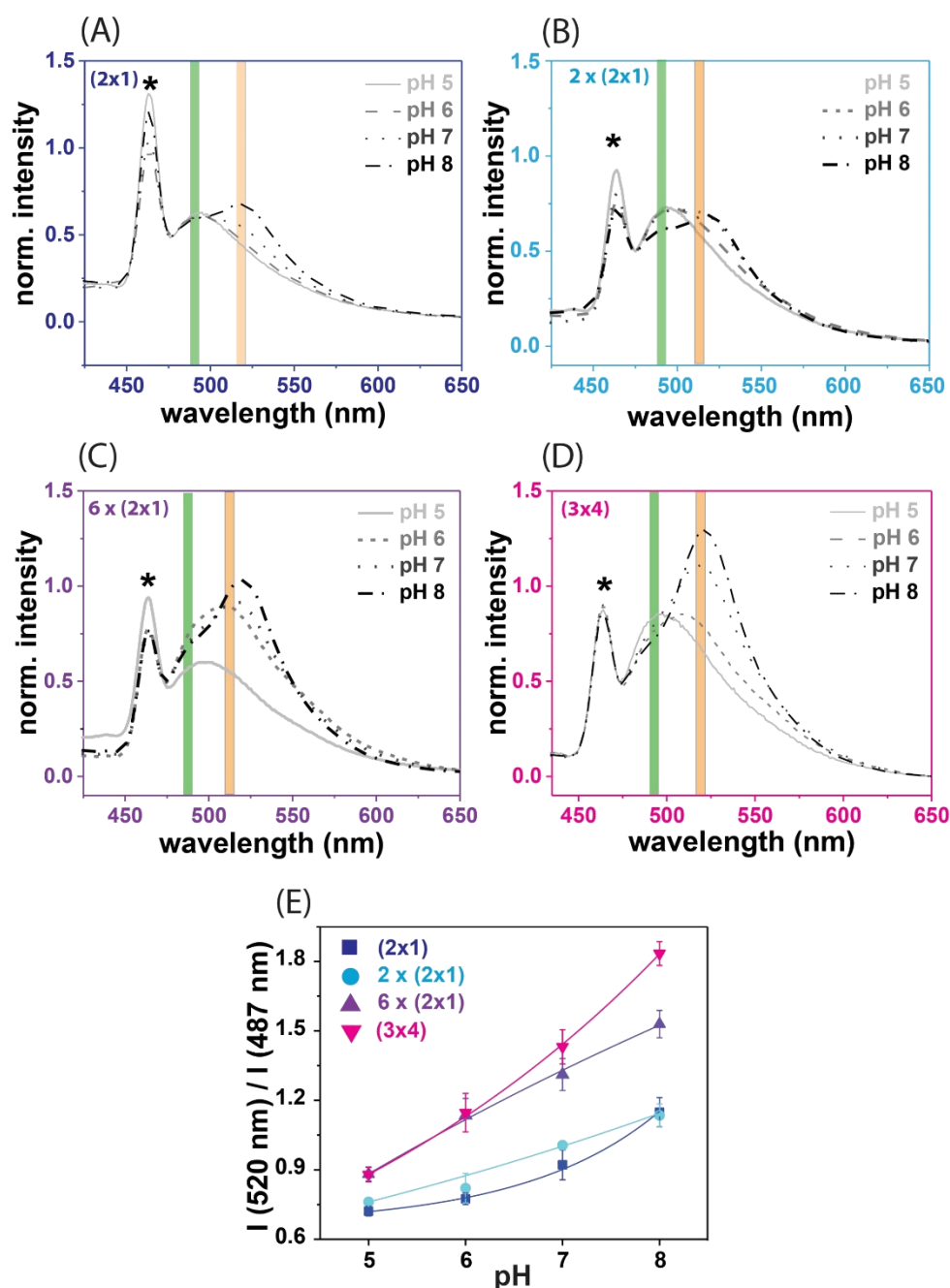


**Figure 4.7.:** FRET nanoarray for pH ratiometric sensing. (A)-(D) Normalized steady-state emission spectra of each nanoarray at  $\lambda_{\text{exc}} = 400 \text{ nm}$  at pH 5, 6, 7, and 8. The first narrow peak marked by an asterisk is the water Raman peak, with the relative intensity decreasing with increasing number of dye molecules. (E) pH dependent emission intensity ratio of C343 (487 nm) and FAM (520 nm) of the four different nanoarrays. The pH sensitivity between pH 6 and pH 8 is further enhanced for the **(3x4)** array compared to that of the **6 x (2x1)** array.

Subsequently, time-resolved studies were conducted for the same arrays at the same conditions as for steady-state studies (Figure 4.8 (A)-(D)). The pH independent fluorescence decay lifetime of C343 and pH dependent fluorescence lifetime decay of FAM is shown in Figure A.4. As the absorption profile of FAM changes according to pH<sup>186</sup>, the spectral overlap of the Do and Ac changes (equation 2.4), which results in a change in  $E$  that can be monitored. The C343 decay curves showed a rapid decrease in the fluorescence lifetime with rising pH, as the fluorescence emission of FAM was restored allowing for FRET process to take place more efficiently. The lifetime decay curves were analyzed using a triple-exponential fit for pH 5 and a bi-exponential fit for pH 6-8, with the last decay component set to the fluorescence decay lifetime of an unquenched C343 ( $\tau_D = 5.65 - 5.71$  ns). The extra decay component was required to analyze the fluorescence decay curves at pH 5 as a small yet not negligible contribution from an emissive species with very small lifetime in the ps range was observed, although C343 should not be deprotonated at pH 5<sup>187</sup>. This could be due to the stronger interaction between the C343 molecules and the DNA at low pH.  $E$  was obtained from the amplitude weighted average lifetimes of the donor ( $\bar{\tau}_{DA}$ ). As was shown in the intensity ratios (Figure 4.7 (E)), the **(3x4)** array showed the best sensitivity to pH changes with sensitivities comparable to small molecule pH ratiometric sensors (Figure 4.8 (E))<sup>188</sup>.



#### 4.1. FRET nanoarrays and ratiometric sensing

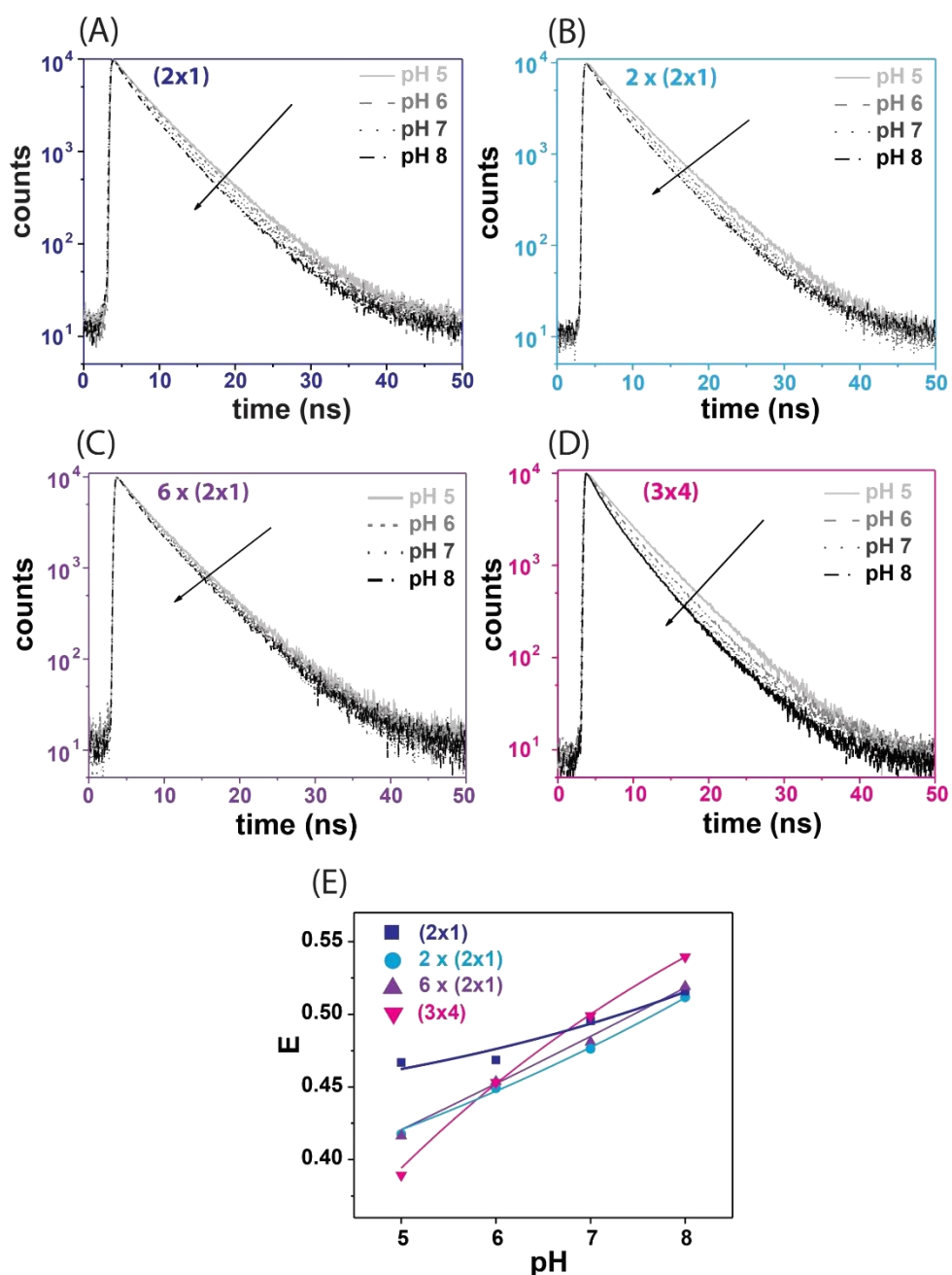


**Figure 4.8.:** Time-resolved studies of the ratiometric pH sensor. (A)-(D) The fluorescence decay curves of C343 (the Do) were recorded at 490 nm ( $\lambda_{exc} = 450$  nm) at four different pH values for the four nanoarrays. The lifetime of C343 decreased with the increase in pH, as the fluorescence of FAM (the Ac) was restored allowing for FRET process to take place. (E) FRET efficiencies were obtained from the Do fluorescence lifetimes, with the **(3x4)** array showing the best pH sensitivity compared to the other arrays.

The integrity of the DNA origami nanostructures at each pH was also confirmed *via* AFM imaging, which showed their stability at each pH (Figure 4.9).

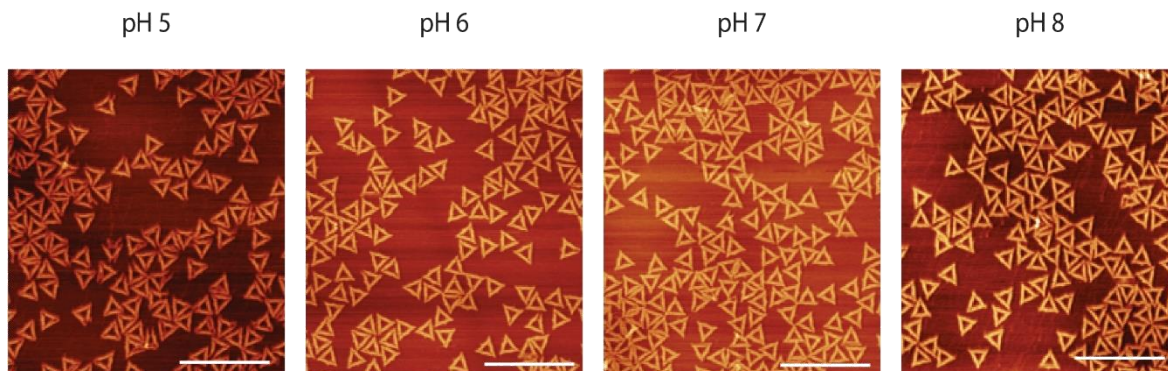


**Figure 4.9.:** AFM images of the triangular DNA origami nanostructure with **(3x4)** nanoarray at pH 5, pH 6, pH 7, and pH 8. (Scale bar = 500 nm). At all pH, triangular structures could be confirmed.

### 4.1.3. Application as ratiometric thioamide sensor

The potential to use the **(3x4)** FRET nanoarray as a thioamide ratiometric sensor was also investigated in this work. More specifically, thioacetamide (TAA) was used as the analyte. The same Do-Ac pair as for pH sensing was used as the ratiometric sensor, i.e. C343 as the TAA unresponsive internal reference, and FAM as the TAA indicator<sup>15</sup>. TAA is a hepatotoxin, leading to liver failures<sup>189</sup>. Ratiometric sensing for this analyte is different from ratiometric sensing of pH as the quenching mechanism of the acceptor is different. TAA quenches the fluorescence emission of FAM *via* photoinduced electron transfer (PET)<sup>186</sup>, a quenching mechanism which is governed by redox chemistry in very short distances (in van der Waals contact, i.e. sub-nanometer scale) between the analyte and an excited fluorophore<sup>190</sup>. The Gibbs free energy of electron transfer ( $\Delta G_{ET}$ ) from a Do to Ac is determined using the Rehm-Weller models of electron transfer as<sup>191</sup>,

$$\Delta G_{ET} = F\{E_{ox}(D) - E_{red}(A)\} - E_{0,0} + C \quad , \quad (4.1)$$

where  $F$  is the Faraday constant,  $E_{ox}(D)$  is the oxidation potential of the electron donor,  $E_{red}(A)$  is the reduction potential of the electron acceptor,  $E_{0,0}$  is the zero vibrational electronic excitation energy of the fluorophore ( $S_0 \rightarrow S_1$ ), and  $C$  is the term accounting for Coulombic interactions (negligible in water). Spontaneous quenching of the dye can be expected if the determined  $\Delta G_{ET}$  has a negative value.

#### 4.1. FRET nanoarrays and ratiometric sensing

The oxidation potential of TAA is 0.97 V vs SCE (saturated calomel electrode) and the determined  $\Delta G_{ET}$  for FAM was -0.78 eV<sup>15</sup>, predicting the dye to be quenched with the addition of TAA. For C343 in acetonitrile, the reduction potential is -1.44 V vs SCE<sup>192</sup> with  $E_{0,0} = 2.6$  eV<sup>193</sup>, leading to a  $\Delta G_{ET}$  value close to zero (-0.19 eV) predicting C343 could potentially be quenched by TAA. This is however not a precise prediction for the system studied in this thesis as the C343 used in the FRET nanoarray is linked to a DNA sequence, with measurements conducted in buffer containing salts, which could lead to a  $\Delta G_{ET}$  that could be a positive value.

Normalized emission spectra that were dilution corrected were recorded (Figure 4.10) while increasing the concentration of TAA in solution. The **(3x4)** array with only C343 (Figure 4.10 (A), (B)) showed a slight decrease in the fluorescence emission intensity. By plotting the ratio of the fluorescence emission intensity ( $I(487\text{ nm})$ ) over the initial intensity ( $I_0(478\text{ nm})$  where TAA = 0 mM), it can be seen that the intensity does not change for concentrations of TAA higher than 20 mM. Ideally, the fluorescence emission of C343 should not change with the addition of TAA. But here, a small change in the emission intensity was observed for TAA concentrations less than 20 mM. This could be due to the fact that the pH of the solution might change slightly (pH = 5.2, 100 g/L in water) resulting in a weak interaction between the DNA and the dye as was observed in the previous section at low pH. The pH of the solution, however, does not change dramatically, as the excitation and emission spectra of FAM-only arrays showed no change in their profile (Figure A.5). On the other hand, the emission intensity of the array with only FAM (Figure 4.10 (C), (D)) decreased significantly with increasing amount of TAA. When the FRET array (with both Do and Ac) was assembled, the intensity of the Ac ( $I(520\text{ nm})$ ) over the Do ( $I(487\text{ nm})$ ) followed the decreasing trend of the Ac.

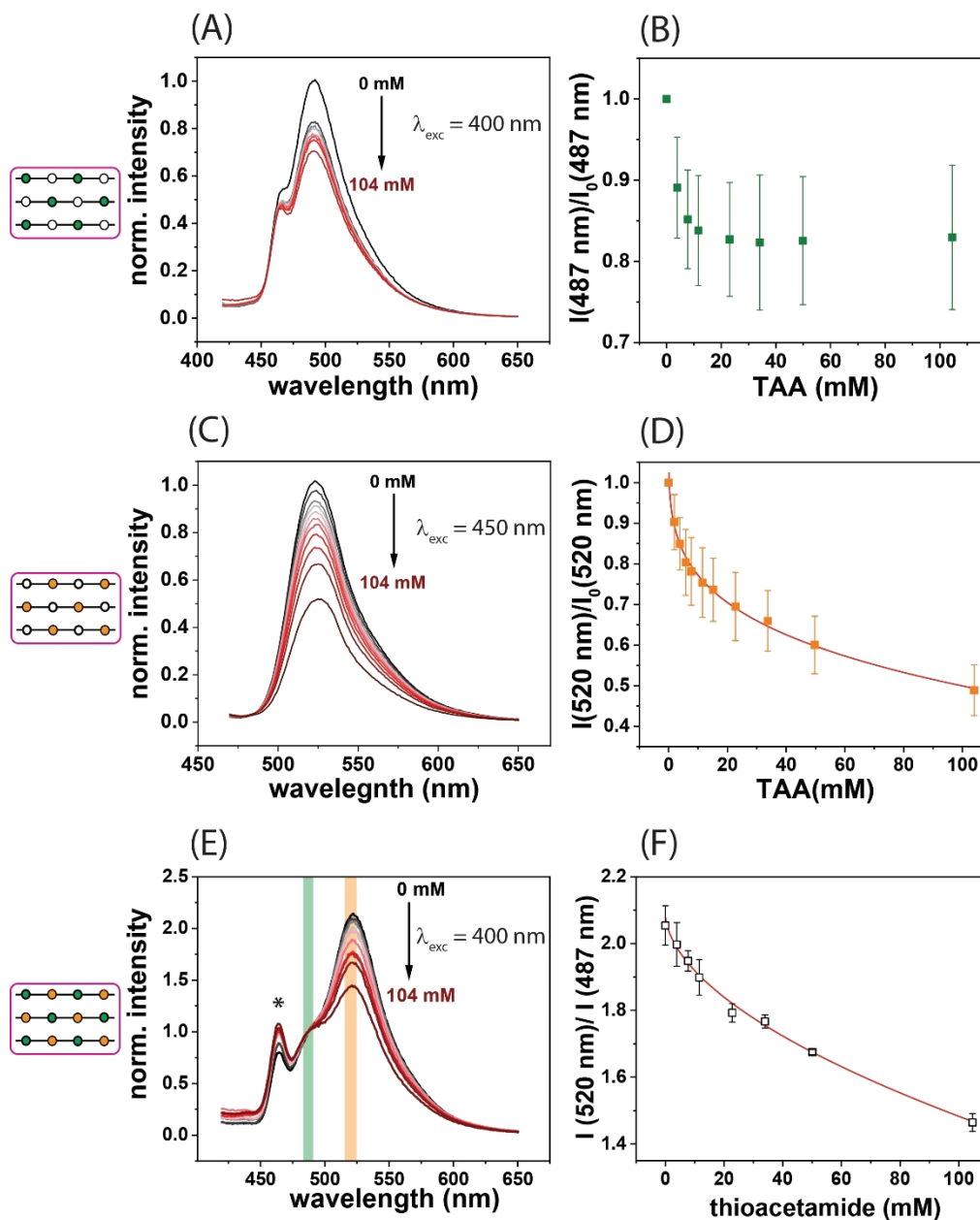


**Figure 4.10.:** Steady-state emission spectra of the (3x4) array at different TAA concentrations. (A) Normalized emission spectra of the C343-only array ( $\lambda_{exc} = 400$  nm) showed a slight decrease in the emission intensity with the addition of TAA. (B) Fluorescence intensity of C343 at 487 nm ( $I(487 \text{ nm})$ , TAA = x mM) over initial fluorescence intensity ( $I_0(487 \text{ nm})$ , TAA = 0 mM) showed a slight decreasing trend until a plateau was reached at approximately 20 mM. (C) Normalized emission spectra of the FAM-only array ( $\lambda_{exc} = 450$  nm) showed a decrease in the emission intensity with the addition of TAA. (D) Fluorescence intensity of FAM at 520 nm ( $I(520 \text{ nm})$ , TAA = x mM) over initial fluorescence intensity ( $I_0(520 \text{ nm})$ , TAA = 0 mM) decreased with the increase of the concentration of TAA. (E) Normalized emission spectra of the FRET nanoarray ( $\lambda_{exc} = 400$  nm) showed a first peak arising from C343 with a second peak arising from FAM *via* FRET (water Raman peak marked with asterisk). (F) The intensity ratio of FAM over C343 decreased with increasing TAA concentration, as FAM was quenched due to the analyte.

#### *4.1. FRET nanoarrays and ratiometric sensing*

Subsequently, time-resolved studies were conducted at the same conditions (Figure 4.11). Fluorescence lifetime decay profile of the Do did not change over the full concentration range (Figure 4.11 (A)), with the determined average lifetime of  $5.62 \pm 0.03$  ns (Figure 4.11 (B)), essentially staying constant. In contrast, the fluorescence lifetime decay of FAM decreases significantly with the increasing concentration of TAA (Figure 4.11 (C)) from  $4.79 \pm 0.04$  ns to  $3.69 \pm 0.01$  ns (Figure 4.11 (D)). As explained earlier, the absorption of FAM does not change with the addition of TAA and therefore the Do lifetime (C343) in a FRET nanoarray will not change. This was confirmed as shown in Figure 4.11 (E), (F). It is therefore clear that sensing for an analyte such as TAA, which quenches the emission of the Ac without changing the absorption profile, can be done using the ratio of the fluorescence emission intensity of the Do against the Ac (intensity based ratiometric sensing).

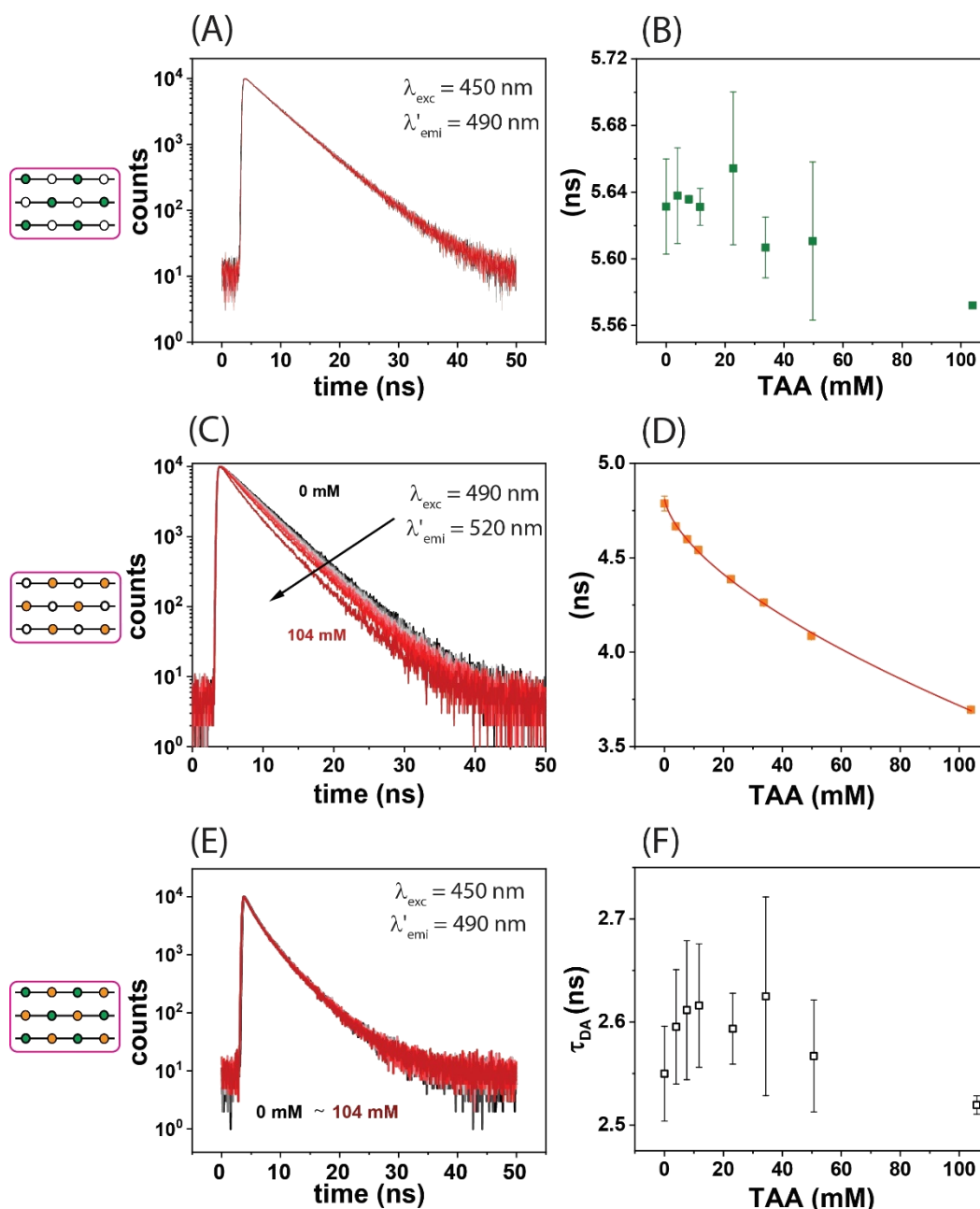


**Figure 4.11.:** Time-resolved studies of the ratiometric TAA sensor of the **(3x4)** array at different TAA concentrations. (A) The fluorescence decay curves of C343 (the Do) were recorded at 490 nm ( $\lambda_{exc} = 450$  nm), which showed very little change with the addition of TAA. (B) The determined fluorescence decay lifetimes ( $\tau_s$ ) showed an average lifetime of  $5.62 \pm 0.03$  ns. (C) The fluorescence decay curves of FAM (the Ac) were recorded at 530 nm ( $\lambda_{exc} = 490$  nm), which showed a clear change in the decay profiles. (D) The determined  $\tau_s$  decreased from  $4.79 \pm 0.04$  ns to  $3.7 \pm 0.01$  ns with the increase in TAA concentration. (E) The fluorescence decay curves of C343 were recorded for the **(3x4)** array at 490 nm ( $\lambda_{exc} = 450$  nm), with both dyes of the FRET pair C343 and FAM, which showed no change in the decay curve profiles. (F) The determined amplitude averaged donor lifetime ( $\bar{\tau}_{DA}$ ) does not change, as expected, with an average of  $2.58 \pm 0.04$  ns.

## 4.1. FRET nanoarrays and ratiometric sensing

### 4.1.4. Conclusions

Various FRET nanoarrays of different sizes and patterns of Do and Ac molecules, at a ratio of 1:1, were created using DNA origami nanostructures. Analyzing the nanoarrays with Steady-state and time-resolved fluorescence methods, optimization of the array could be done by arranging the dye molecules in a checkerboard pattern as well as increasing the array size to a **(3x4)** array. Emission intensity ratio of the Do and Ac as well as  $E$  were enhanced. This arrangement also allows for minimum self-quenching of the dyes.

The versatility of the nanoarray was shown by simply replacing the dye-labeled ssDNA strands with the appropriate dye molecules for the application. Based on their improved optical properties, **(3x4)** nanoarrays were further used in a proof-of-concept study as a ratiometric pH sensor. Here, a pH independent donor C343 and a pH responsive acceptor FAM were used. The enhanced sensitivity of the **(3x4)** nanoarray compared to single dye pairs or separated dye pairs to pH showed the potential of this approach for pH sensing. This nanoarray was further utilized as a ratiometric sensor a toxin, TAA, where C343 is analyte independent and FAM is analyte responsive. This analyte, in contrast to sensing pH, is better suited for intensity based ratiometric sensing as  $E$  does not change according to the TAA concentration. Alternatively, the FAM-only array could be utilized as bright TAA sensor when using time-resolved fluorescence techniques, such as fluorescence lifetime imaging (FLIM)<sup>194</sup>, as lifetime-based detection schemes eliminate the problems faced by single wavelength emission based detection schemes (explained in section 2.2.3). The applicability of the nanoarrays as ratiometric sensors can be easily expanded to sensing other analytes by choosing the appropriate FRET pairs, such as a. Hg<sup>+</sup> sensor using rhodamine-BODIPY pair<sup>195</sup> or a H<sub>2</sub>O<sub>2</sub> sensor using coumarin-fluorescein derivatives<sup>18</sup>.

## 4.2. A new reporter design for microbead-based assay

In this section, utilizing the DNA origami technology to develop a new fluorescent reporter for microbead-based assays for detecting oligonucleotides is discussed. Compared to the previous section where ratios of two emission wavelengths of two dye molecules were used to determine the analyte concentration, here single fluorescence emission wavelength was used. However, this emission intensity is referenced back to the emission of the microbead code and therefore could also be thought as an internally referenced ratiometric sensing technique. Figure 4.12 illustrates this microbead-based sensing technique, as was explained in section 3.2.2, where the microbead-bound reporter fluorescence is measured using the VideoScan technology. The target sequence used here are DNA equivalents of human miRNA sequences (~20 nb in length, currently used as biomarkers <sup>196</sup>) and all included a 40nb poly adenosine end (A<sub>40</sub>), which acted as the handle for the dye-labeled reporters. This poly A extension miRNA is actually used quite commonly in microRNA (miRNA) detection to compensate for their short sequence length <sup>197</sup>.

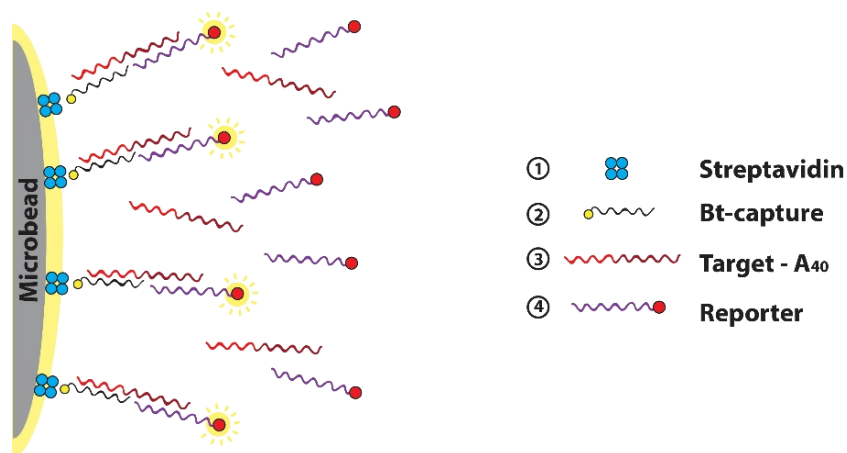


**Figure 4.12.:** Microbead-based oligonucleotide sensing using VideoScan. Target selectivity is achieved by the biotinylated capture ssDNA (Bt-Capture) on the surface of the streptavidin coated microbead. The reporter signal is only measured if they are hybridized to the surface bound target oligonucleotide.



## 4.2. A new reporter design for microbead-based assay

### 4.2.1. Comparison of the two reporters

As was explained in section 3.2.2, size- and color-coded microbeads were used to detect target oligonucleotides. The target response of the two different reporters, ssDNA labeled with one dye molecule (*ssDNA\_R*) and the DNA origami nanostructure reporter with 14 dye molecules (*DNA origami\_R*), were compared (Figure 4.13). For both reporters, the surface fluorescence intensity increased until reaching a maximum at 10 nM target concentration (Figure 4.13 (A)). Several key assay performance characteristics were quantified (Figure 4.13 (B)) such as limit of detection (LoD), limit of quantification (LoQ) and half maximal effective concentration (EC50). The assay parameters are given as <sup>198</sup>,

$$\text{LoD} = \frac{3.29 \times \sigma_0 + B}{A}, \quad (4.2)$$

$$\text{LoQ} = \frac{10 \times \sigma_0 + B}{A}, \quad (4.3)$$

$$\text{EC50} = \frac{(y_{\max} + y_{\min})/2 + B}{A}, \quad (4.4)$$

where  $\sigma_0$  is the standard deviation of the blank,  $A$  is the slope, and  $B$  the intercept of the calibration curve. As shown in Figure 4.13 (B) the *DNA origami\_R* reporter showed a lower LoD (78 pM), as well as a lower LoQ (366 pM) than *ssDNA\_R* (LoD: 549 pM, LoQ: 655 pM) for

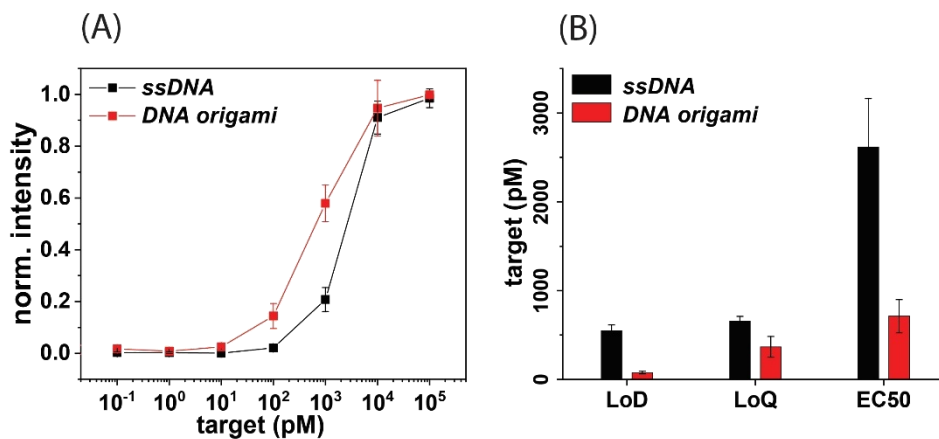


**Figure 4.13.:** Comparison of the two different reporters *ssDNA\_R* (black) and *DNA origami\_R* (red). (A) Normalized surface fluorescence intensities were recorded using VideoScan according to the target oligonucleotide concentration with each reporter at 2.5 nM. (B) Assay parameters such as LoD, LoQ, and EC50 were quantified using equations 4.2 - 4.4 from four individual dilution series for each reporter. LoD and LoQ were clearly shifted towards lower target concentration by using *DNA origami\_R*.

the assay, resulting in a more sensitive assay for the detection of target oligonucleotides at lower concentrations than when using *ssDNA\_R* as the reporter. The dynamic range was larger for *DNA origami\_R* (0.1 – 10 nM) than for *ssDNA\_R* (1 – 10 nM).

#### 4.2.2. Proof-of-concept multiplex analysis

Using microbeads encoded with different ratios of fluorescent dyes allows for each analyte to be assigned to a specific microbead population, which allows for multiplex analysis. As the target selectivity for this assay was achieved through the Bt-capture strand (Figure 4.12), the exact same reporters could be used for all target sequences (all target sequences have an A<sub>40</sub> sequence at the 3'- end). Here, five different target oligonucleotides (exact sequences are listed in Table A.3) were chosen for multiplex analysis (Figure 4.14) with both *ssDNA\_R* and *DNA origami\_R*.

Once all the microbead populations were functionalized, they were mixed in one microwell for VideoScan measurements. For all five target sequences (Figure 4.14 (A)-(E)), the assay showed similar trends, with the *DNA origami\_R* reaching maximum intensity at a lower target concentration than the *ssDNA\_R*. The determined assay parameters are shown in Figure 4.14 (F), with the assay showing lower values for all parameters when using *DNA origami\_R* (LoD: 2.7 – 9.5 pM, LoQ: 5.3 – 15.5 pM, EC50: 46 – 94 pM) compared to that of using *ssDNA\_R* (LoD: 80 – 185 pM, LoQ: 81 – 186 pM, EC50: 403 – 713 pM). It must be noted here that this is a proof-of-concept multiplex analysis, as the microbeads were mixed after already hybridizing with target and the reporter. In fact, no fluorescence signal was observed if the microbeads were incubated to more than one target sequence. This indicates the complexity of the DNA hybridization process that occurs on the surface of the microbead, where many competing factors exist.

## 4.2. A new reporter design for microbead-based assay

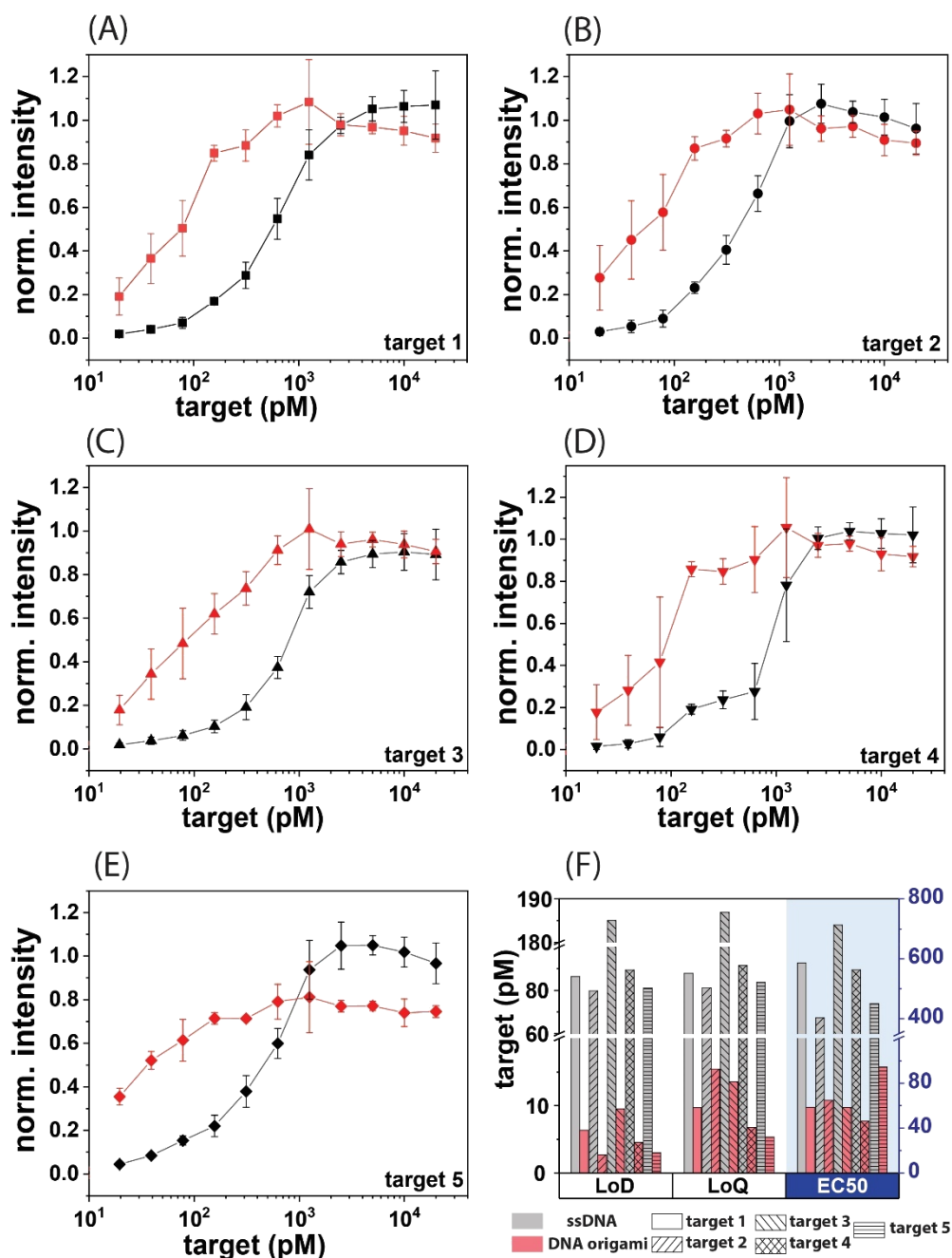


**Figure 4.14.:** Multiplex analysis. (A)-(E) Normalized surface fluorescence intensity recorded for five different target sequences for both reporters (*ssDNA\_R*: black, *DNA origami\_R*: red). (F) Assay parameters (LoD, LoQ, and EC50) were determined according to equation 4.2 - 4.4. Again, a clear distinction between the two reporters was shown with *DNA origami\_R* showing significantly lower values for all three parameters (EC50 values shown on right axis in blue, with the same unit as left axis).

### 4.2.3. Strategies to improve the measured signal

It has been shown in previous sections that by using *DNA origami\_R*, the microbead-based assay could be optimized for the detection of target oligonucleotides at lower concentration. This is advantageous for detecting targets such as miRNA that exist in low copy numbers. However, the fluorescence intensity measured when using these *DNA origami\_R* was considerably lower than when using *ssDNA\_R* (Figure A.6). This could be due to the size of the DNA origami nanostructure being simply much larger than the *ssDNA*, blocking still available target sites for binding more reporters. Another factor, as briefly mentioned at the end of section 4.2.2, could be that the DNA hybridization on the surface of the microbead is much more complicated than expected, resulting in a much less efficient labeling yield.

Here, the effect of altering the binding strength between the *DNA origami\_R* and the target (that is already bound on the microbead surface) on the measured signal is shown (Figure 4.15). The hybridization conditions were varied by changing the temperature and magnesium ion concentration (Figure 4.15 (B)) for DNA origami nanostructures with 4 and 8 probe strands. A clear decrease in the fluorescence intensity was observed as the hybridization temperature was raised from room temperature (RT) to 45 °C. In addition, with the increase in the magnesium ion concentration (10 – 25 mM) a slight increase in the fluorescence intensity was observed. This increase in the ionic strength in the hybridization solution provides more screening of the electrostatic repulsion between the negatively charged backbone of the DNA, therefore increasing the melting temperature<sup>199,200</sup>. In addition, a slight increase in the signal was observed when using *DNA origami\_R* with 8 probe strands compared to that with 4 probe strands. Based on this, it was hypothesized that increasing the number of probe strands would also enhance the binding strength and thus the surface fluorescence. A target concentration dependent graph was therefore obtained comparing *DNA origami\_R* with 4 probe strands to that with 12 probe strands at two different magnesium concentrations (15 mM and 25 mM). The difference in the observed signal however was not dependent on the number of probe strands but on the magnesium concentration, which suggests that the signal intensity is affected more by the salt concentration and hybridization temperature rather than the number of sites that the target can bind to.

## 4.2. A new reporter design for microbead-based assay

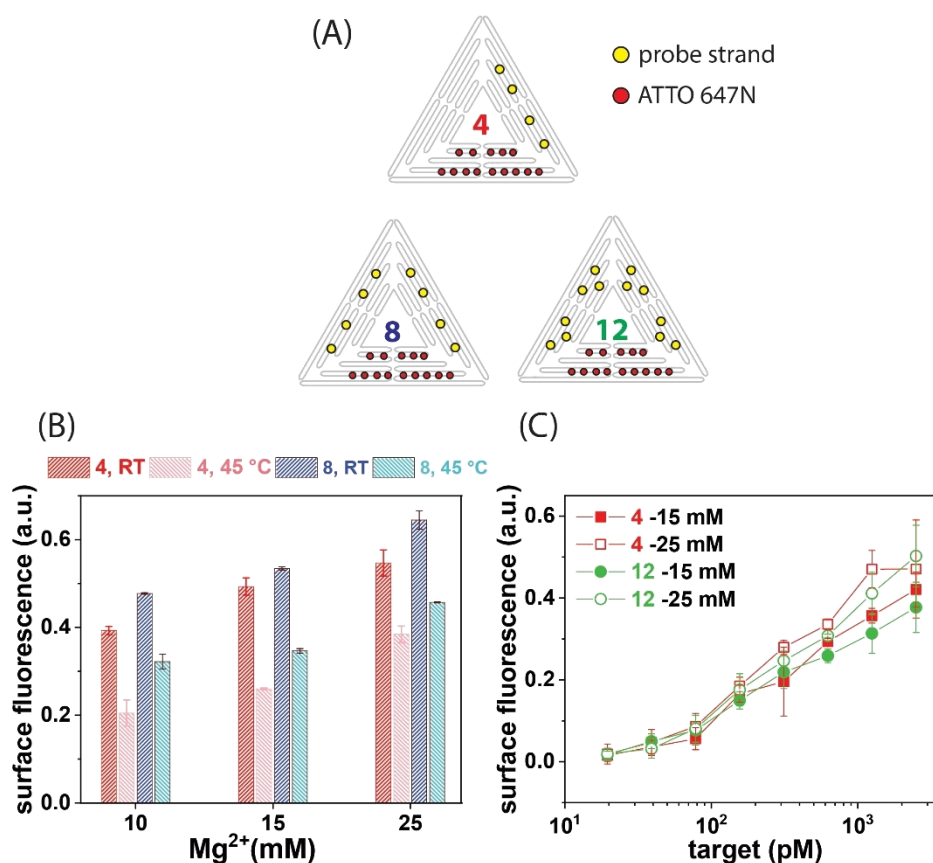


**Figure 4.15.:** Improving the signal intensity. (A) *DNA origami\_R* structures with 4 (red), 8 (blue), and 12 (green) probe strands for target oligonucleotide binding (red circles represent ATTO 647N). (B) Surface fluorescence measured for *DNA origami\_R* with 4 probe strands at room temperature (red) and at an elevated temperature of 45 °C (pink), and with 8 probe strands at room temperature (blue) and at 45 °C (light blue) at three different magnesium concentrations (100 nM target oligonucleotide, 2.5 nM reporter). (C) Surface fluorescence measured according to the target oligonucleotide concentration for *DNA origami\_R* with 4 and 12 probe strands, each at 15 mM and 25 mM magnesium concentration.

As the strategies to improve the signal shown in Figure 4.15 were not satisfactory, further efforts were made to investigate whether the binding strength of the reporters to the target could be enhanced by placing the probe strands in different positions (seven different *DNA origami\_R* structures, Table A.4). The effect of the number of probe strands, as well as the spatial distribution of them (either all on one trapezoid of the triangle or two) was varied. The resulting fluorescence signals further confirmed that the binding strength was not significantly altered by the number of probe strands per *DNA origami\_R* (Figure 4.16). Unfortunately, no trend could be observed either (Figure 4.16 (B)), highlighting the complexity of the hybridization process at the microbead surface.

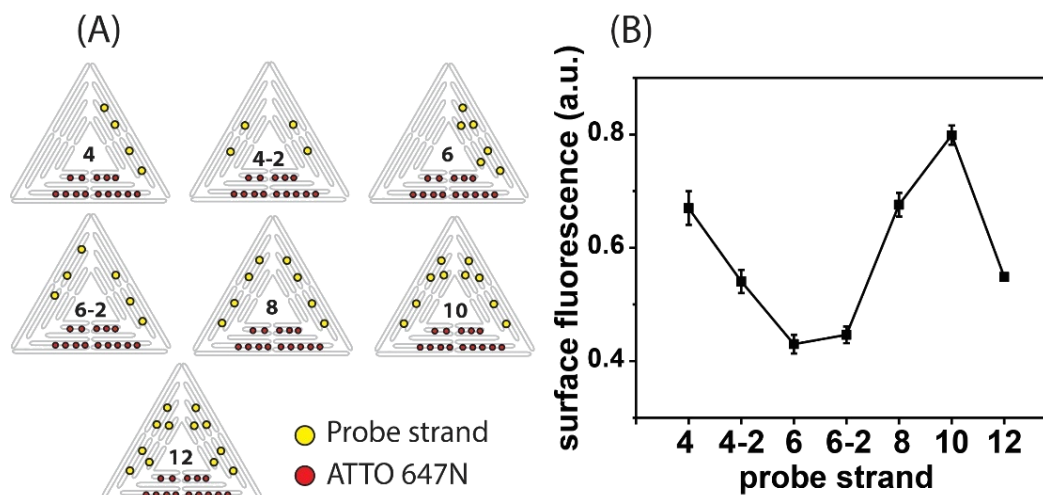


**Figure 4.16.:** Probe strand influence on signal. (A) Seven different *DNA origami\_R* structures were built, with the number of probe strands ranging from 4 to 12, with altering the placements of the probe strands on the DNA origami nanostructure. (B) Surface fluorescence signal measured for each *DNA origami\_R* (100 nM target, 2.5 nM reporter).

Another strategy to improve the fluorescence signal is to simply add on many DNA origami nanostructures to amplify the number of ATTO 647N that would be bound on the surface. Here, a linker DNA origami (*Linker origami*) with a linker DNA strand (*Linker*) was chosen to connect multiple DNA origami nanostructures (Figure 4.17, sequences are listed in Table A.5). Once the *DNA origami\_R* was immobilized on the surface of the microbead, the *Linker* was hybridized with the linker capture strand (linker capture 1). In the subsequent hybridization step, the *Linker origami* was added, allowing for the linker capture strand (linker capture 2) to hybridize with the *Linker*. This process could be, in theory, repeated multiple times to amplify the signal as required. However, as shown in Figure 4.17 (A) and (B) (4 probes and 8 probes, respectively), signal amplification was not achieved using this strategy. This, as was postulated earlier, shows that the DNA hybridization process on the surface of the microbead is very complicated. Although the *Linker* sequence is completely different from the target sequence, by the addition of this strand (+ 50 nM *Linker*) the fluorescence signal decreased significantly. With the addition of the *Linker origami*, the fluorescence signal was fully restored.

## 4.2. A new reporter design for microbead-based assay

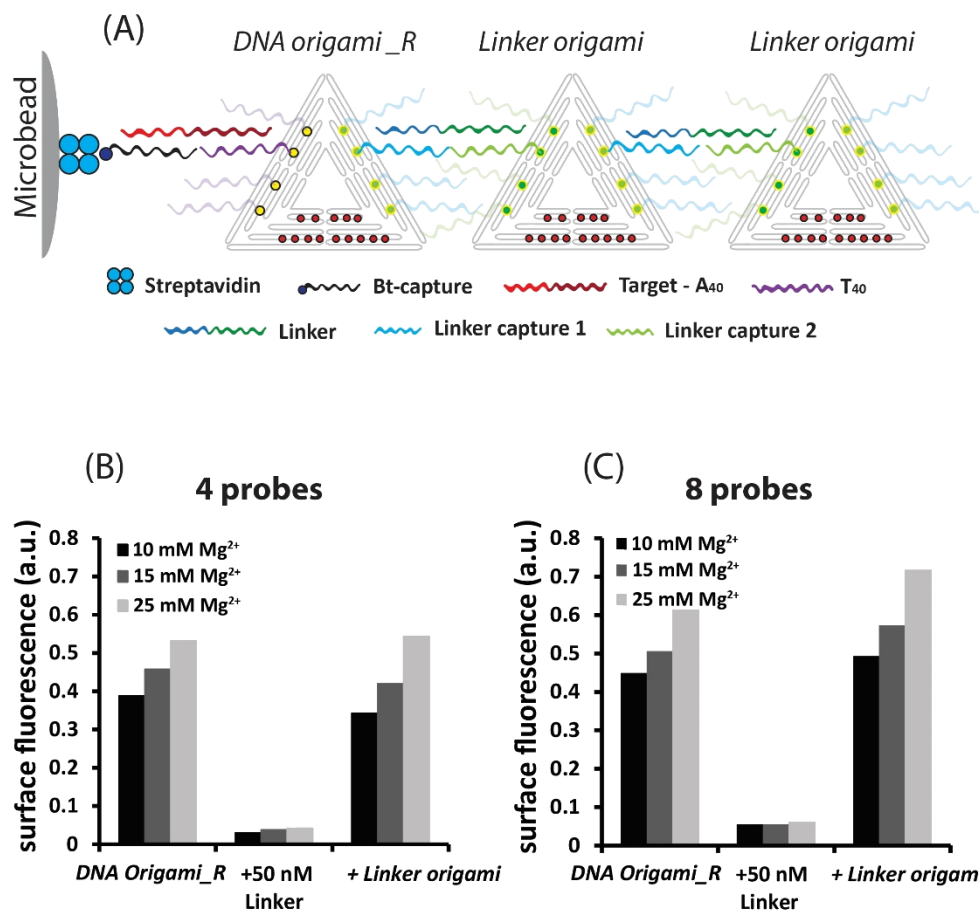


**Figure 4.17.:** Signal amplifying strategies by linking DNA origami nanostructures. (A) Schematic illustration of the hybridization steps, connecting the multiple DNA origami nanostructures. In addition to the fluorescence signal generated by DNA origami\_R, Linker origami that also has 14 dye molecules could provide an amplification of the fluorescence signal. The DNA origami nanostructures are linked via a linking DNA (Linker) that has a different sequence than the target. (B)-(C) Surface fluorescence measured using either a DNA origami\_R with 4 probes (B) or 8 probes (C). Instead of the fluorescence signal enhancing, with the addition of the Linker the signal was significantly decreased. By hybridization of the Linker origami, the fluorescence is restored.

#### 4.2.4. Conclusion

DNA origami nanostructures were utilized in this section, to develop a reporter system for microbead-based assays for detecting oligonucleotides. Utilizing the spatial addressability of the DNA origami nanostructures, 14 ATTO 647N dye molecules as well as a number of probe strands ranging from four to twelve were placed on each reporter. VideoScan technology was used to measure the fluorescence signals of the assay. *DNA origami\_R* were shown to be more suitable than *ssDNA\_R* for target concentrations in the lower region. Proof-of-concept multiplex analysis was also conducted by assigning each target sequence to a specific microbead population. Several signal-amplifying strategies, including the increase of ionic strength in the hybridization solution as well as the number of probe strands to increase the binding strength, however showed little improvement in the measured fluorescence signal indicating complex hybridization behavior of DNA on the surface of microbeads. Although the DNA origami nanostructure based reporters showed great potential as a new reporter for oligonucleotide sensing, many questions still need to be answered especially in regards to gaining more insight into how the *DNA origami\_R* is bound to the microbead surface. This could lead to improving the system to allow for real multiplex analysis, increasing the fluorescence signal by increasing the surface coverage, and utilizing an appropriate signal amplification strategy where the linker does not reduce the initial emission intensity.



## 4.3. DNA coated metal nanoparticles with tailored optical properties

In this last section, different types of metal nanoparticles (AuNPs, AgNPs, and AuNRs) were assembled on DNA origami nanostructures. As explained in section 2.4.4, the near-field of two nanoparticles in close proximity can interact with each other, leading to an enhanced electric field (hot-spot) within the gap of the two particles (Figure A.7), which can modify the optical properties of the analyte placed in this hot-spot. Therefore, assembling dimer structures and placing the analyte of interest in the gap is of great interest. The spatial addressability of DNA origami nanostructures was once again utilized here as the platform to place nanoparticles and dye molecules in desired arrangements. Preparation of the samples were not an easy task, especially when using dye-labeled ssDNA, and thus in this section successes and challenges in assembling various nanoparticles are discussed. Figure 4.18 summarizes the structures that were successfully assembled in this work.

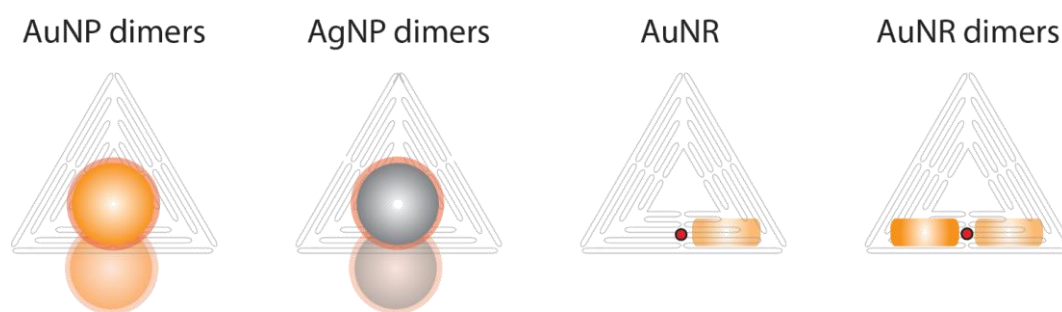


**Figure 4.18.:** A summary of structures assembled in this section. AuNPs and AgNPs coated with dye-labeled DNA were assembled as dimers on DNA origami nanostructures. AuNRs were also coated with DNA and placed on DNA origami nanostructures, either as a monomer or a dimer. TAMRA (red circle) was additionally placed on the DNA origami nanostructure.

### 4.3.1. AuNP and AgNP dimers on DNA origami nanostructure

Citrate stabilized AuNPs and AgNPs were coated with dye-labeled DNA and assembled as dimers on DNA origami nanostructures. Although many studies exist where the particles are

### 4.3. DNA coated metal-nanoparticles with tailored optical properties

coated with thiol modified DNA (protocols followed in section 3.2.4), problems still exist when particles need to be coated with a DNA sequence that includes a charged dye molecule, or the particle is large (over 60 nm). Here, AuNPs were coated with the dye-labeled DNA without aggregation<sup>154</sup>, and in less than 24 hours (following former coating methods done at RT required more than 48 hours for particles larger than 20 nm). Coating AgNPs with dye-labeled DNA was challenging as expected, but progress has been made here to achieve stable DNA coated particles.

#### AuNP dimers

AuNPs of different sizes (40, 60, and 80 nm) were coated with SH-T<sub>4</sub>(TTT)<sub>8</sub> strands and assembled onto the DNA origami nanostructure (capture strands are listed in Table A.6). The hybridization of the coating strand with the capture strand on the DNA origami occurs in a zipper configuration<sup>201</sup>, as the staple strand was extended on its 5'-end with the

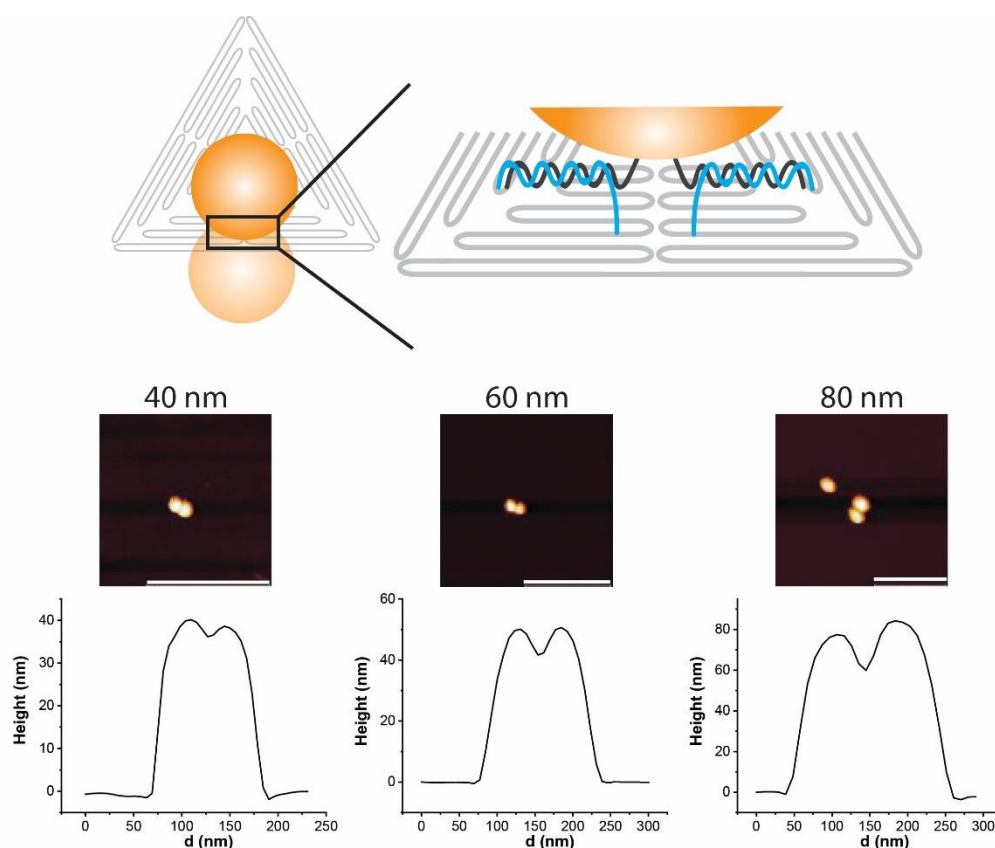


**Figure 4.19.:** AuNP dimers assembled on DNA origami nanostructures. Upper panel shows a schematic representation of the AuNP dimer structure on the DNA origami nanostructure, with a zoom-in area (black box). The hybridization of the AuNP coating strand and the capture strand is in a zipper configuration. Bottom panels show AFM images of an example of a dimer structure for each size of the AuNPs (scale bar 500 nm) with the height profile of each structure.

complementary sequence (Figure 4.19, upper panel). This allows for the particles to assemble closer to each other thus making the gap size between the particles smaller. The gap size is expected to be 7 nm (estimated from 2.0 nm thick DNA origami nanostructure and 2.5 nm thick DNA coating per AuNP<sup>57</sup>). As shown in Figure 4.19 bottom panels, AuNP dimer structures for all sizes could be assembled that could be clearly imaged by AFM.

These dimer structures provide a good platform to calculate SERS enhancement factors, and therefore 60 nm AuNPs were coated with a dye labeled DNA in which the dye molecule was used as the SERS analyte. The dye was placed close to the surface of the AuNP (SH-dT(X)T<sub>3</sub>(TTT)<sub>8</sub>, X = dye molecule), which ensures the fluorescence of the dye molecule to be quenched, which otherwise would create a large background in the measured SERS spectra.

The SERS enhancement factor can be determined as<sup>202</sup>,

$$EF_{SERS} = \frac{I_{SERS}/N_{SERS}}{I_{NR}/N_{NR}}, \quad (4.5)$$

where  $I_{SERS}$  and  $I_{NR}$  are the SERS and normal Raman intensities measured in the presence and absence of the SERS substrate, respectively.  $N_{SERS}$  and  $N_{NR}$  are the analyte molecules that actually emit SERS and normal Raman signals, respectively. For dimer structures the enhancement factor ( $EF_{dimer}$ ) can also be determined using a reference enhancement factor as,

$$EF_{dimer} = \frac{I_{dimer}/N_{dimer}}{I_{monomer}/N_{monomer}} EF_{monomer}, \quad (4.6)$$

where  $I_{dimer}$  and  $I_{monomer}$  are the SERS intensities measured for the single nanoparticle and dimer, respectively.  $N_{dimer}$  and  $N_{monomer}$  are the number of analyte molecules for the dimer structure and the monomer, respectively. Here, the reference enhancement factor is given as  $EF_{monomer}$ , which is the enhancement factor for a single particle.

Here, two dye molecules were chosen as the SERS analyte; TAMRA which is resonant to the 532 nm laser thus enabling surface enhanced resonance Raman scattering to occur (with a large characteristic SERS peak at 1650 cm<sup>-1</sup><sup>27</sup>), and PEPY which is non-resonant to the 532 nm laser (with the characteristic C≡C stretching vibration occurring at 2200 cm<sup>-1</sup>, a spectral region where DNA does not show any Raman scattering<sup>203,204</sup>). The advantage of using TAMRA, as mentioned, is the resonance to the excitation laser allowing for an extra enhancement.

### 4.3. DNA coated metal-nanoparticles with tailored optical properties

However, due to this resonance the fluorescence emission of TAMRA prevents one from collecting normal Raman scattering and thus requires one to rely on a reference system (equation 4.6,  $EF_{monomer}$ ) of a 60 nm AuNP<sup>27</sup>. PEPY on the other hand is not resonant to the 532 nm excitation laser (absorption occurs only in the Blue/UV regime), and therefore collecting normal Raman scattering can be done without difficulties, and can be used to determine directly the SERS enhancement factors (equation 4.5) without having to rely on a reference system. However, since PEPY does not absorb at 532 nm, the extra enhancement due to the resonance will not be observed, and the cross section of the Raman scattering could be much smaller.

Figure 4.20 (A) shows the absorption spectra of the two dye labeled ssDNAs showing clearly that only TAMRA absorbed at 532 nm (dotted line). Using sequences SH-dT(TAMRA)T<sub>3</sub>(TTT)<sub>8</sub> and SH-dT(PEPY)T<sub>3</sub>(TTT)<sub>8</sub>, where the first T base next to the thiol group is modified with the dye molecule, 60 nm AuNPs were coated and subsequently hybridized on to the capture strands protruding from the DNA origami nanostructures to assemble dimers (Figure 4.20 (B)).

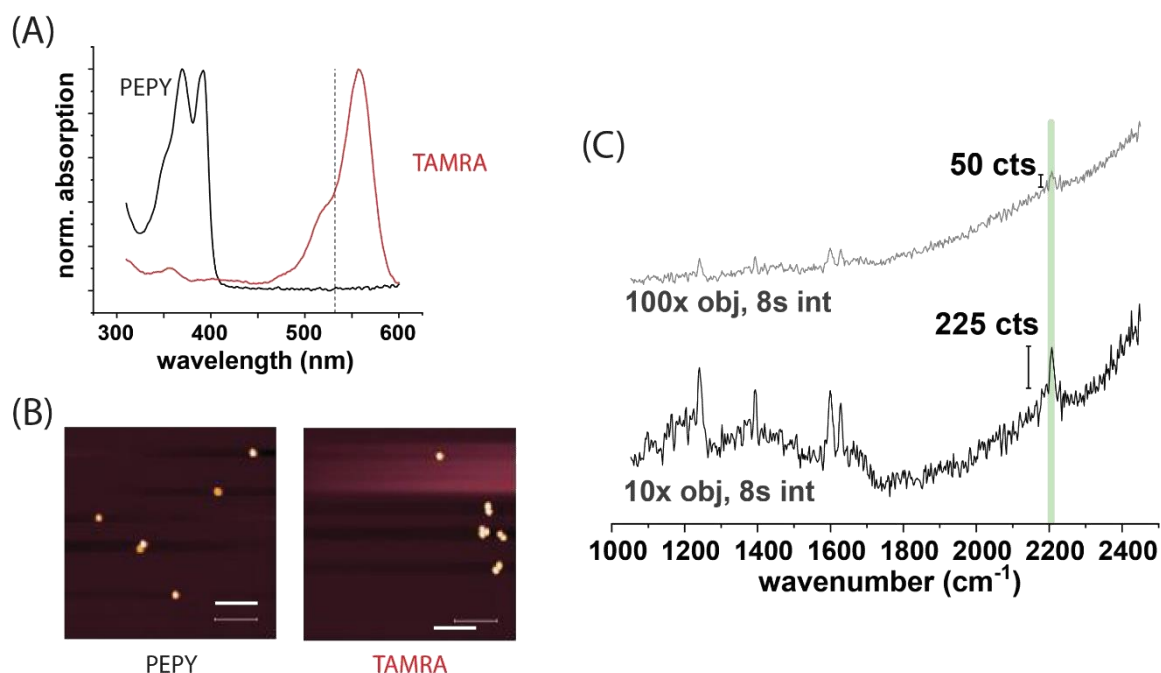


**Figure 4.20.:** PEPY and TAMRA. (A) Normalized absorption spectra of the two dye-labeled DNA strands clearly showing the absorption of the TAMRA dye to the 532 nm laser (dotted line) whereas the PEPY dye absorbs below 400 nm. (B) AFM images of the AuNP dimer structures that are coated with the dye-labeled DNA (on Si chip). (C) Normal Raman scattering spectra ( $\lambda_{exc} = 532$  nm) of the PEPY-labeled DNA, showing a clear characteristic peak at 2200 cm<sup>-1</sup> (highlighted in green).

The normal Raman scattering spectra ( $\lambda_{\text{exc}} = 532 \text{ nm}$ ) were collected for the PEPY-labeled DNA on Si chips and the characteristic peak at  $2200 \text{ cm}^{-1}$  could be clearly observed (Figure 4.20 (C)).

SERS spectra were recorded ( $\lambda_{\text{exc}} = 532 \text{ nm}$ ) by mapping the area near the end of a scratch on the Si chip surface and could be correlated with each structure imaged *via* AFM (Figure 4.21 (A)). As is shown in Figure 4.21 (B), the characteristic TAMRA Raman scattering peak at  $1650 \text{ cm}^{-1}$  could be clearly identified. The difference between the dimer structure (71 cts,  $n = 1$ ) and the monomer (21 cts,  $n = 9$ ) structure could also be clearly seen.

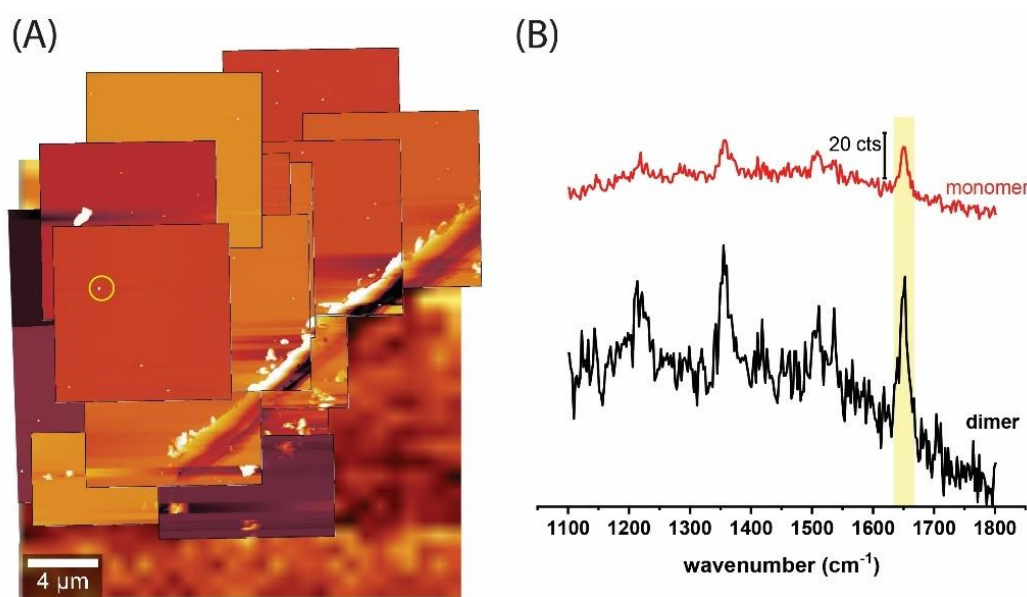


**Figure 4.21.:** SERS of TAMRA for AuNP dimers. (A) AFM image overlaid on the Raman map, using the scratch on the surface as the guide. The AuNP dimer was seen in the yellow circle. (B) SERS spectra arising from monomers (red, averaged from 9 monomers, 21 cts) and the dimer (black, 71 cts) highlighted in (A). Characteristic peak of TAMRA at  $1650 \text{ cm}^{-1}$  is highlighted in yellow. SERS spectra were all obtained at  $\lambda_{\text{exc}} = 532 \text{ nm}$ , using a 100 x objective, a laser power of  $25 \mu\text{W}$ , and integration time of 4s.

By using the literature value of enhancement factor for a 60 nm AuNP ( $9 \times 10^5$ )<sup>205</sup>, and the number of TAMRA ( $N_{\text{TAMRA}}$ ) modified DNA sequences on the 60 nm AuNP<sup>27</sup>, an  $EF_{\text{dimer}}$  of  $1.52 \times 10^6$  could be estimated for the AuNP dimers (Table 4.1).

### 4.3. DNA coated metal-nanoparticles with tailored optical properties

**Table 4.1.:** Estimations of  $EF_{dimer}$  using experimentally obtained SERS data.

System (TAMRA)	1650 $cm^{-1}$ (cts)	$N_{TAMRA}$	1650 $cm^{-1}$ (cts) per TAMRA	EF
60 nm AuNP (reference)	21	5000 <sup>27</sup>	$4.2 \times 10^{-3}$	$9 \times 10^5$ <sup>205</sup>
60 nm AuNP dimer	71	10000	$7.1 \times 10^{-3}$	$1.52 \times 10^6$

As mentioned, this method of determining the  $EF_{dimer}$  relies on using EF for a AuNP monomer, which in this case was 60 nm AuNPs excited at 647 nm, a wavelength that does not match the excitation wavelength used here. As the EF is directly dependent on the excitation wavelength (equation 2.21), this could lead to a deviation from the real EF value. Determining the number of TAMRA molecules that is just in the hot-spot is also difficult, and thus an averaged EF (EF of the hot-spot as well as areas not within the hot-spot) is calculated here by taking into account all the TAMRA on the surface of the AuNP. Due to such estimations, the value presented in Table 4.1 can be used as a first insight into the determination of the  $EF_{dimer}$ .

The second SERS analyte PEPY, used to determine the  $EF_{SERS}$  directly, did not show any characteristic peaks at 2200  $cm^{-1}$  (Figure A.8), which could mean that the  $EF_{SERS}$  here is not high enough to observe molecules that have a rather small Raman cross section. This highlights the importance of using an analyte resonant to the excitation wavelength, as well as optimizing the structure and improving the sensitivity by using different excitation wavelengths for higher EF.

### AgNP dimers

As silver shows higher SERS enhancement than gold<sup>206</sup> (due to the damping effect at the LSPR being less than for gold<sup>28</sup>) at wavelengths shorter than 532 nm (Figure A.7,  $\lambda_{exc} = 488$  nm), AgNPs with a diameter of 60 nm were also used here as SERS probes and assembled into dimers on the DNA origami nanostructure (Figure 4.22). Coating AgNPs with the dye-labeled DNA proved to be much more challenging than for AuNPs, but stable particles could be obtained at high salt concentrations (0.75 M NaCl) by coating the AgNPs with a mixture of a non-labeled thiol-modified DNA and the TAMRA-labeled DNA at a 1:1 ratio. In addition, the DNA strands tended to detach from the surface much quicker than anticipated. This results in free DNA origami nanostructures as shown in Figure 4.22 (B), as the detached ssDNA occupied

the capture strands on the DNA origami nanostructure and preventing the particles to assemble on the DNA origami. Coating the AgNPs with PEPY-labeled DNA was successful, and did not require a mixture of the non-labeled thiol-modified DNA (Figure 4.22 (C)).

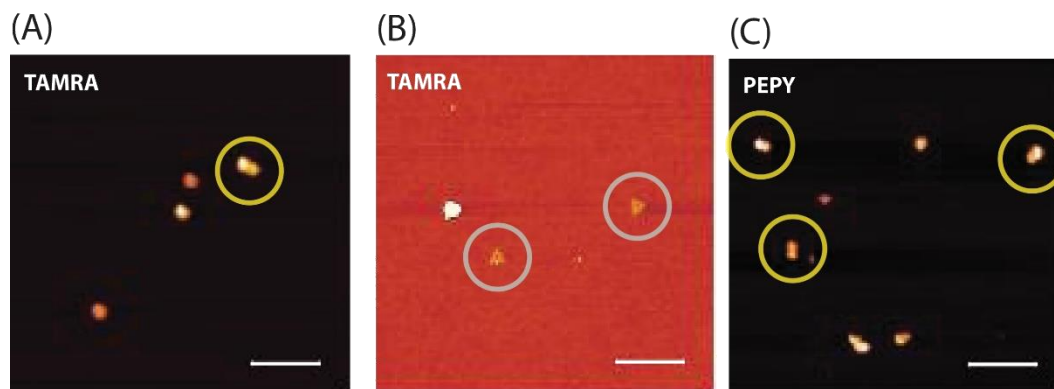


**Figure 4.22.:** AFM images of the AgNP dimers on DNA origami nanostructures (shown inside yellow circles). (A) AgNP dimers assembled on DNA origami nanostructures, coated using a 1:1 ratio of the TAMRA-labeled DNA and non-labeled DNA. (B) The same sample from (A) also had free DNA origami nanostructures (in grey circles), confirming the quick dissociation of the DNA strands from the surface of the AgNPs. (C) AgNP dimers that were coated with the PEPY-labeled DNA. Free DNA origami were not observed for these structures.

For TAMRA, SERS spectra could be obtained with the characteristic TAMRA signal observed at  $1650\text{ cm}^{-1}$  (Figure 4.23). The obtained SERS intensity of TAMRA on a AgNP monomer was very similar (22 cts,  $n=20$ ) to that of the AuNP monomer. The number of TAMRA-labeled DNA per AgNP is expected to be lower than that of the AuNP as the coating was done with a mixture of TAMRA-labeled and non-labeled DNA. Therefore, it could be postulated here that AgNPs as a SERS substrate has higher enhancement factors than AuNPs even when excited at 532 nm for the monomer. A trimer-like structure could also be observed and therefore a SERS spectrum for this was collected (Figure 4.23 (B), blue spectrum). It showed higher intensities than for the monomer but the counts were not as high as observed for the AuNP dimers, suggesting that these structures were not formed by assembly on the DNA origami but by salt-induced aggregation leading to a larger gap between the particles. This aggregation of particles happened as the structures were immobilized on the Si surface using high concentration of  $\text{Mg}^{2+}$  (50 mM), which is unavoidable as it is required to force the DNA origami structures to attach to the Si surface.

### 4.3. DNA coated metal-nanoparticles with tailored optical properties

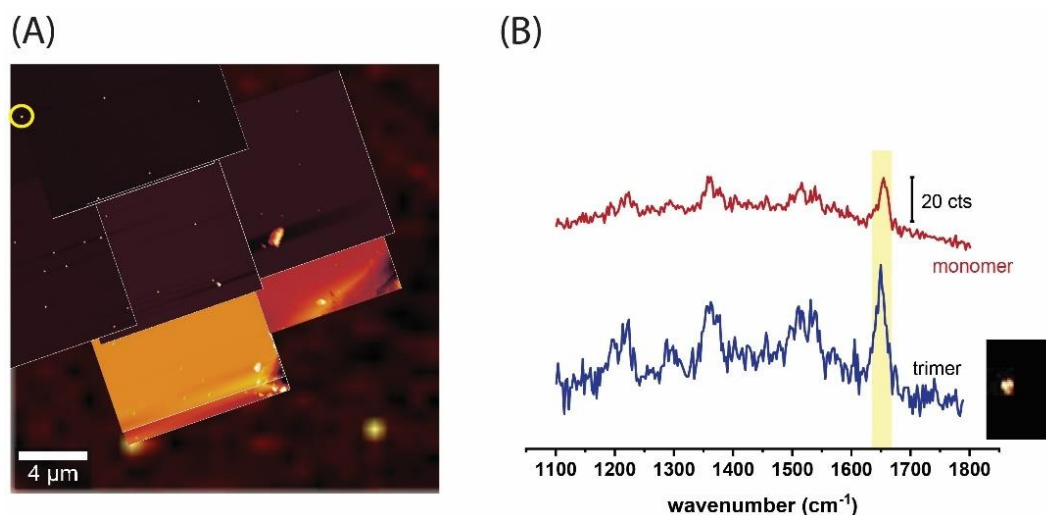


**Figure 4.23.:** SERS of TAMRA for AgNP dimers. (A) AFM image overlaid on the Raman map, using the scratch on the surface as the guide. The AgNP trimer was seen in the yellow circle. (B) SERS spectra arising from monomers (dark red, averaged from 20 monomers, 22 cts) and the trimer (navy, 57 cts) highlighted in (A). Characteristic peak of TAMRA at  $1650\text{ cm}^{-1}$  is highlighted in yellow. SERS spectra were all obtained at  $\lambda_{\text{exc}} = 532\text{ nm}$ , using a 100 x objective, a laser power of  $25\text{ }\mu\text{W}$ , and integration times of 4s.

As was the case for AuNP dimers, no characteristic SERS spectra for PEPY could be observed (Figure A.8). This suggests that the sensitivity of the system needs to be further improved, potentially requiring a single molecule level sensitivity to observe molecules, which are not in resonance to the laser wavelength. As the EF is expected to be higher for AgNP dimers when excited at lower wavelengths than 532 nm (Figure A.7), utilizing wavelengths such as 488 nm could improve the EF. In addition, the structures could be more optimized to bring the dimers closer to each other as the EF in the hotspot increases with smaller gap sizes<sup>207</sup>.

#### 4.3.1. AuNRs

As the anisotropic shape of the nanorods give rise to interesting plasmonic properties, including high SERS enhancement factors when excited along the longitudinal axis of the nanorods<sup>206</sup>, efforts were made here to synthesize, characterize, and use them to explore optical properties of the plasmonic structures. Coating of AuNRs is not a simple task and many strategies have been explored by many scientists such as growing a layer of gold after synthesizing the nanorod<sup>146</sup>, growing a silica shell<sup>208</sup>, as well as low pH methods for rapid



coating<sup>136</sup>, which are either very time consuming or do not provide sufficient surface coverage. Here, a modified version of the low pH method was used to successfully coat the AuNRs with DNA and produce stable particles in high salt concentrations (0.5 M NaCl).

### Synthesis and characterization

Gold nanorods were synthesized according to the silver-assisted seed-mediated method as previously described in section 3.2.3. The aspect ratio (AR) of the nanorods could be altered by changing the amount of AgNO<sub>3</sub> added to the growth solution. Two examples of the synthesized AuNRs are shown in Figure 4.24, where both nanorods were synthesized with the identical seed solution, but AuNR 1 had a growth solution containing 100  $\mu$ L of 4 mM AgNO<sub>3</sub> solution whereas AuNR 2 had 150  $\mu$ L. The resulting nanorods were imaged *via* AFM, and the AR of the structures could be estimated (AuNR 1 had an AR of 2.6 and AuNR 2 had an AR of 3.2). Although the AFM is an excellent method to determine the height profile of the nanorods, it is not a precise method to determine the lateral dimensions due to the convolution of the nanorod structure with the shape of the tip (10 nm diameter tip). Therefore, only an estimate of the length of the nanorod can be given (the width dimension was taken from the height profile of the AuNRs). It must be noted here that in order to obtain good AFM images of the nanorods, they must be washed extensively (*via* centrifugation) prior to placing them on the Si chip (or mica) to minimize the CTAB surfactant in the solution, as the image can be blurry due to the charge from the surface of the particles repulsing the AFM tip and leading to inaccurate determinations of the AuNR height profiles.

Extinction spectra of the nanorods (Figure 4.24 (B)) showed clear distinction in the longitudinal LSPR of each nanorod with AuNR 1 showing a peak at 645 nm, and AuNR 2 at 740 nm. The seed solution which was used for synthesizing both of the nanorods is also shown, which does not show any LSPR peak due to the small size of the seeds. When the AR was calculated using the LSPR wavelength<sup>110</sup>, AuNR 1 and AuNR 2 had an AR of 2.4 and 3.3 indicating the limitations of using AFM for size distribution analysis of nanorods, for which other imaging techniques such as transmission electron microscopy (TEM) are required for full analysis (Figure 4.25).

### 4.3. DNA coated metal-nanoparticles with tailored optical properties

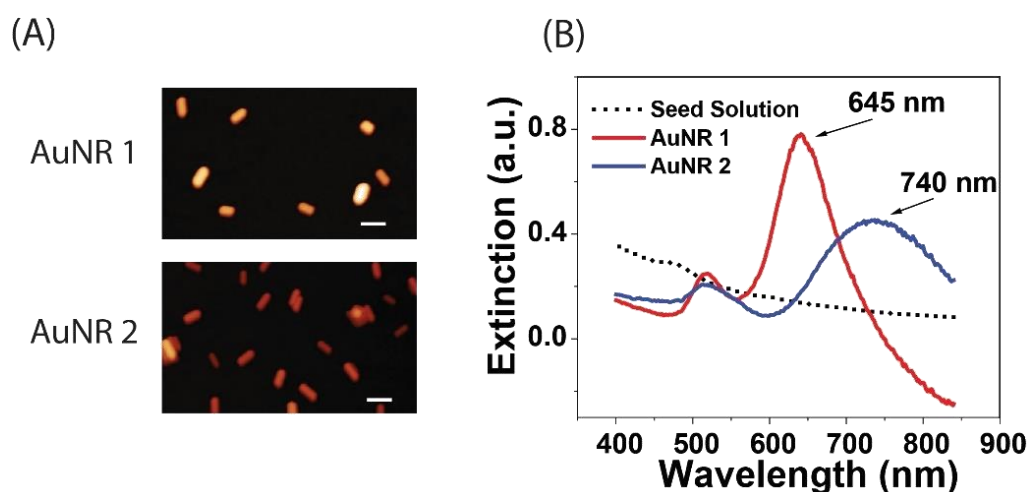


**Figure 4.24:** AuNR synthesis with different aspect ratios. (A) AFM images of the synthesized nanorods AuNR 1 (AR 2.6) and AuNR 2 (AR 3.2) (scale bar : 100 nm). (B) Extinction spectra of the AuNR 1 (red) and AuNR 2 (blue) as well as the seed solution (dotted line) was recorded. The two nanorods show distinctly different longitudinal LSPR, with AuNR 1 at 645 nm and AuNR 2 at 740 nm.

Although synthesizing AuNRs with different AR is relatively simple, synthesizing them with a small size and shape distribution is very difficult. The inhomogeneity can be clearly seen in TEM images as shown in Figure 4.25 (A). Two batches of nanorods were synthesized using the same conditions (from same seed solution with identical concentrations of  $\text{AgNO}_3$  in growth solution) and a difference in the spectra could be observed (Figure 4.25 (B)). The AuNRs with longitudinal LSPR at 632 nm had an AR of  $2.4 \pm 0.5$  (with a length of  $45 \pm 8$  nm and a width of  $19 \pm 5$  nm) according to the TEM images. This corresponded well with the calculated AR of 2.3, derived from the extinction spectra. The batch with the longitudinal LSPR at 635 nm had an AR of  $2.3 \pm 0.5$  (with a length of  $47 \pm 8$  nm, and a width of  $22 \pm 5$  nm) according to the TEM images, which again corresponds well with the calculated AR of 2.3 based on the extinction spectra. A variety of differently sized and shaped nanorods can be seen in the TEM images, and centrifugal separation can be used to increase the purity, although this method is quite inefficient<sup>209</sup>. Many groups have explored separation techniques such as multiphase centrifugal separation<sup>210</sup> and depletion-induced purification<sup>211</sup>. Whichever method was used, it was clear that the purification step will require much more time and effort as it needs to be tailored for each specific AuNR. Therefore, further efforts were not made to purify the synthesized nanorods other than to remove the excess reactants and reduce the CTAB in the solution for DNA coating.

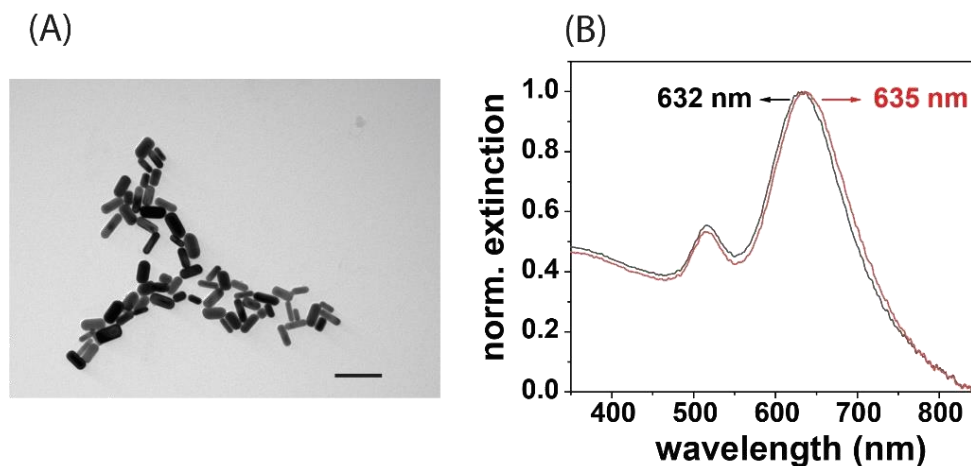


**Figure 4.25.:** AuNR analysis. (A) TEM image of AuNRs synthesized (scale bar 100 nm). Clear size and shape distributions can be seen. (B) Normalized spectra of two AuNR batches with identical synthesis conditions but with slightly different LSPR.

## Optical properties of a dye molecule near the AuNR surface

Optical properties of a dye molecule, as was discussed in section 2.4, depend on the distance between the metal surface and the dye molecule. In this section, with the intention of developing a dual nanoprobe for SEF and SERS, dsDNA was used as the spacer to place the dye molecule at a specific distance from the AuNR surface and TAMRA was used as the dye molecule (Figure 4.26).

According to literature, approximately at a distance of 10 nm from the surface of the AuNR an enhancement in the fluorescence should be observed<sup>120</sup>. At a closer distance, the emission intensity decreases as the fluorescence is quenched<sup>122</sup>. If the molecule is close enough to the surface (within a few nanometers), SERS can be observed<sup>123</sup>. Here, three different dsDNA pairs and a telomeric ssDNA strand was used as the spacer and dye placing tool (Figure 4.26 (A)). Thiol modified DNA sequences were attached to the surface of the AuNR *via* thiol-gold bond (detailed description of the coating procedure can be found in section 3.2.4). Hybridization with the complementary strand carrying the dye molecule allows for the placement of the dye at a given distance (except for the telomeric DNA sequence with both thiol and dye modifications). For DNA sequence **a'** the dye molecule would be placed at approximately 4.2 nm from the surface, whereas for **b'** and **c'** it would be placed at 9.8 nm from the surface of the nanorod. It was expected that for all of the three sequences (**a'**, **b'**, and **c'**) fluorescence emission from TAMRA would be observed, with **b'** and **c'** potentially

### 4.3. DNA coated metal-nanoparticles with tailored optical properties

showing SEF. For sequences **a**, and **b**, fluorescence was expected to be fully quenched and SERS to be observed. For the telomeric sequence **d'**, fluorescence emission was also expected.

However, when steady-state emission spectra were recorded ( $\lambda_{\text{exc}} = 535 \text{ nm}$ ) the only sequence that showed a faint fluorescence signal was the AuNR coated with  $(\text{TTT})_8\text{T}_4\text{-SH}$  that was hybridized with the **b'** sequence (Figure 4.26 (B)). The difference between sequence **b'** and **c'** is that in the case of **b'**, hybridization can occur anywhere along the  $(\text{TTT})_8\text{T}_4\text{-SH}$  sequence allowing for the dye molecule to be placed at distance that is further than 9.8 nm from the surface.

From Figure 4.26 (B), it was unclear whether the nanorods were in fact coated with the dsDNA, and therefore all the DNA was removed from the AuNR surface using excess DTT (as was explained in section 3.2.4.). As shown in Figure 4.26 (C), once the dsDNA was liberated from the surface of the AuNR, the fluorescence emission was restored and TAMRA emission could be detected ( $\lambda_{\text{emi}} = 580 \text{ nm}$ ). This proved two things; a) the AuNR coating with the thiol-modified DNA was successful, and b) the dye-labeled DNA was indeed hybridized. This conclusion however, also posed a further question. There was no SEF observed at approximately 10 nm from the surface of AuNR, and in fact most of the fluorescence was strongly quenched. This was especially surprising for the sequence **c'**, as this dsDNA does not allow for large variations of the distance.

In addition, it was clear that the hybridization yield is higher if the dye molecules are at the distal end than the closer end, as the emission intensity of **b'** is higher than **b**. Another fact that can be extracted from these spectra is that longer sequences work better for coating the nanorods, as the emission intensity of **a** and **a'** were very low (Figure A.10). As for the telomeric sequence (**d'**), two assumptions could be made. Either the ssDNA lies on the surface of the AuNR as the backbone is negatively charged and the surface of AuNR is positively charged (due to the CTAB bilayer on the surface) thus bringing the dye molecule very close to the surface and fully quenching the fluorescence, or the distance between the dye molecule and the surface is simply not far enough even if the DNA is protruding outward into the solution. The AuNR that was coated with dsDNA (with sequence **b** as the dye-labeled DNA) had an average of  $127 \pm 28$  dsDNA strands (Figure A.11).

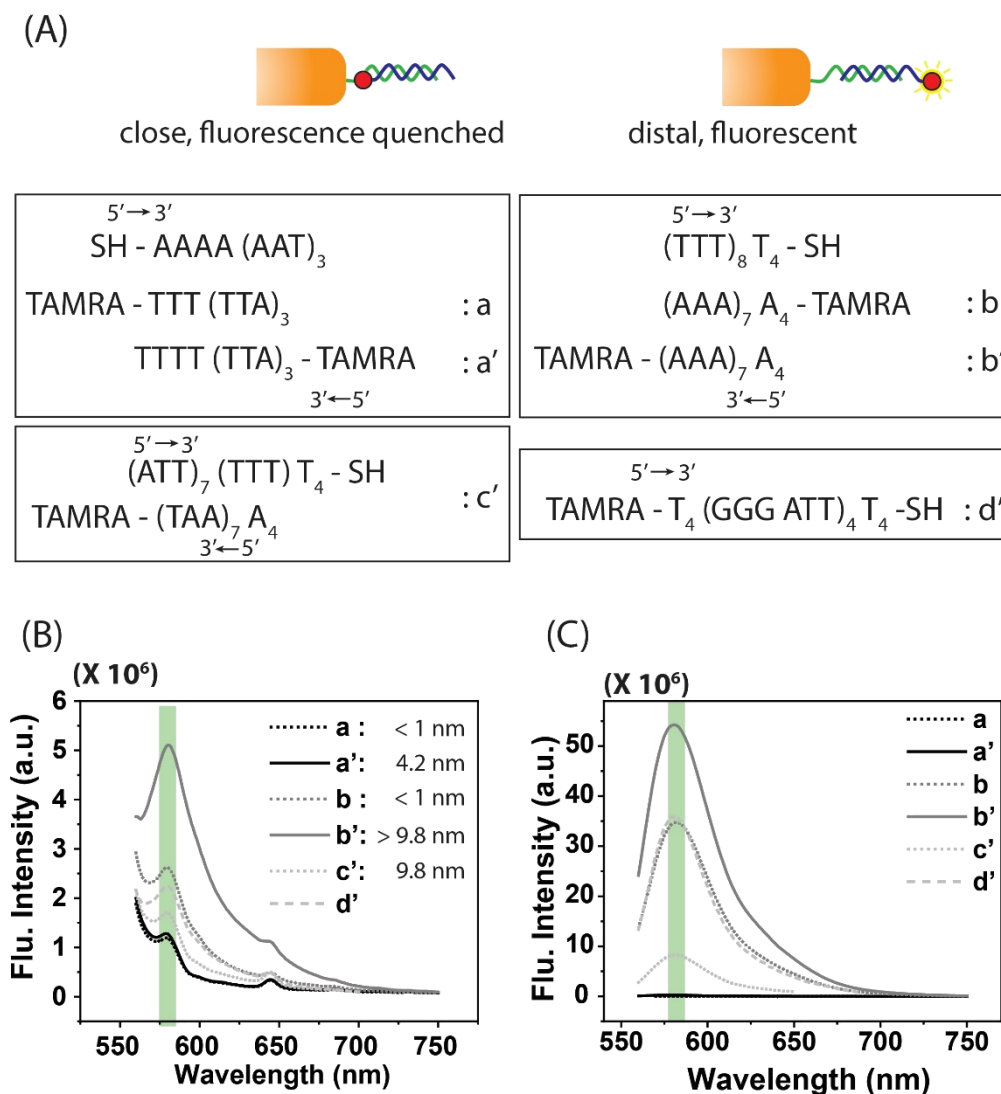


**Figure 4.26.:** Optical properties of TAMRA near the surface of AuNRs. (A) Schematic illustration of the dsDNA coated AuNRs either with the dye molecule close to the surface where the fluorescence is fully quenched, or with the dye molecule at the distal end where the fluorescence emission is not fully quenched. Different types of DNA sequences that were used are listed with the thiol-modified DNA written in 5' to 3' direction and the complementary dye-modified DNA written in the opposite direction. (B) Steady-state emission spectra of the DNA coated AuNRs ( $\lambda_{exc} = 535$  nm) show almost no TAMRA fluorescence ( $\lambda_{emi} = 580$  nm). Sequences labeled **a'**, **b'**, **c'**, and **d'** have the dye at the distal end whereas **a** and **b** have the dye at the close end quenching the fluorescence fully. The position of TAMRA from the surface of the AuNR is noted next to the sequence. (C) Steady-state emission spectra of DTT treated samples show recovered fluorescence of TAMRA when the DNA was liberated from the surface of the AuNRs.

### 4.3. DNA coated metal-nanoparticles with tailored optical properties

SERS spectra of AuNR coated with dye molecules close to the surface were recorded (**a** and **b**), however no characteristic TAMRA peaks could be observed (Figure A.12). It was postulated that for sequence **a**, there was not enough coverage of the dsDNA on the AuNR to detect the Raman signal. For sequence **b**, it is possible that the sequence hybridized in a way that the dye molecules were too far from the surface of the AuNR. For all sequences, it is also possible that the negatively charged phosphate backbone of the ssDNA adsorbs onto the side of the AuNR (not the apex) instead of binding *via* gold-thiol bond. This brings the TAMRA molecule close to the sides of the AuNR where the enhancement factors might not be high enough to observe SERS effects (Figure A.9).

### AuNR assembly on DNA origami nanostructure

As was observed, simply coating the AuNR surface with dsDNA did not provide adequate control of the distance between the surface of the nanorod and the dye molecule. DNA origami nanostructures were therefore used as a platform, which allows one to place the dye molecule at a specific distance from the surface of the AuNR, especially at the apex where the EF is largest (when exciting along the longitudinal axis of the nanorod, Figure A.9). This strategy could in principle also be used for the assembly of dimer structures with the dye molecule (TAMRA), placed in the gap ('hot-spot') between the two nanorods (Figure 4.27). This approach however, proved to be quite challenging as the DNA coated AuNR needed to be stable enough to withstand high ionic strength buffer (15 mM Mg<sup>2+</sup> for the DNA origami nanostructures). The stability of the metal particles is normally provided by a densely coated surface to protect the particles from aggregating, which was difficult to achieve with AuNRs, as was demonstrated in the previous section.

As can be seen from Figure 4.27 (A), placing one AuNR on the DNA origami nanostructure was successful with the correct orientation where the longitudinal axis of the AuNR was parallel to the edge of the trapezoid of the triangular DNA origami nanostructure that it was bound to. This structure could potentially be used to study EF of single AuNR as the placement of the analyte can be done easily on the DNA origami nanostructure<sup>126</sup>. AuNR dimers could also be assembled, as can be seen in Figure 4.27 (B). However, this proved to be more challenging as many dimer structures were assembled in a non-ideal manner such as two AuNRs formed side-to-side. This corresponds well with the theory that the thiol-modified DNA preferentially attaches to the apex of the nanorod rather than the sides (Figure 2.15). The inefficient DNA

coating of the nanorods was also shown in gel electrophoresis as many of the particles were stuck in the pocket (Figure 3.8). It can also be postulated here that having five to six capture strands on the DNA origami might not be enough to hold the AuNR in place, if trying to assemble dimers that are aligned along their longitudinal axis (capture strands listed in Table A.6).

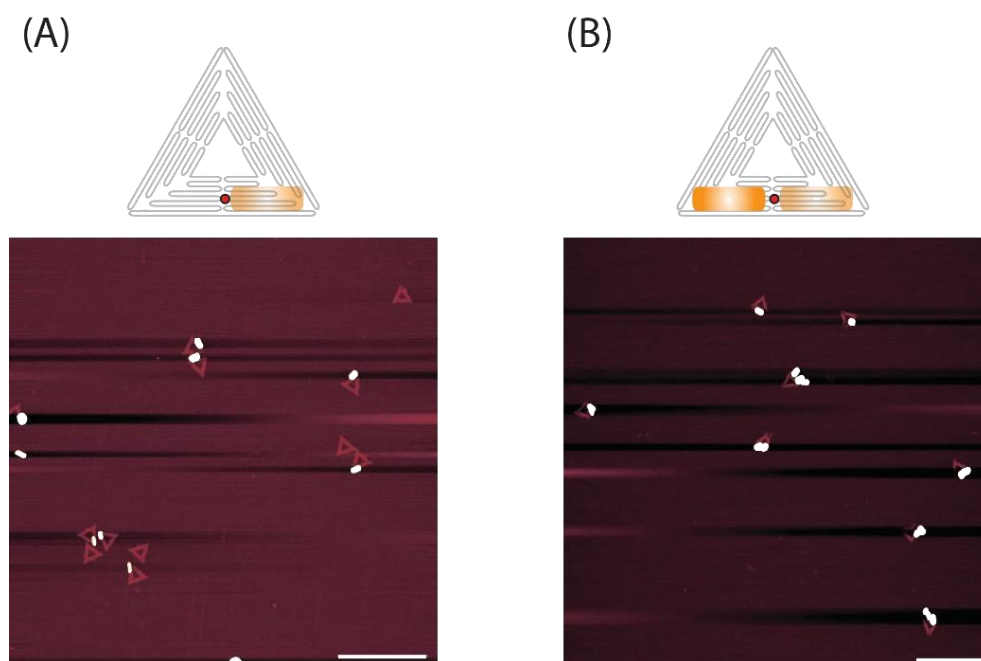


**Figure 4.27.:** Schematic illustration of the AuNR, dye molecule assembly on DNA origami nanostructures with the corresponding AFM image. (A) AuNR monomer placed on the DNA origami nanostructure, with TAMRA molecule (red circle) placed at the apex of the nanorod. (B) AuNR dimers assembled on the DNA origami nanostructure with the TAMRA placed in the gap along the longitudinal axis of the dimers. Scale bar represents 500 nm.

### 4.3.3. Conclusion

AuNPs, AgNPs, and AuNRs were used here as plasmonic substrates to investigate optical properties of dye molecules in the vicinity of the metal surface. Stable dye-labeled DNA coated AuNP and AgNP were produced and were assembled on DNA origami nanostructures. To assemble structures that could be used to determine field enhancement factors, the particles were coated either with a TAMRA-labeled DNA or a PEPY-labeled DNA so the dye could be used as the SERS analyte. Dimers of these structures could be successfully assembled using various sizes of AuNP as well as 60 nm AgNP. AgNPs proved to be quite challenging, especially using the TAMRA-labeled DNA due to the charge of the dye molecule. EF for 60nm AuNP dimer

### 4.3. DNA coated metal-nanoparticles with tailored optical properties

with an inter-particle distance of approximately 7 nm could be obtained here, using TAMRA as the analyte giving a 1.7 fold enhancement over a single nanoparticle. SERS spectra of TAMRA coated AgNP showed a potentially higher EF than AuNP at an excitation wavelength of 532 nm, as the number of TAMRA molecules per AgNP is expected to be lower than that per AuNP (due to the coating strategy) but the SERS intensity at  $1650\text{ cm}^{-1}$  was similar. In order to determine the direct  $EF_{SERS}$ , efforts were made to detect a dye molecule PEPY, which is not in resonance with the Raman laser used here. However, the  $\text{C}\equiv\text{C}$  stretching vibration of the PEPY dye molecule could not be observed with either AuNP or AgNP, confirming the importance of the resonance effect of the dye molecule, the comparatively low EF of the SERS substrates, and the need for further optimization of the structures. Achieving single molecule level sensitivity will allow for detection of such non-resonant dye molecules, which could open doors to studying EF at different excitation wavelengths for one system without relying on estimations as was the case when using TAMRA as the analyte.

It must be noted here that the yield of the dimer structures is very low ( $\sim 10\%$ ), and increasing the stoichiometric ratio of the nanoparticles to DNA origami nanostructures did not increase the yield. Even after purification *via* gel electrophoresis, the density of dimer structures did not increase significantly as many structures only have one AuNP on the DNA origami nanostructure which could not be separated by this purification method. For a better analysis of the EF, it is of interest to produce dimers with better yield.

AuNRs were also used here due to their interesting optical properties arising from their anisotropical shape. Because of the tight CTAB bilayer on the surface of the nanorods, coating them with thiol-modified DNA was difficult but stable particles in high salt concentrations were still produced. Contrary to published results where SEF was observed at dye-surface distances below 10 nm<sup>120,212</sup>, only fluorescence quenching was observed. AuNR monomers could be successfully assembled on the DNA origami potentially providing a better structure to study SEF as it gives more control over the dye-surface distance. However, when trying to assemble AuNR dimers on the DNA origami nanostructure it proved very challenging as the AuNRs were selectively coated on the apex with the thiol-modified DNA. This led to dimer structures that were not aligned along the longitudinal axis of the dimers (which provides the highest near-field enhancements) and forming undesirable structures where the two dimers are assembled side-to-side, or assembled at an angle. It is therefore imperative to optimize the dimer assembly for further EF studies.



## 5. Conclusion and Outlook

Triangular DNA origami nanostructures were used throughout this thesis as a platform to study nanophotonics, for both fluorescence emission and surface enhanced Raman scattering, utilizing the spatial addressability to place dye molecules as well as metal nanoparticles with nanometer scale accuracy.

Firstly, the DNA origami nanostructures were used as a platform to create various FRET nanoarrays of different sizes and patterns of donor and acceptor molecules at a ratio of 1:1. Steady-state and time-resolved fluorescence studies were conducted using FAM as the donor and Cy3 as the acceptor. The emission intensity ratio of donor and acceptor molecules as well as FRET efficiency could be optimized by; a) increasing the overall size of the nanoarray from a simple donor-acceptor pair (**2x1**) to a (**3x4**) array, and b) arranging the dye molecules in a checkerboard pattern, in which the dyes would also exhibit minimum self-quenching due to the large distance between identical dyes. The versatility of this nanoarray design was demonstrated by replacing the dye molecules according to the required application, without having to synthesize the DNA origami nanostructures from scratch. Here, based on the optimized optical properties, the (**3x4**) array in a checkerboard pattern was chosen and used in a proof-of-concept ratiometric pH sensor. A pH-inert C343 was used as the donor and the internal reference signal, and a pH-responsive FAM was used as the acceptor and the reporter signal. The emission intensity ratio as well as FRET efficiency within the biologically relevant pH ranges (pH 5 - pH 8) showed drastic changes for the (**3x4**) array compared to the **6 x (2x1)** array where the number of dye molecules is the same but the dye arrangement is different. This shows the potential of the nanoarray for ratiometric pH sensing. This array was further utilized as a proof-of-concept ratiometric toxin detector, in this case thioacetamide (TAA), where the TAA-inert C343 was used again as the donor/internal reference signal and TAA-responsive FAM was used as the acceptor/reporter signal.

## 5. Conclusion and Outlook

The DNA origami nanostructure was also used to develop a new reporter system for microbead-based assays to detect oligonucleotides, in this case the DNA equivalent of miRNA. The spatial addressability of the DNA origami nanostructure allowed for the reporter to carry multiple dye molecules (14 ATTO 647N molecules in this design), enhancing the emission intensity of each reporter. Additionally, probe sequences for hybridization with the target oligonucleotide could be placed away from the crowded dye labeled area of the DNA origami nanostructure. The target specificity in this sensing scheme was provided by a biotin modified target capture strand, which was bound to the streptavidin functionalized microbead. The target oligonucleotide with a poly A sequence (A<sub>40</sub>) at the 3'-end is immobilized on the surface of the microbead by hybridization to the reporter having a poly T (T<sub>40</sub>) sequence. A unique technique termed VideoScan was used to measure the fluorescence signals of the assay, where the dual fluorescence dye encoded microbeads were identified first (and grouped into a specific population), after which the surface fluorescence generated by the reporter was read. This method references the reporter signal back to the microbead fluorescence signal, thus making it a ratiometric sensor where the microbead is analyte-inert, and the reporter is analyte-responsive. A target response curve was obtained comparing two types of reporter, *ssDNA\_R* and the newly designed *DNA origami\_R*. The new reporter showed a better response to lower target oligonucleotide concentrations than the simple *ssDNA\_R*, with determined assay parameters such as LoD, LoQ and EC50 all showing lower values while the dynamic range was larger. As the target oligonucleotides all had an A<sub>40</sub> sequence at the 3'- end, the DNA origami reporter could be used in a proof-of-concept multiplexed analysis without making any changes to the design, with the fluorescence code of each microbead population used as the target specific identification tag. Signal amplification strategies were also explored by changing the binding strength of the *DNA origami\_R* and the target oligonucleotide which showed an increase in measured signal with the increase of ionic strength in the hybridization solution. However, other strategies such as increasing the number of probe strands *per DNA origami\_R*, or linking several DNA origami nanostructures together showed very little changes in the observed signal. The potential of using the DNA origami nanostructures as a novel reporter in multiplexed analysis was thus demonstrated, especially for lower target oligonucleotide concentrations in the pM range.

Not only could dye molecules be placed on the DNA origami nanostructure, but metal nanoparticles could also be strategically placed in relation to a dye molecule. These assemblies

provided the means to study plasmonics, with special interest in SERS and SEF. Designing a system to study SERS enhancement factors in the hot-spot between two metal nanoparticles for different excitation wavelengths and different materials was of particular interest here. Therefore, two different dye-labeled thiol-modified ssDNA strands were used to coat AuNPs and AgNPs; a) TAMRA that is resonant to the 532 nm excitation wavelength and b) PEPY that has an absorption band in the Blue/UV region and has a characteristic C≡C stretching Raman band away from all the signals observed from the DNA. 60 nm AuNPs that were coated with TAMRA labeled DNA, and assembled on the DNA origami nanostructure, showed a characteristic Raman band at 1650 cm<sup>-1</sup>. However, PEPY with a 'strong' C≡C stretching band at 2200 cm<sup>-1</sup> could not be detected although collecting normal Raman data was possible ( $\lambda_{exc} = 532$  nm). 60 nm AgNP, hypothesized to give much stronger near-field enhancements than AuNP when excited at 488 nm, were also assembled on the DNA origami as dimers. This proved to be more challenging than AuNP, especially with the TAMRA-labeled DNA as the dye molecules are charged. However, stable particles could be successfully produced and the characteristic SERS band of TAMRA could be observed. Coating AgNP with PEPY-labeled DNA was simple, as the dye is not charged. However, this again showed no characteristic SERS band. Overall the use of PEPY highlighted the importance of improving the sensitivity of the system for molecules with relatively small Raman cross sections, whether it may be through optimizing the structure or by choosing the appropriate excitation wavelength.

AuNRs, due to their anisotropic shape, provided interesting near-field enhancements with a tunable longitudinal LSPR. Although synthesizing the AuNR and tuning their LSPR was quite simple, producing pure samples within each batch (with small size distribution) was very difficult. In addition, due to the CTAB bilayer that is tightly packed around the nanorods coating these nanorods with thiol-modified ssDNA was not a simple task but was achieved through establishing new coating protocols. Using the DNA coated AuNRs, the optical properties of a dye molecule in the vicinity of the AuNR surface were studied by using dsDNA as a rigid spacer between the dye molecule and the surface of the AuNR. This did not require the AuNR to be stable in high ionic strength, and thus simplified the sample preparation step. However, no SEF was observed at distances that were expected to give rise to SEF and only fluorescence quenching was observed. It was apparent that the dsDNA does not provide adequate distance control between the surface of the AuNR and the dye molecule and therefore DNA origami nanostructures were utilized to tackle this aspect. Further efforts in

## 5. Conclusion and Outlook

coating the AuNR with DNA led to successful assembly of the particles on the DNA origami nanostructure. As hot-spots created in a nanoscale gap between two metallic particles give very high near-field enhancements, efforts were made to assemble AuNR dimers using the DNA origami as the platform. However, strategically placing two nanorods aligned along their longitudinal axis was very difficult as the apex of the nanorods were preferentially coated with the thiol-modified DNA, leading to a dimer structure with the two nanorods assembled side-by-side. This highlighted the importance of further improve the surface coverage of the AuNRs with DNA.

In summary, DNA origami nanostructures could be used in a variety of nanophotonic applications utilizing the spatial addressability, including a ratiometric sensor, a reporter molecule for miRNA detection with low copy number, as well as for plasmonics. The FRET nanoarray designed here can be easily extended to the detection of other analytes enabling a broad range of applications such as a  $F^-$  and  $CN^-$  sensor utilizing naphthalimide as the Do and squaraine as the Ac<sup>213</sup>, a  $Hg^{2+}$  sensor using leuco-rhodamine derivative as the Do and BODIPY as the Ac<sup>195</sup>, and a hydrogen peroxide sensor based on coumarin-fluorescein derivatives<sup>18</sup>. Since DNA origami nanostructures have been previously demonstrated to be taken up by cells, they could also be utilized as intracellular probes<sup>214–216</sup>. It would also be interesting to conduct single particle fluorescence measurements to determine the hybridization yield of the dye-labeled DNA on the DNA origami nanostructure, as this might influence the observed Do to Ac emission intensity ratio. As for the reporters developed for microbead-based assays, although the LoD was comparable to previously reported values in the femtomolar region<sup>24,217,218</sup>, it was apparent that the hybridization on the surface of microbeads was much more complex than anticipated. Optimizing the shape of the DNA origami nanostructures, such as using a more compact three-dimensional structure<sup>9,219,220</sup>, could provide better placement of dye molecules as well as hybridization of the DNA origami nanostructure to the microbead surface. In addition, utilizing synthetic DNA analogues for probe sequences such as peptide nucleic acid (PNA) or locked nucleic acid (LNA) that have been reported to have increased binding efficiency to oligonucleotides could provide better binding of the reporter to the target and potentially increase the measured signal<sup>221,222</sup>. As well, it would be of great interest to be able to do real multiplex analysis with the DNA origami reporters since the use of miRNA as biomarkers requires profiling of many different sequences. In addition, the unmatched nanoscale control of placing objects of interest by utilizing DNA origami nanostructures

provides a unique potential to study plasmonics. This could provide much more insight into the diverse optical effects that happen in the vicinity of the metal nanoparticles. For such studies, however, several key components during sample preparation must be further optimized, including improving the yield of dimer structures. Whether it may be through purification or by optimizing the stoichiometry of nanoparticles and DNA origami nanostructures, a better yield of the dimer structures would be beneficial in determining enhancement factors for SERS. Single particle fluorescence measurements would also be very interesting here as bulk measurements only showed quenching phenomena of the fluorophore near the metal surface. Dimer structures with a single fluorophore between the particles, as was previously demonstrated<sup>58</sup>, could be done here as well. A systematic study of comparing SEF and SERS of identical structures at different excitation wavelengths could therefore be conducted. Although correlating AFM images with SERS maps provides the means to assign each spectrum to a specific structure, it is very labor intensive. This could be improved by obtaining extinction spectra maps<sup>223</sup> of the assembled structures which could easily distinguish a single particle from a dimer, and correlating this with the SERS map. Dark field scattering<sup>223</sup> would also be beneficial to the study of the dimers, which can be conducted on the same sample, providing various information about the structure.

The work presented here shows the versatility of using the DNA origami technique, ranging from applications in fluorescence-based sensing for biologically relevant molecules to fundamental studies regarding plasmonics. It is not surprising that these techniques are attracting great interest, and it is likely that many more developments will be made in the future whether it may be in fundamental research or in real-life sensing applications.

# Bibliography

- (1) Feynman, R. There's Plenty of Room at the Bottom. *Engineering and Science* **1960**, *23*.
- (2) Tanihuchi N. On the basic concept of Nano-technology. *Proceedings of International Conference on Production Engineering Tokyo* **1974**, *2*, 18–23.
- (3) Binnig, G.; Rohrer, H.; Gerber, C.; Weibel, E. Surface Studies by Scanning Tunneling Microscopy. *Phys. Rev. Lett.* **1982**, *49*, 57–61.
- (4) Liddle, J. A.; Gallatin, G. M. Nanomanufacturing: A Perspective. *ACS Nano* **2016**, *10*, 2995–3014.
- (5) Imboden, M.; Bishop, D. Top-down nanomanufacturing. *Physics Today* **2014**, *67*, 45–50.
- (6) Alberts, B.; Johnson, A.; Lewis, J.; Raff, M.; Roberts, K.; Walter, P. *Molecular Biology of the Cell Fifth Edition*; Garland Science; [Taylor & Francis, distributor]: New York, [London], 2008.
- (7) Seeman, N. C. Nucleic acid junctions and lattices. *J Theor Biol* **1982**, *99*, 237–247.
- (8) Rothemund, P. W. K. Folding DNA to create nanoscale shapes and patterns. *Nature* **2006**, *440*, 297–302.
- (9) Castro, C. E.; Kilchherr, F.; Kim, D.-N.; Shiao, E. L.; Wauer, T.; Wortmann, P.; Bathe, M.; Dietz, H. A primer to scaffolded DNA origami. *Nat Methods* **2011**, *8*, 221–229.
- (10) Lakowicz, J. R. *Principles of Fluorescence Spectroscopy*; Springer US: Boston, MA, 2006.
- (11) Resch-Genger, U.; Grabolle, M.; Cavaliere-Jaricot, S.; Nitschke, R.; Nann, T. Quantum dots versus organic dyes as fluorescent labels. *Nat Methods* **2008**, *5*, 763–775.
- (12) Fleige, E.; Ziem, B.; Grabolle, M.; Haag, R.; Resch-Genger, U. Aggregation Phenomena of Host and Guest upon the Loading of Dendritic Core-Multishell Nanoparticles with Solvatochromic Dyes. *Macromolecules* **2012**, *45*, 9452–9459.
- (13) Pauli, J.; Grabolle, M.; Brehm, R.; Spieles, M.; Hamann, F. M.; Wenzel, M.; Hilger, I.; Resch-Genger, U. Suitable labels for molecular imaging--influence of dye structure and hydrophilicity on the spectroscopic properties of IgG conjugates. *Bioconjug Chem* **2011**, *22*, 1298–1308.
- (14) *The molecular probes handbook: A guide to fluorescent probes and labeling technologies*; Spence, M. T. Z.; Johnson, I. D., Eds., 11th ed.; Live Technologies Corporation: [Carlsbad, CA], op. 2010.
- (15) Goldberg, J. M.; Batjargal, S.; Chen, B. S.; Petersson, E. J. Thioamide quenching of fluorescent probes through photoinduced electron transfer: Mechanistic studies and applications. *J Am Chem Soc* **2013**, *135*, 18651–18658.
- (16) Medintz, I. L.; Hildebrandt, N. *FRET - Forster resonance energy transfer: From theory to applications*; Wiley-VCH Verlag GmbH: Weinheim, Germany, 2014.
- (17) Olejko, L.; Cywinski, P. J.; Bald, I. Ion-selective formation of a guanine quadruplex on DNA origami structures. *Angew Chem Int Ed Engl* **2015**, *54*, 673–677.
- (18) Albers, A. E.; Okreglak, V. S.; Chang, C. J. A FRET-based approach to ratiometric fluorescence detection of hydrogen peroxide. *J Am Chem Soc* **2006**, *128*, 9640–9641.
- (19) Meier, R. J.; Simbürger, J. M. B.; Soukka, T.; Schäferling, M. A FRET based pH probe with a broad working range applicable to referenced ratiometric dual wavelength and luminescence lifetime read out. *Chem Commun (Camb)* **2015**, *51*, 6145–6148.
- (20) Hemmig, E. A.; Creatore, C.; Wünsch, B.; Hecker, L.; Mair, P.; Parker, M. A.; Emmott, S.; Tinnefeld, P.; Keyser, U. F.; Chin, A. W. Programming Light-Harvesting Efficiency Using DNA Origami. *Nano Lett* **2016**, *16*, 2369–2374.
- (21) Olejko, L.; Bald, I. FRET efficiency and antenna effect in multi-color DNA origami-based light harvesting systems. *RSC Adv.* **2017**, *7*, 23924–23934.
- (22) Clapp, A. R.; Medintz, I. L.; Mauro, J. M.; Fisher, B. R.; Bawendi, M. G.; Mattoussi, H. Fluorescence resonance energy transfer between quantum dot donors and dye-labeled protein acceptors. *J Am Chem Soc* **2004**, *126*, 301–310.

- (23) Craw, P.; Balachandran, W. Isothermal nucleic acid amplification technologies for point-of-care diagnostics: A critical review. *Lab Chip* **2012**, *12*, 2469–2486.
- (24) Rödiger, S.; Schierack, P.; Böhm, A.; Nitschke, J.; Berger, I.; Frömmel, U.; Schmidt, C.; Ruhland, M.; Schimke, I.; Roggenbuck, D.; Lehmann, W.; Schröder, C. A highly versatile microscope imaging technology platform for the multiplex real-time detection of biomolecules and autoimmune antibodies. *Adv Biochem Eng Biotechnol* **2013**, *133*, 35–74.
- (25) Le Ru, E. C.; Etchegoin, P. G. *Principles of surface-enhanced Raman spectroscopy: And related plasmonic effects*, 1st ed.; Elsevier: Amsterdam, Boston, 2009.
- (26) Lakowicz, J. R. Radiative decay engineering 5: Metal-enhanced fluorescence and plasmon emission. *Anal Biochem* **2005**, *337*, 171–194.
- (27) Prinz, J.; Heck, C.; Ellerik, L.; Merk, V.; Bald, I. DNA origami based Au-Ag-core-shell nanoparticle dimers with single-molecule SERS sensitivity. *Nanoscale* **2016**, *8*, 5612–5620.
- (28) Heck, C.; Kanehira, Y.; Kneipp, J.; Bald, I. Placement of Single Proteins within the SERS Hot Spots of Self-Assembled Silver Nanolenses. *Angew Chem Int Ed Engl* **2018**, *57*, 7444–7447.
- (29) Halas, N. J.; Lal, S.; Chang, W.-S.; Link, S.; Nordlander, P. Plasmons in strongly coupled metallic nanostructures. *Chem Rev* **2011**, *111*, 3913–3961.
- (30) Watson, J. D.; Crick, F. H. C. Molecular Structure of Nucleic Acids: A Structure for Deoxyribose Nucleic Acid. *Nature* **1953**, *171*, 737–738.
- (31) Franklin, R. E.; Gosling, R. G. The structure of sodium thymonucleate fibres. I. The influence of water content. *Acta Cryst* **1953**, *6*, 673–677.
- (32) Seeman, N. C. At the Crossroads of Chemistry, Biology, and Materials. *Chemistry & Biology* **2003**, *10*, 1151–1159.
- (33) Yakovchuk, P.; Protozanova, E.; Frank-Kamenetskii, M. D. Base-stacking and base-pairing contributions into thermal stability of the DNA double helix. *Nucleic Acids Res* **2006**, *34*, 564–574.
- (34) Seeman, N. C.; Kallenbach, N. R. Design of immobile nucleic acid junctions. *Biophysical Journal* **1983**, *44*, 201–209.
- (35) Ma, R.-I.; Kallenbach, N. R.; Sheardy, R. D.; Petrillo, M. L.; Seeman, N. C. Three-arm nucleic acid junctions are flexible. *Nucl Acids Res* **1986**, *14*, 9745–9753.
- (36) Wang, Y.; Mueller, J. E.; Kemper, B.; Seeman, N. C. Assembly and characterization of five-arm and six-arm DNA branched junctions. *Biochemistry* **2002**, *30*, 5667–5674.
- (37) Wang, X.; Seeman, N. C. Assembly and characterization of 8-arm and 12-arm DNA branched junctions. *J Am Chem Soc* **2007**, *129*, 8169–8176.
- (38) Fu, T. J.; Seeman, N. C. DNA double-crossover molecules. *Biochemistry* **2002**, *32*, 3211–3220.
- (39) Winfree, E.; Liu, F.; Wenzler, L. A.; Seeman, N. C. Design and self-assembly of two-dimensional DNA crystals. *Nature* **1998**, *394*, 539–544.
- (40) He, Y.; Chen, Y.; Liu, H.; Ribbe, A. E.; Mao, C. Self-assembly of hexagonal DNA two-dimensional (2D) arrays. *J Am Chem Soc* **2005**, *127*, 12202–12203.
- (41) He, Y.; Tian, Y.; Ribbe, A. E.; Mao, C. Highly connected two-dimensional crystals of DNA six-point-stars. *J Am Chem Soc* **2006**, *128*, 15978–15979.
- (42) Yan, H.; Park, S. H.; Finkelstein, G.; Reif, J. H.; LaBean, T. H. DNA-templated self-assembly of protein arrays and highly conductive nanowires. *Science* **2003**, *301*, 1882–1884.
- (43) Zheng, J.; Birktoft, J. J.; Chen, Y.; Wang, T.; Sha, R.; Constantinou, P. E.; Ginell, S. L.; Mao, C.; Seeman, N. C. From molecular to macroscopic via the rational design of a self-assembled 3D DNA crystal. *Nature* **2009**, *461*, 74–77.
- (44) Tian, C.; Li, X.; Liu, Z.; Jiang, W.; Wang, G.; Mao, C. Directed Self-Assembly of DNA Tiles into Complex Nanocages. *Angew. Chem.* **2014**, *126*, 8179–8182.
- (45) Wang, P.; Wu, S.; Tian, C.; Yu, G.; Jiang, W.; Wang, G.; Mao, C. Retrosynthetic Analysis-Guided Breaking Tile Symmetry for the Assembly of Complex DNA Nanostructures. *J Am Chem Soc* **2016**, DOI: 10.1021/jacs.6b06074.

- (46) Shih, W. M.; Quispe, J. D.; Joyce, G. F. A 1.7-kilobase single-stranded DNA that folds into a nanoscale octahedron. *Nature* **2004**, *427*, 618–621.
- (47) *Tiamat: A Three-Dimensional Editing Tool for Complex DNA Structures: DNA Computing*; Goel, A.; Simmel, F. C.; Sosík, P.; Williams, S.; Lund, K.; Lin, C.; Wonka, P.; Lindsay, S.; Yan, H., Eds.; Springer Berlin Heidelberg, 2009.
- (48) Andersen, E. S.; Dong, M.; Nielsen, M. M.; Jahn, K.; Lind-Thomsen, A.; Mamdouh, W.; Gothelf, K. V.; Besenbacher, F.; Kjems, J. DNA origami design of dolphin-shaped structures with flexible tails. *ACS Nano* **2008**, *2*, 1213–1218.
- (49) Douglas, S. M.; Marblestone, A. H.; Teerapittayanon, S.; Vazquez, A.; Church, G. M.; Shih, W. M. Rapid prototyping of 3D DNA-origami shapes with caDNAno. *Nucleic Acids Res* **2009**, *37*, 5001–5006.
- (50) Steinhauer, C.; Jungmann, R.; Sobey, T. L.; Simmel, F. C.; Tinnefeld, P. DNA origami as a nanoscopic ruler for super-resolution microscopy. *Angew Chem Int Ed Engl* **2009**, *48*, 8870–8873.
- (51) Jungmann, R.; Steinhauer, C.; Scheible, M.; Kuzyk, A.; Tinnefeld, P.; Simmel, F. C. Single-molecule kinetics and super-resolution microscopy by fluorescence imaging of transient binding on DNA origami. *Nano Lett* **2010**, *10*, 4756–4761.
- (52) Stein, I. H.; Steinhauer, C.; Tinnefeld, P. Single-molecule four-color FRET visualizes energy-transfer paths on DNA origami. *J Am Chem Soc* **2011**, *133*, 4193–4195.
- (53) Keller, A.; Bald, I.; Rotaru, A.; Cauët, E.; Gothelf, K. V.; Besenbacher, F. Probing electron-induced bond cleavage at the single-molecule level using DNA origami templates. *ACS Nano* **2012**, *6*, 4392–4399.
- (54) Vogel, S.; Rackwitz, J.; Schürman, R.; Prinz, J.; Milosavljević, A. R.; Réfrégiers, M.; Giuliani, A.; Bald, I. Using DNA origami nanostructures to determine absolute cross sections for UV photon-induced DNA strand breakage. *J Phys Chem Lett* **2015**, *6*, 4589–4593.
- (55) Rackwitz, J.; Kopyra, J.; Dąbkowska, I.; Ebel, K.; Ranković, M. L.; Milosavljević, A. R.; Bald, I. Sensitizing DNA Towards Low-Energy Electrons with 2-Fluoroadenine. *Angew Chem Int Ed Engl* **2016**, *55*, 10248–10252.
- (56) Heck, C.; Kanehira, Y.; Kneipp, J.; Bald, I. Placement of Single Proteins within the SERS Hot Spots of Self-Assembled Silver Nanolenses. *Angew Chem Int Ed Engl* **2018**, DOI: 10.1002/anie.201801748.
- (57) Thacker, V. V.; Herrmann, L. O.; Sigle, D. O.; Zhang, T.; Liedl, T.; Baumberg, J. J.; Keyser, U. F. DNA origami based assembly of gold nanoparticle dimers for surface-enhanced Raman scattering. *Nat Commun* **2014**, *5*, 3448.
- (58) Acuna, G. P.; Möller, F. M.; Holzmeister, P.; Beater, S.; Lalkens, B.; Tinnefeld, P. Fluorescence enhancement at docking sites of DNA-directed self-assembled nanoantennas. *Science* **2012**, *338*, 506–510.
- (59) Puchkova, A.; Vietz, C.; Pibiri, E.; Wünsch, B.; Sanz Paz, M.; Acuna, G. P.; Tinnefeld, P. DNA Origami Nanoantennas with over 5000-fold Fluorescence Enhancement and Single-Molecule Detection at 25  $\mu$ M. *Nano Lett* **2015**, *15*, 8354–8359.
- (60) Stokes, G. G. On the Change of Refrangibility of Light. *Philosophical Transactions of the Royal Society of London* **1852**, *142*, 463–562.
- (61) Valeur, B.; Berberan-Santos, M. N. A Brief History of Fluorescence and Phosphorescence before the Emergence of Quantum Theory. *J. Chem. Educ.* **2011**, *88*, 731–738.
- (62) Teunissen, A. J. P.; Pérez-Medina, C.; Meijerink, A.; Mulder, W. J. M. Investigating supramolecular systems using Förster resonance energy transfer. *Chem Soc Rev* **2018**, DOI: 10.1039/c8cs00278a.
- (63) Valeur, B.; Berberan-Santos, M. N. *Molecular Fluorescence*; Wiley-VCH Verlag GmbH & Co. KGaA: Weinheim, Germany, 2012.
- (64) Medintz, I.; Hildebrandt, N. *FRET - Förster Resonance Energy Transfer*; Wiley-VCH Verlag GmbH & Co. KGaA: Weinheim, Germany, 2013.



- (65) Fan, J.; Hu, M.; Zhan, P.; Peng, X. Energy transfer cassettes based on organic fluorophores: Construction and applications in ratiometric sensing. *Chem Soc Rev* **2013**, *42*, 29–43.
- (66) Schäferling, M.; Duerkop, A. Intrinsically Referenced Fluorimetric Sensing and Detection Schemes: Methods, Advantages and Applications. In *Standardization and quality assurance in fluorescence measurements I: Techniques*; Resch-Genger, U., Ed.; Springer Series on Fluorescence 5; Springer Berlin Heidelberg: Berlin, Heidelberg, 2008; pp 373–414.
- (67) Wu, C.; Bull, B.; Christensen, K.; McNeill, J. Ratiometric single-nanoparticle oxygen sensors for biological imaging. *Angew Chem Int Ed Engl* **2009**, *48*, 2741–2745.
- (68) Wen, Z.-C.; Jiang, Y.-B. Ratiometric dual fluorescent receptors for anions under intramolecular charge transfer mechanism. *Tetrahedron* **2004**, *60*, 11109–11115.
- (69) Li, Y.-P.; Yang, H.-R.; Zhao, Q.; Song, W.-C.; Han, J.; Bu, X.-H. Ratiometric and selective fluorescent sensor for Zn<sup>2+</sup> as an "off-on-off" switch and logic gate. *Inorg Chem* **2012**, *51*, 9642–9648.
- (70) Henary, M. M.; Wu, Y.; Fahrni, C. J. Zinc(II)-selective ratiometric fluorescent sensors based on inhibition of excited-state intramolecular proton transfer. *Chemistry* **2004**, *10*, 3015–3025.
- (71) Henary, M. M.; Wu, Y.; Cody, J.; Sumalekshmy, S.; Li, J.; Mandal, S.; Fahrni, C. J. Excited-state intramolecular proton transfer in 2-(2'-arylsulfonamidophenyl)benzimidazole derivatives: The effect of donor and acceptor substituents. *J Org Chem* **2007**, *72*, 4784–4797.
- (72) Demchenko, A. P. *Introduction to Fluorescence Sensing*; Springer Netherlands: Dordrecht, 2009.
- (73) Whitaker, J. E.; Haugland, R. P.; Prendergast, F. G. Spectral and photophysical studies of benzo[c]xanthene dyes: Dual emission pH sensors. *Anal Biochem* **1991**, *194*, 330–344.
- (74) Peng, X.; Wu, Y.; Fan, J.; Tian, M.; Han, K. Colorimetric and ratiometric fluorescence sensing of fluoride: Tuning selectivity in proton transfer. *J Org Chem* **2005**, *70*, 10524–10531.
- (75) Han, J.; Burgess, K. Fluorescent indicators for intracellular pH. *Chem Rev* **2010**, *110*, 2709–2728.
- (76) Tsien, R. Y. New calcium indicators and buffers with high selectivity against magnesium and protons: Design, synthesis, and properties of prototype structures. *Biochemistry* **1980**, *19*, 2396–2404.
- (77) Grynkiewicz, G.; Poenie, M.; Tsien, R. Y. A new generation of Ca<sup>2+</sup> indicators with greatly improved fluorescence properties. *J Biol Chem* **1985**, *260*, 3440–3450.
- (78) Lee, M. H.; Kim, H. J.; Yoon, S.; Park, N.; Kim, J. S. Metal ion induced FRET OFF-ON in tren/dansyl-appended rhodamine. *Org Lett* **2008**, *10*, 213–216.
- (79) Ueberfeld, J.; Walt, D. R. Reversible ratiometric probe for quantitative DNA measurements. *Anal Chem* **2004**, *76*, 947–952.
- (80) Takakusa, H.; Kikuchi, K.; Urano, Y.; Sakamoto, S.; Yamaguchi, K.; Nagano, T. Design and Synthesis of an Enzyme-Cleavable Sensor Molecule for Phosphodiesterase Activity Based on Fluorescence Resonance Energy Transfer. *J. Am. Chem. Soc.* **2002**, *124*, 1653–1657.
- (81) Zhou, X.; Su, F.; Lu, H.; Senechal-Willis, P.; Tian, Y.; Johnson, R. H.; Meldrum, D. R. An FRET-based ratiometric chemosensor for in vitro cellular fluorescence analyses of pH. *Biomaterials* **2012**, *33*, 171–180.
- (82) Barilero, T.; Le Saux, T.; Gosse, C.; Jullien, L. Fluorescent thermometers for dual-emission-wavelength measurements: Molecular engineering and application to thermal imaging in a microsystem. *Anal Chem* **2009**, *81*, 7988–8000.
- (83) Didenko, V. V. DNA probes using fluorescence resonance energy transfer (FRET): Designs and applications. *BioTechniques* **2001**, *31*, 1106-16, 1118, 1120-1.
- (84) Long, L.; Lin, W.; Chen, B.; Gao, W.; Yuan, L. Construction of a FRET-based ratiometric fluorescent thiol probe. *Chem Commun (Camb)* **2011**, *47*, 893–895.
- (85) Shao, J.; Sun, H.; Guo, H.; Ji, S.; Zhao, J.; Wu, W.; Yuan, X.; Zhang, C.; James, T. D. A highly selective red-emitting FRET fluorescent molecular probe derived from BODIPY for the detection of cysteine and homocysteine: An experimental and theoretical study. *Chem. Sci.* **2012**, *3*, 1049–1061.

- (86) Atilgan, S.; Ozdemir, T.; Akkaya, E. U. Selective Hg(II) sensing with improved Stokes shift by coupling the internal charge transfer process to excitation energy transfer. *Org Lett* **2010**, *12*, 4792–4795.
- (87) Collins, F. S. Contemplating the end of the beginning. *Genome Res* **2001**, *11*, 641–643.
- (88) Rödiger, S.; Liebsch, C.; Schmidt, C.; Lehmann, W.; Resch-Genger, U.; Schedler, U.; Schierack, P. Nucleic acid detection based on the use of microbeads: A review. *Microchim Acta* **2014**, *181*, 1151–1168.
- (89) Lee, J.; Ha, J. U.; Choe, S.; Lee, C.-S.; Shim, S. E. Synthesis of highly monodisperse polystyrene microspheres via dispersion polymerization using an amphoteric initiator. *J Colloid Interface Sci* **2006**, *298*, 663–671.
- (90) Rödiger, S.; Ruhland, M.; Schmidt, C.; Schröder, C.; Grossmann, K.; Böhm, A.; Nitschke, J.; Berger, I.; Schimke, I.; Schierack, P. Fluorescence dye adsorption assay to quantify carboxyl groups on the surface of poly(methyl methacrylate) microbeads. *Anal Chem* **2011**, *83*, 3379–3385.
- (91) Fernandez Oropeza, N.; Zurek, N. A.; La Galvan-De Cruz, M.; Fabry-Wood, A.; Fetzer, J. M.; Graves, S. W.; Shreve, A. P. Multiplexed Lipid Bilayers on Silica Microspheres for Analytical Screening Applications. *Anal Chem* **2017**, *89*, 6440–6447.
- (92) Wilson, R.; Cossins, A. R.; Spiller, D. G. Encoded microcarriers for high-throughput multiplexed detection. *Angew Chem Int Ed Engl* **2006**, *45*, 6104–6117.
- (93) Vignali, D. A.A. Multiplexed particle-based flow cytometric assays. *Journal of Immunological Methods* **2000**, *243*, 243–255.
- (94) Xu, H.; Sha, M. Y.; Wong, E. Y.; Uphoff, J.; Xu, Y.; Treadway, J. A.; Truong, A.; O'Brien, E.; Asquith, S.; Stubbins, M.; Spurr, N. K.; Lai, E. H.; Mahoney, W. Multiplexed SNP genotyping using the Qbead system: A quantum dot-encoded microsphere-based assay. *Nucleic Acids Res* **2003**, *31*, e43.
- (95) Jin, R.; Cao, Y. C.; Thaxton, C. S.; Mirkin, C. A. Glass-bead-based parallel detection of DNA using composite Raman labels. *Small* **2006**, *2*, 375–380.
- (96) Horejsh, D.; Martini, F.; Poccia, F.; Ippolito, G.; Di Caro, A.; Capobianchi, M. R. A molecular beacon, bead-based assay for the detection of nucleic acids by flow cytometry. *Nucleic Acids Res* **2005**, *33*, e13.
- (97) Pregibon, D. C.; Toner, M.; Doyle, P. S. Multifunctional encoded particles for high-throughput biomolecule analysis. *Science* **2007**, *315*, 1393–1396.
- (98) Ohrmalm, C.; Jobs, M.; Eriksson, R.; Golbob, S.; Elfaitouri, A.; Benachenhou, F.; Strømme, M.; Blomberg, J. Hybridization properties of long nucleic acid probes for detection of variable target sequences, and development of a hybridization prediction algorithm. *Nucleic Acids Res* **2010**, *38*, e195.
- (99) Macey, M. G. *Flow Cytometry*; Humana Press: Totowa, NJ, 2007.
- (100) Whitesides, G. M. The origins and the future of microfluidics. *Nature* **2006**, *442*, 368–373.
- (101) Ng, J. K.-K.; Wang, W.; Liu, W.-T.; Chong, S. S. Spatially addressable bead-based biosensor for rapid detection of beta-thalassemia mutations. *Anal Chim Acta* **2010**, *658*, 193–196.
- (102) Brenner, S.; Johnson, M.; Bridgham, J.; Golda, G.; Lloyd, D. H.; Johnson, D.; Luo, S.; McCurdy, S.; Foy, M.; Ewan, M.; Roth, R.; George, D.; Eletr, S.; Albrecht, G.; Vermaas, E.; Williams, S. R.; Moon, K.; Burcham, T.; Pallas, M.; DuBridge, R. B.; Kirchner, J.; Fearon, K.; Mao, J.; Corcoran, K. Gene expression analysis by massively parallel signature sequencing (MPSS) on microbead arrays. *Nat Biotechnol* **2000**, *18*, 630–634.
- (103) Sasuga, Y.; Tani, T.; Hayashi, M.; Yamakawa, H.; Ohara, O.; Harada, Y. Development of a microscopic platform for real-time monitoring of biomolecular interactions. *Genome Res* **2006**, *16*, 132–139.
- (104) Schmidt, C.; Rödiger, S.; Gruner, M.; Moncsek, A.; Stohwasser, R.; Hanack, K.; Schierack, P.; Schröder, C. Multiplex localization of sequential peptide epitopes by use of a planar microbead chip. *Anal Chim Acta* **2016**, *908*, 150–160.

- (105) Liebsch, C.; Rödiger, S.; Böhm, A.; Nitschke, J.; Weinreich, J.; Fruth, A.; Roggenbuck, D.; Lehmann, W.; Schedler, U.; Juretzek, T.; Schierack, P. Solid-phase microbead array for multiplex O-serotyping of *Escherichia coli*. *Microchim Acta* **2017**, *184*, 1405–1415.
- (106) Mie, G. Beiträge zur Optik trüber Medien, speziell kolloidaler Metallösungen. *Ann. Phys.* **1908**, *330*, 377–445.
- (107) Maier, S. A. *Plasmonics: Fundamentals and Applications*; Springer Science+Business Media, LLC: Boston, MA, 2007.
- (108) Johnson, P. B.; Christy, R. W. Optical Constants of the Noble Metals. *Phys. Rev. B* **1972**, *6*, 4370–4379.
- (109) Schlücker, S. *Surface enhanced Raman spectroscopy: Analytical, biophysical and life science applications*; Wiley-VCH Verlag: Weinheim Germany, 2011.
- (110) Link, S.; Mohamed, M. B.; El-Sayed, M. A. Simulation of the Optical Absorption Spectra of Gold Nanorods as a Function of Their Aspect Ratio and the Effect of the Medium Dielectric Constant. *J. Phys. Chem. B* **1999**, *103*, 3073–3077.
- (111) Jain, P. K.; El-Sayed, M. A. Plasmonic coupling in noble metal nanostructures. *Chemical Physics Letters* **2010**, *487*, 153–164.
- (112) Lakowicz, J. R. Radiative decay engineering: Biophysical and biomedical applications. *Anal Biochem* **2001**, *298*, 1–24.
- (113) RAMAN, C. V.; KRISHNAN, K. S. A New Type of Secondary Radiation. *Nature* **1928**, *121*, 501–502.
- (114) Larkin, P. J. *Infrared and Raman spectroscopy: Principles and spectral interpretation*; Elsevier: Amsterdam, 2011.
- (115) Kneipp, J.; Kneipp, H.; Kneipp, K. SERS--a single-molecule and nanoscale tool for bioanalytics. *Chem Soc Rev* **2008**, *37*, 1052–1060.
- (116) Fleischmann, M.; Hendra, P. J.; McQuillan, A. J. Raman spectra of pyridine adsorbed at a silver electrode. *Chemical Physics Letters* **1974**, *26*, 163–166.
- (117) Geddes, C. D.; Lakowicz, J. R. *Radiative Decay Engineering*; Springer US: Boston, MA, 2005.
- (118) Chance, R. R.; Miller, A. H.; Prock, A.; Silbey, R. Fluorescence and energy transfer near interfaces: The complete and quantitative description of the Eu +3 /mirror systems. *The Journal of Chemical Physics* **1975**, *63*, 1589–1595.
- (119) Yun, C. S.; Javier, A.; Jennings, T.; Fisher, M.; Hira, S.; Peterson, S.; Hopkins, B.; Reich, N. O.; Strouse, G. F. Nanometal surface energy transfer in optical rulers, breaking the FRET barrier. *J Am Chem Soc* **2005**, *127*, 3115–3119.
- (120) Gabudean, A. M.; Focsan, M.; Astilean, S. Gold Nanorods Performing as Dual-Modal Nanoprobes via Metal-Enhanced Fluorescence (MEF) and Surface-Enhanced Raman Scattering (SERS). *J. Phys. Chem. C* **2012**, *116*, 12240–12249.
- (121) Khatua, S.; Paulo, P. M. R.; Yuan, H.; Gupta, A.; Zijlstra, P.; Orrit, M. Resonant plasmonic enhancement of single-molecule fluorescence by individual gold nanorods. *ACS Nano* **2014**, *8*, 4440–4449.
- (122) Cecconello, A.; Lu, C.-H.; Elbaz, J.; Willner, I. Au nanoparticle/DNA rotaxane hybrid nanostructures exhibiting switchable fluorescence properties. *Nano Lett* **2013**, *13*, 6275–6280.
- (123) Singh, A. K.; Khan, S. A.; Fan, Z.; Demeritte, T.; Senapati, D.; Kanchanapally, R.; Ray, P. C. Development of a long-range surface-enhanced Raman spectroscopy ruler. *J Am Chem Soc* **2012**, *134*, 8662–8669.
- (124) Fu, B.; Flynn, J. D.; Isaacoff, B. P.; Rowland, D. J.; Biteen, J. S. Super-Resolving the Distance-Dependent Plasmon-Enhanced Fluorescence of Single Dye and Fluorescent Protein Molecules. *J. Phys. Chem. C* **2015**, *119*, 19350–19358.

- (125) Chhabra, R.; Sharma, J.; Wang, H.; Zou, S.; Lin, S.; Yan, H.; Lindsay, S.; Liu, Y. Distance-dependent interactions between gold nanoparticles and fluorescent molecules with DNA as tunable spacers. *Nanotechnology* **2009**, *20*, 485201.
- (126) Pal, S.; Dutta, P.; Wang, H.; Deng, Z.; Zou, S.; Yan, H.; Liu, Y. Quantum Efficiency Modification of Organic Fluorophores Using Gold Nanoparticles on DNA Origami Scaffolds. *J. Phys. Chem. C* **2013**, *117*, 12735–12744.
- (127) Su, L.; Yuan, H.; Lu, G.; Rocha, S.; Orrit, M.; Hofkens, J.; Uji-i, H. Super-resolution Localization and Defocused Fluorescence Microscopy on Resonantly Coupled Single-Molecule, Single-Nanorod Hybrids. *ACS Nano* **2016**, *10*, 2455–2466.
- (128) Lessard-Viger, M.; Rioux, M.; Rainville, L.; Boudreau, D. FRET enhancement in multilayer core-shell nanoparticles. *Nano Lett* **2009**, *9*, 3066–3071.
- (129) Busson, M. P.; Rolly, B.; Stout, B.; Bonod, N.; Bidault, S. Accelerated single photon emission from dye molecule-driven nanoantennas assembled on DNA. *Nat Commun* **2012**, *3*, 962.
- (130) Mirkin, C. A.; Letsinger, R. L.; Mucic, R. C.; Storhoff, J. J. A DNA-based method for rationally assembling nanoparticles into macroscopic materials. *Nature* **1996**, *382*, 607–609.
- (131) Alivisatos, A. P.; Johnsson, K. P.; Peng, X.; Wilson, T. E.; Loweth, C. J.; Bruchez, M. P.; Schultz, P. G. Organization of 'nanocrystal molecules' using DNA. *Nature* **1996**, *382*, 609–611.
- (132) Lee, J.-S.; Lytton-Jean, A. K. R.; Hurst, S. J.; Mirkin, C. A. Silver nanoparticle-oligonucleotide conjugates based on DNA with triple cyclic disulfide moieties. *Nano Lett* **2007**, *7*, 2112–2115.
- (133) Zhang, X.; Servos, M. R.; Liu, J. Fast pH-assisted functionalization of silver nanoparticles with monothiolated DNA. *Chem Commun (Camb)* **2012**, *48*, 10114–10116.
- (134) Vietz, C.; Lalkens, B.; Acuna, G. P.; Tinnefeld, P. Functionalizing large nanoparticles for small gaps in dimer nanoantennas. *New J. Phys.* **2016**, *18*, 45012.
- (135) Huang, Y.-F.; Chang, H.-T.; Tan, W. Cancer cell targeting using multiple aptamers conjugated on nanorods. *Anal Chem* **2008**, *80*, 567–572.
- (136) Shi, D.; Song, C.; Jiang, Q.; Wang, Z.-G.; Ding, B. A facile and efficient method to modify gold nanorods with thiolated DNA at a low pH value. *Chem Commun (Camb)* **2013**, *49*, 2533–2535.
- (137) Li, J.; Zhu, B.; Zhu, Z.; Zhang, Y.; Yao, X.; Tu, S.; Liu, R.; Jia, S.; Yang, C. J. Simple and Rapid Functionalization of Gold Nanorods with Oligonucleotides Using an mPEG-SH/Tween 20-Assisted Approach. *Langmuir* **2015**, *31*, 7869–7876.
- (138) Jones, M. R.; Macfarlane, R. J.; Lee, B.; Zhang, J.; Young, K. L.; Senesi, A. J.; Mirkin, C. A. DNA-nanoparticle superlattices formed from anisotropic building blocks. *Nat Mater* **2010**, *9*, 913–917.
- (139) Elghanian, R.; Storhoff, J. J.; Mucic, R. C.; Letsinger, R. L.; Mirkin, C. A. Selective Colorimetric Detection of Polynucleotides Based on the Distance-Dependent Optical Properties of Gold Nanoparticles. *Science* **1997**, *277*, 1078–1081.
- (140) Zhang, X.; Servos, M. R.; Liu, J. Instantaneous and quantitative functionalization of gold nanoparticles with thiolated DNA using a pH-assisted and surfactant-free route. *J Am Chem Soc* **2012**, *134*, 7266–7269.
- (141) Pakiari, A. H.; Jamshidi, Z. Nature and strength of M-S bonds (m = Au, Ag, and Cu) in binary alloy gold clusters. *J Phys Chem A* **2010**, *114*, 9212–9221.
- (142) Cao, Jin, R.; Mirkin, C. A. DNA-Modified Core-Shell Ag/Au Nanoparticles. *J Am Chem Soc* **2001**, *123*, 7961–7962.
- (143) Fujita, M.; Katafuchi, Y.; Ito, K.; Kanayama, N.; Takarada, T.; Maeda, M. Structural study on gold nanoparticle functionalized with DNA and its non-cross-linking aggregation. *J Colloid Interface Sci* **2012**, *368*, 629–635.
- (144) Gómez-Graña, S.; Hubert, F.; Testard, F.; Guerrero-Martínez, A.; Grillo, I.; Liz-Marzán, L. M.; Spalla, O. Surfactant (bi)layers on gold nanorods. *Langmuir* **2012**, *28*, 1453–1459.
- (145) Perez-Juste, J.; Pastozia-Santos, I.; Liz-Marzán, L.; Mulvaney, P. Gold nanorods: Synthesis, characterization and applications. *Coordination Chemistry Reviews* **2005**, *249*, 1870–1901.

- (146) Pal, S.; Deng, Z.; Wang, H.; Zou, S.; Liu, Y.; Yan, H. DNA directed self-assembly of anisotropic plasmonic nanostructures. *J Am Chem Soc* **2011**, *133*, 17606–17609.
- (147) Wijaya, A.; Hamad-Schifferli, K. Ligand customization and DNA functionalization of gold nanorods via round-trip phase transfer ligand exchange. *Langmuir* **2008**, *24*, 9966–9969.
- (148) Gole, A.; Murphy, C. J. Biotin-streptavidin-induced aggregation of gold nanorods: Tuning rod-rod orientation. *Langmuir* **2005**, *21*, 10756–10762.
- (149) John, C. L.; Strating, S. L.; Shephard, K. A.; Zhao, J. X. Reproducibly synthesize gold nanorods and maintain their stability. *RSC Adv.* **2013**, *3*, 10909.
- (150) Caswell, K. K.; Wilson, J. N.; Bunz, U. H. F.; Murphy, C. J. Preferential end-to-end assembly of gold nanorods by biotin-streptavidin connectors. *J Am Chem Soc* **2003**, *125*, 13914–13915.
- (151) Wang, Z. L.; Mohamed, M. B.; Link, S.; El-Sayed, M. A. Crystallographic facets and shapes of gold nanorods of different aspect ratios. *Surface Science* **1999**, *440*, L809-L814.
- (152) Chang, J.-Y.; Wu, H.; Chen, H.; Ling, Y.-C.; Tan, W. Oriented assembly of Au nanorods using biorecognition system. *Chem Commun (Camb)* **2005**, 1092–1094.
- (153) Thomas, K. G.; Barazzouk, S.; Ipe, B. I.; Joseph, S. T. S.; Kamat, P. V. Uniaxial Plasmon Coupling through Longitudinal Self-Assembly of Gold Nanorods. *J. Phys. Chem. B* **2004**, *108*, 13066–13068.
- (154) Hurst, S. J.; Lytton-Jean, A. K. R.; Mirkin, C. A. Maximizing DNA loading on a range of gold nanoparticle sizes. *Anal Chem* **2006**, *78*, 8313–8318.
- (155) Kimura-Suda, H.; Petrovykh, D. Y.; Tarlov, M. J.; Whitman, L. J. Base-dependent competitive adsorption of single-stranded DNA on gold. *J Am Chem Soc* **2003**, *125*, 9014–9015.
- (156) Tokareva, I.; Hutter, E. Hybridization of oligonucleotide-modified silver and gold nanoparticles in aqueous dispersions and on gold films. *J Am Chem Soc* **2004**, *126*, 15784–15789.
- (157) Vietz, C.; Kaminska, I.; Sanz Paz, M.; Tinnefeld, P.; Acuna, G. P. Broadband Fluorescence Enhancement with Self-Assembled Silver Nanoparticle Optical Antennas. *ACS Nano* **2017**, *11*, 4969–4975.
- (158) Urban, M. J.; Zhou, C.; Duan, X.; Liu, N. Optically Resolving the Dynamic Walking of a Plasmonic Walker Couple. *Nano Lett* **2015**, *15*, 8392–8396.
- (159) Gür, F. N.; Schwarz, F. W.; Ye, J.; Diez, S.; Schmidt, T. L. Toward Self-Assembled Plasmonic Devices: High-Yield Arrangement of Gold Nanoparticles on DNA Origami Templates. *ACS Nano* **2016**, *10*, 5374–5382.
- (160) Vogele, K.; List, J.; Pardatscher, G.; Holland, N. B.; Simmel, F. C.; Pirzer, T. Self-Assembled Active Plasmonic Waveguide with a Peptide-Based Thermomechanical Switch. *ACS Nano* **2016**, *10*, 11377–11384.
- (161) Kuzyk, A.; Jungmann, R.; Acuna, G. P.; Liu, N. DNA Origami Route for Nanophotonics. *ACS Photonics* **2018**, *5*, 1151–1163.
- (162) Schmied, J. J.; Gietl, A.; Holzmeister, P.; Forthmann, C.; Steinhauer, C.; Dammeyer, T.; Tinnefeld, P. Fluorescence and super-resolution standards based on DNA origami. *Nat Methods* **2012**, *9*, 1133–1134.
- (163) Gallizia, A.; Lalla, C. de; Nardone, E.; Santambrogio, P.; Brandazza, A.; Sidoli, A.; Arosio, P. Production of a soluble and functional recombinant streptavidin in Escherichia coli. *Protein Expr Purif* **1998**, *14*, 192–196.
- (164) Nikoobakht, B.; El-Sayed, M. A. Preparation and Growth Mechanism of Gold Nanorods (NRs) Using Seed-Mediated Growth Method. *Chem. Mater.* **2003**, *15*, 1957–1962.
- (165) Lin, Z.; Cai, J. J.; Scriven, L. E.; Davis, H. T. Spherical-to-Wormlike Micelle Transition in CTAB Solutions. *J. Phys. Chem.* **1994**, *98*, 5984–5993.
- (166) Walsh, M. J.; Barrow, S. J.; Tong, W.; Funston, A. M.; Etheridge, J. Symmetry breaking and silver in gold nanorod growth. *ACS Nano* **2015**, *9*, 715–724.
- (167) Miranda, O. R.; Dollahon, N. R.; Ahmadi, T. S. Critical Concentrations and Role of Ascorbic Acid (Vitamin C) in the Crystallization of Gold Nanorods within Hexadecyltrimethyl Ammonium Bromide

- (CTAB)/Tetraoctyl Ammonium Bromide (TOAB) Micelles. *Crystal Growth & Design* **2006**, *6*, 2747–2753.
- (168) Smith, D. K.; Korgel, B. A. The importance of the CTAB surfactant on the colloidal seed-mediated synthesis of gold nanorods. *Langmuir* **2008**, *24*, 644–649.
- (169) Smith, D. K.; Miller, N. R.; Korgel, B. A. Iodide in CTAB prevents gold nanorod formation. *Langmuir* **2009**, *25*, 9518–9524.
- (170) Alekseeva, A. V.; Bogatyrev, V. A.; Khlebtsov, B. N.; Mel'nikov, A. G.; Dykman, L. A.; Khlebtsov, N. G. Gold nanorods: Synthesis and optical properties. *Colloid J* **2006**, *68*, 661–678.
- (171) Haiss, W.; Thanh, N. T. K.; Aveyard, J.; Fernig, D. G. Determination of size and concentration of gold nanoparticles from UV-vis spectra. *Anal Chem* **2007**, *79*, 4215–4221.
- (172) Scarabelli, L.; Sánchez-Iglesias, A.; Pérez-Juste, J.; Liz-Marzán, L. M. A "Tips and Tricks" Practical Guide to the Synthesis of Gold Nanorods. *J Phys Chem Lett* **2015**, *6*, 4270–4279.
- (173) Sellers, H.; Ulman, A.; Shnidman, Y.; Eilers, J. E. Structure and binding of alkanethiolates on gold and silver surfaces: Implications for self-assembled monolayers. *J. Am. Chem. Soc.* **1993**, *115*, 9389–9401.
- (174) Orendorff, C. J.; Murphy, C. J. Quantitation of metal content in the silver-assisted growth of gold nanorods. *J Phys Chem B* **2006**, *110*, 3990–3994.
- (175) Liu, X.; Atwater, M.; Wang, J.; Huo, Q. Extinction coefficient of gold nanoparticles with different sizes and different capping ligands. *Colloids Surf B Biointerfaces* **2007**, *58*, 3–7.
- (176) Paramelle, D.; Sadovoy, A.; Gorelik, S.; Free, P.; Hobley, J.; Fernig, D. G. A rapid method to estimate the concentration of citrate capped silver nanoparticles from UV-visible light spectra. *Analyst* **2014**, *139*, 4855–4861.
- (177) Choi, Y.; Kotthoff, L.; Olejko, L.; Resch-Genger, U.; Bald, I. DNA Origami-Based Förster Resonance Energy-Transfer Nanoarrays and Their Application as Ratiometric Sensors. *ACS Appl Mater Interfaces* **2018**, *10*, 23295–23302.
- (178) Olejko, L.; Cywiński, P. J.; Bald, I. An ion-controlled four-color fluorescent telomeric switch on DNA origami structures. *Nanoscale* **2016**, *8*, 10339–10347.
- (179) Snyder, B.; Freire, E. Fluorescence energy transfer in two dimensions. A numeric solution for random and nonrandom distributions. *Biophysical Journal* **1982**, *40*, 137–148.
- (180) Berney, C.; Danuser, G. FRET or No FRET: A Quantitative Comparison. *Biophysical Journal* **2003**, *84*, 3992–4010.
- (181) Corry, B.; Jayatilaka, D.; Rigby, P. A flexible approach to the calculation of resonance energy transfer efficiency between multiple donors and acceptors in complex geometries. *Biophysical Journal* **2005**, *89*, 3822–3836.
- (182) Casey, J. R.; Grinstein, S.; Orłowski, J. Sensors and regulators of intracellular pH. *Nat Rev Mol Cell Biol* **2010**, *11*, 50–61.
- (183) Riter, R. E.; Undiks, E. P.; Levinger, N. E. Impact of Counterion on Water Motion in Aerosol OT Reverse Micelles. *J. Am. Chem. Soc.* **1998**, *120*, 6062–6067.
- (184) Schäferling, M. Nanoparticle-based luminescent probes for intracellular sensing and imaging of pH. *Wiley Interdiscip Rev Nanomed Nanobiotechnol* **2016**, *8*, 378–413.
- (185) Martin, M. M.; Lindqvist, L. The pH dependence of fluorescein fluorescence. *Journal of Luminescence* **1975**, *10*, 381–390.
- (186) Sjöback, R.; Nygren, J.; Kubista, M. Absorption and fluorescence properties of fluorescein. *Spectrochimica Acta Part A: Molecular and Biomolecular Spectroscopy* **1995**, *51*, L7-L21.
- (187) Pant, D.; Le Guennec, M.; Illien, B.; Girault, H. H. The pH dependent adsorption of Coumarin 343 at the water/dichloroethane interface. *Phys. Chem. Chem. Phys.* **2004**, *6*, 3140.
- (188) Hong, S. W.; Jo, W. H. A fluorescence resonance energy transfer probe for sensing pH in aqueous solution. *Polymer* **2008**, *49*, 4180–4187.

- (189) Fitzhugh, O. G.; Nelson, A. A. Liver Tumors in Rats Fed Thiourea or Thioacetamide. *Science* **1948**, *108*, 626–628.
- (190) Sauer, M.; Hofkens, J.; Enderlein, J. *Handbook of Fluorescence Spectroscopy and Imaging*; Wiley-VCH Verlag GmbH & Co. KGaA: Weinheim, Germany, 2011.
- (191) Rehm, D.; Weller, A. Kinetics of Fluorescence Quenching by Electron and H-Atom Transfer. *Isr. J. Chem.* **1970**, *8*, 259–271.
- (192) Hara, K.; Sato, T.; Katoh, R.; Furube, A.; Ohga, Y.; Shinpo, A.; Suga, S.; Sayama, K.; Sugihara, H.; Arakawa, H. Molecular Design of Coumarin Dyes for Efficient Dye-Sensitized Solar Cells. *J. Phys. Chem. B* **2003**, *107*, 597–606.
- (193) Morandeira, A.; Boschloo, G.; Hagfeldt, A.; Hammarström, L. Coumarin 343–NiO Films as Nanostructured Photocathodes in Dye-Sensitized Solar Cells: Ultrafast Electron Transfer, Effect of the I<sup>3</sup>–/I<sup>–</sup> Redox Couple and Mechanism of Photocurrent Generation. *J. Phys. Chem. C* **2008**, *112*, 9530–9537.
- (194) Hanson, K. M.; Behne, M. J.; Barry, N. P.; Mauro, T. M.; Gratton, E.; Clegg, R. M. Two-Photon Fluorescence Lifetime Imaging of the Skin Stratum Corneum pH Gradient. *Biophysical Journal* **2002**, *83*, 1682–1690.
- (195) Zhang, X.; Xiao, Y.; Qian, X. A ratiometric fluorescent probe based on FRET for imaging Hg<sup>2+</sup> ions in living cells. *Angew Chem Int Ed Engl* **2008**, *47*, 8025–8029.
- (196) Sauer, E.; Reinke, A.-K.; Courts, C. Differentiation of five body fluids from forensic samples by expression analysis of four microRNAs using quantitative PCR. *Forensic Sci Int Genet* **2016**, *22*, 89–99.
- (197) Biscontin, A.; Casara, S.; Cagnin, S.; Tombolan, L.; Rosolen, A.; Lanfranchi, G.; Pittà, C. de. New miRNA labeling method for bead-based quantification. *BMC Mol Biol* **2010**, *11*, 44.
- (198) Currie, L. Detection and quantification limits: Origins and historical overview. *Anal Chim Acta* **1999**, *391*, 127–134.
- (199) Gong, P.; Levicky, R. DNA surface hybridization regimes. *Proc Natl Acad Sci U S A* **2008**, *105*, 5301–5306.
- (200) SantaLucia, J. A unified view of polymer, dumbbell, and oligonucleotide DNA nearest-neighbor thermodynamics. *Proceedings of the National Academy of Sciences* **1998**, *95*, 1460–1465.
- (201) Bidault, S.; Abajo, F. J. G. d.; Polman, A. Plasmon-based nanolenses assembled on a well-defined DNA template. *J Am Chem Soc* **2008**, *130*, 2750–2751.
- (202) Lee, H. M.; Jin, S. M.; Kim, H. M.; Suh, Y. D. Single-molecule surface-enhanced Raman spectroscopy: A perspective on the current status. *Phys Chem Chem Phys* **2013**, *15*, 5276–5287.
- (203) Yamakoshi, H.; Dodo, K.; Palonpon, A.; Ando, J.; Fujita, K.; Kawata, S.; Sodeoka, M. Alkyne-tag Raman imaging for visualization of mobile small molecules in live cells. *J Am Chem Soc* **2012**, *134*, 20681–20689.
- (204) Barhoumi, A.; Zhang, D.; Tam, F.; Halas, N. J. Surface-enhanced Raman spectroscopy of DNA. *J Am Chem Soc* **2008**, *130*, 5523–5529.
- (205) Hong, S.; Li, X. Optimal Size of Gold Nanoparticles for Surface-Enhanced Raman Spectroscopy under Different Conditions. *Journal of Nanomaterials* **2013**, *2013*, 1–9.
- (206) Orendorff, C. J.; Gearheart, L.; Jana, N. R.; Murphy, C. J. Aspect ratio dependence on surface enhanced Raman scattering using silver and gold nanorod substrates. *Phys Chem Chem Phys* **2006**, *8*, 165–170.
- (207) Dhawan, A.; Norton, S. J.; Gerhold, M. D.; Vo-Dinh, T. Comparison of FDTD numerical computations and analytical multipole expansion method for plasmonics-active nanosphere dimers. *Opt. Express* **2009**, *17*, 9688.
- (208) Sendroiu, I. E.; Warner, M. E.; Corn, R. M. Fabrication of silica-coated gold nanorods functionalized with DNA for enhanced surface plasmon resonance imaging biosensing applications. *Langmuir* **2009**, *25*, 11282–11284.

- (209) Sharma, V.; Park, K.; Srinivasarao, M. Shape separation of gold nanorods using centrifugation. *Proc Natl Acad Sci U S A* **2009**, *106*, 4981–4985.
- (210) Akbulut, O.; Mace, C. R.; Martinez, R. V.; Kumar, A. A.; Nie, Z.; Patton, M. R.; Whitesides, G. M. Separation of nanoparticles in aqueous multiphase systems through centrifugation. *Nano Lett* **2012**, *12*, 4060–4064.
- (211) Park, K.; Koerner, H.; Vaia, R. A. Depletion-induced shape and size selection of gold nanoparticles. *Nano Lett* **2010**, *10*, 1433–1439.
- (212) Fu, Y.; Zhang, J.; Lakowicz, J. R. Plasmon-enhanced fluorescence from single fluorophores end-linked to gold nanorods. *J Am Chem Soc* **2010**, *132*, 5540–5541.
- (213) Yu, H.; Fu, M.; Xiao, Y. Switching off FRET by analyte-induced decomposition of squaraine energy acceptor: A concept to transform 'turn off' chemodosimeter into ratiometric sensors. *Phys Chem Chem Phys* **2010**, *12*, 7386–7391.
- (214) Jiang, Q.; Song, C.; Nangreave, J.; Liu, X.; Lin, L.; Qiu, D.; Wang, Z.-G.; Zou, G.; Liang, X.; Yan, H.; Ding, B. DNA origami as a carrier for circumvention of drug resistance. *J Am Chem Soc* **2012**, *134*, 13396–13403.
- (215) Walsh, A. S.; Yin, H.; Erben, C. M.; Wood, M. J. A.; Turberfield, A. J. DNA cage delivery to mammalian cells. *ACS Nano* **2011**, *5*, 5427–5432.
- (216) Zhao, Y.-X.; Shaw, A.; Zeng, X.; Benson, E.; Nyström, A. M.; Högberg, B. DNA origami delivery system for cancer therapy with tunable release properties. *ACS Nano* **2012**, *6*, 8684–8691.
- (217) Liu, X.; Bing, T.; Shangguan, D. Microbead-Based Platform for Multiplex Detection of DNA and Protein. *ACS Appl Mater Interfaces* **2017**, *9*, 9462–9469.
- (218) Zuo, X.; Yang, X.; Wang, K.; Tan, W.; Wen, J. A novel sandwich assay with molecular beacon as report probe for nucleic acids detection on one-dimensional microfluidic beads array. *Anal Chim Acta* **2007**, *587*, 9–13.
- (219) Linko, V.; Dietz, H. The enabled state of DNA nanotechnology. *Curr Opin Biotechnol* **2013**, *24*, 555–561.
- (220) Selnihhin, D.; Sparvath, S. M.; Preus, S.; Birkedal, V.; Andersen, E. S. Multifluorophore DNA Origami Beacon as a Biosensing Platform. *ACS Nano* **2018**, DOI: 10.1021/acsnano.8b01510.
- (221) Egholm, M.; Buchardt, O.; Christensen, L.; Behrens, C.; Freier, S. M.; Driver, D. A.; Berg, R. H.; Kim, S. K.; Norden, B.; Nielsen, P. E. PNA hybridizes to complementary oligonucleotides obeying the Watson-Crick hydrogen-bonding rules. *Nature* **1993**, *365*, 566–568.
- (222) Singh, S. K.; Koshkin, A. A.; Wengel, J.; Nielsen, P. LNA (locked nucleic acids): Synthesis and high-affinity nucleic acid recognition. *Chem. Commun.* **1998**, 455–456.
- (223) Billaud, P.; Marhaba, S.; Cottancin, E.; Arnaud, L.; Bachelier, G.; Bonnet, C.; Del Fatti, N.; Lermé, J.; Vallée, F.; Vialle, J.-L.; Broyer, M.; Pellarin, M. Correlation between the Extinction Spectrum of a Single Metal Nanoparticle and Its Electron Microscopy Image. *J. Phys. Chem. C* **2008**, *112*, 978–982.



# Appendix

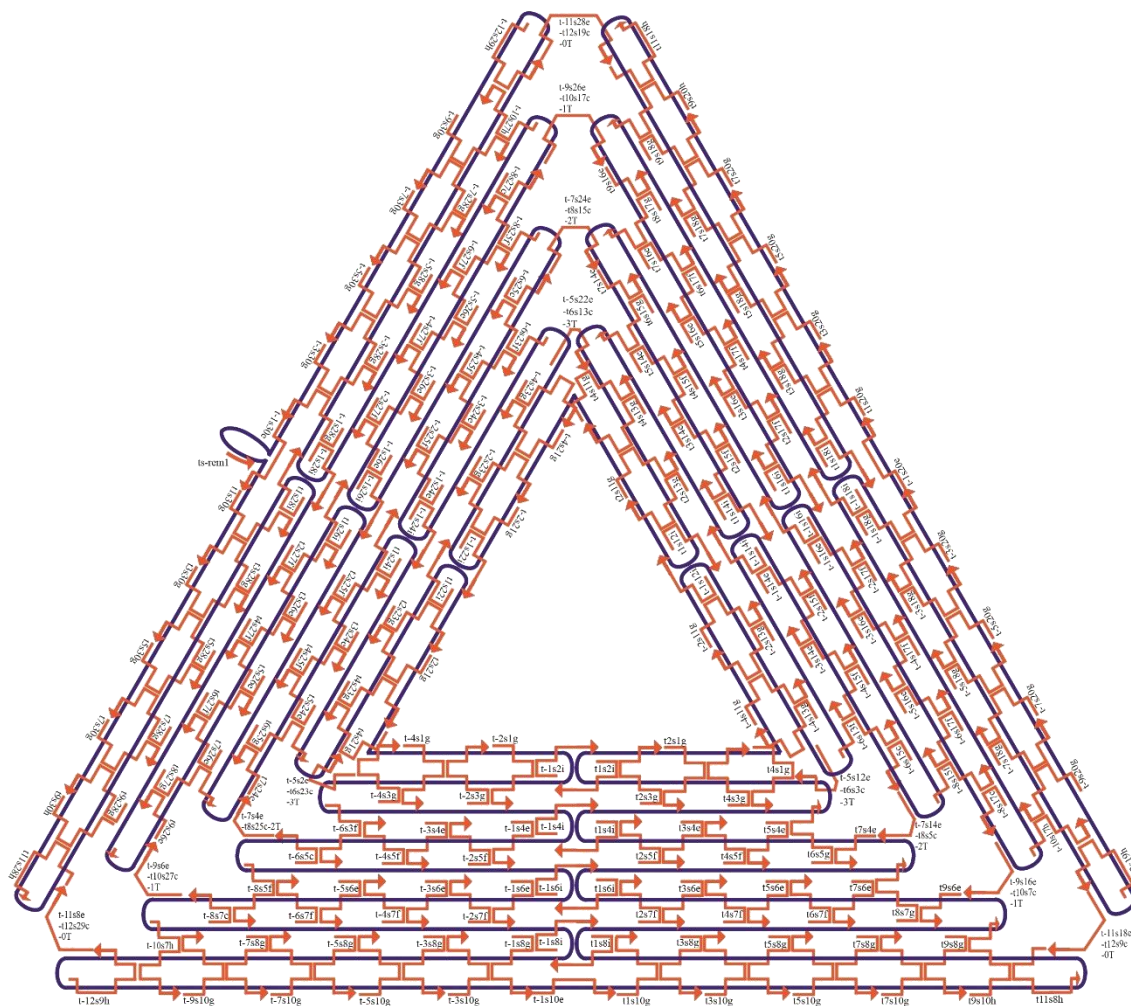


**Figure A.1.:** A triangular DNA origami nanostructure staple map, used throughout this work. Scaffold strand: dark blue, staple strands: red. This staple map was created by Dr. Christian Heck.

**Table A.1.:** Elongated staple strand for FRET nanoarray analysis for each array (Donor : FAM-(ATT)<sub>7</sub>, Acceptor: Cy3-(TTG)<sub>7</sub>).

<b>Nanoarray</b>	<b>Donor capture</b> (AAT) <sub>7</sub> -(staple)	<b>Acceptor capture</b> (CAA) <sub>7</sub> -(staple)
<b>(2x1)</b>	t-4s5f	t-4s3g
<b>(2x2)</b>	t-4s5f, t-3s4e	t-4s3g, t-3s6e
<b>(2x3)</b>	t-4s5f, t-3s4e, t-2s5f	t-4s3g, t-3s6e, t-2s3g
<b>(3x2)</b>	t-4s5f, t-3s4e, t-3s8g	t-4s3g, t-3s6e, t-4s7f
<b>(3x4)</b>	t-4s3g, t-3s6e, t-4s7f, t-2s3g, t-2s7f, t-1s6e	t-4s5f, t-3s4e, t-3s8g, t-2s5f, t-1s4e, t-1s8g

**Table A.2.:** List of staple strand for proof-of-concept pH ratiometric sensing for each array (Donor : C343-(TTG)<sub>7</sub>, Acceptor: FAM-(ATT)<sub>7</sub>).

<b>Nanoarray</b>	<b>Donor capture</b> (CAA) <sub>7</sub> -(staple)	<b>Acceptor capture</b> (AAT) <sub>7</sub> -(staple)
<b>(2x1)</b>	t-4s3g	t-4s5f
<b>2 x (2x1)</b>	t-4s3g, t-1s6e	t-4s5f, t-1s8g
<b>6 x (2x1)</b>	t-4s3g, t-4s13g, t-4s23g, t-3s4e, t-3s14e, t-3s24e	t-4s5f, t-4s15f, t-4s25f, t-3s6e, t-3s16e, t-3s26e
<b>(3x4)</b>	t-4s3g, t-3s6e, t-4s7f, t-2s3g, t-2s7f, t-1s6e	t-4s5f, t-3s4e, t-3s8g, t-2s5f, t-1s4e, t-1s8g

**Table A.3.:** Target oligonucleotide sequences and biotin modified target capture oligonucleotide sequences used for proof-of-concept multiplexing analysis for microbead-based assay. The target sequences were chosen based on human miRNA sequences that have been discovered and are being used as biomarkers in profiling (sequences are listed 5' -> 3').

<b>Target oligonucleotide</b>			
<b>Target</b>	<b>Corresponding miRNA</b>	<b>Target DNA sequence</b>	<b>Human miRNA sequence</b>
Target 1	has-miR-21	TAGCTTATCAGACTGATGTTGAA <sub>40</sub>	uagcuuauacagacugauguuga
Target 2	hsa-miR-106a-5p	AAAAGTGCTTACAGTGCAGGTAGA <sub>40</sub>	aaaagugcuuacagugcagguag
Target 3	hsa-miR-4484	AAAAGGCGGGAGAAGCCCCAA <sub>40</sub>	aaaaggcgggagaagcccca
Target 4	hsa-miR-15a-5p	TAGCAGCACATAATGGTTTGTGA <sub>40</sub>	uagcagcacauaaugguuugug
Target 5	hsa-miR-486-5p	TCCTGTAAGTACTGAGCTGCCCCGAGA <sub>40</sub>	uccuguacugagcugccccgag
<b>Target capture oligonucleotide</b>			
<b>Target capture</b>	<b>Capture DNA sequence</b>		<b>Spacer</b>
Capture-Target 1	TCAACATCAGTCTGATAAGCTA		(Capture)-HEGL-Biotin
Capture-Target 2	CTACCTGCACTGTAAGCACTTTT		
Capture-Target 3	TGGGGCTTCTCCCGCCTTTT		
Capture-Target 4	CACAAACCATTATGTGCTGCTA		
Capture-Target 5	CTCGGGGCAGCTCAGTACAGGA		

**Table A.4.:** List of staple strands for *DNA origami\_R* with different numbers of probe strands for each design.

<i>DNA origami_R</i>	<b>Probe strands</b> (staple)-T <sub>40</sub>	<b>Dye label handles</b> (AAT) <sub>7</sub> -(staple)
<b>4</b>	t-6s17f, t-2s17f, t 2s17f, t 6s17f	t-7s8g, t-5s8g, t-3s8g, t-1s8g, t-3s4e, t-1s4e, t 1s4i, t 1s8i, t 3s4e, t 3s8g, t 5s4e, t 5s8g, t 7s8g, t 9s8g
<b>4-2</b>	t-2s17f, t 2s17f, t-2s27f, t 2s27f,	
<b>6</b>	t-6s17f, t-4s15f, t-2s17f, t 6s17f, t 4s15f, t 2s17f	
<b>6-2</b>	t-6s17f, t-4s15f, t 2s17f, t-6s27f, t-2s27f, t 2s27f,	
<b>8</b>	t-6s17f, t-2s17f, t 2s17f, t 6s17f, t-6s27f, t-2s27f, t 2s27f, t 6s27f	
<b>10</b>	t-6s17f, t-2s17f, t 2s17f, t 4s15f, t 6s17f, t-6s27f, t-4s25f, t-2s27f, t 2s27f, t 6s27f	
<b>12</b>	t-6s17f, t-4s15f, t-2s17f, t 2s17f, t 4s15f, t 6s17f, t-6s27f, t-4s25f, t-2s27f, t 2s27f, t 4s25f, t 6s27f	

**Table A.5.:** List of staple strands for *DNA origami\_R* used as a strategy to signal amplification. Linker strand used here is ATG CAC GTA AGC CGA GTA TGG TTG ACC AAC ACC GGA AAA CTT TTC ACT TG (sequences are listed in 5' -> 3' direction).

	<b>Probe strands</b> (staple)-T <sub>40</sub>	<b>Linker capture 1</b> CAT ACT CGG CTT AACG TGC AT-(staple)	<b>Linker capture 2</b> (staple)-AAG GTA AAA GTT TTC CGG TGG TTG TCA AC
<i>DNA origami_R</i>	t-6s17f, t-2s17f, t 2s17f, t 6s17f	t 2s25f, t-3s26e, t5s26e, t-6s27f	
<i>Linker origami</i>	X	t 2s25f, t-3s26e, t5s26e, t-6s27f	t-2s17f, t 6s17f, t 3s14e, t-5s16e

**Table A.6.:** Staple strand list for capturing metal nanoparticles on the DNA origami nanostructure.

	<b>Capture strands (AAA)<sub>8</sub>T<sub>4</sub>-(staple)</b>	<b>Capture strands (ATT)<sub>7</sub>-(staple)</b>
<b>AuNR</b>	t-3s6e, t-3s8g, t-1s6e, t-1s8g and, (AAA) <sub>8</sub> -t-5s8g	t 1s6i, t 1s8i, t 3s6e, t 3s8g, t 5s6e, t 5s8g
<b>AuNP, AgNP</b>	t-2s5f, t-2s7f, t 2s5f, t 2s7f, t-1s6e, t-1s8g, t 1s6i, t 1s8i	<b>X</b>

### **Preparation of streptavidin coupled microbeads (conducted by Dr. Carsten Schmidt)<sup>1</sup>**

Briefly, 150000 fluorescence encoded carboxylated polymethylmethacrylate microbeads (PolyAn GmbH, Berlin, Germany) were activated with 25 mg mL<sup>-1</sup> N-(3-dimethylaminopropyl)-N'-ethylcarbodiimide hydrochloride (EDC, Sigma, St-Louis, MO, USA) dissolved in 0.1 M 2-(N-morpholino)ethanesulfonic acid buffer (pH 4.5) (MES, Sigma, St. Louis, MO, USA) for 30 min at 28 °C. After activation, excess EDC was removed by washing the microbeads with 200 µl diluted PBS (2.5 mM Na-phosphate pH 7.4, 7.5 mM NaCl). The activated microbeads were incubated in 50 µl of 150 µg/mL streptavidin dissolved in diluted PBS-buffer for 3 h at 28°C. Excessive streptavidin was removed with three washing steps using 200 µl TBST (50 mM Tris/HCl (pH 7.5), 154 mM NaCl, 0.01% Tween-20).

Streptavidin was generated recombinantly according to Gallizia et al<sup>2</sup>. Briefly, streptavidin was produced with *E. coli* (BL21DE3 pLys) transformed with a pET11a containing the streptavidin DNA. Cells were disrupted with french pressing, cell debris were removed by centrifugation, and the supernatant was incubated with 2-iminobiotin-sepharose (Sigma). The sepharose was washed extensively until the absorption at 260 nm reached the baseline level. Finally streptavidin was eluted in 1% acetic acid. By use of centrifugal filter units (Millipore), acetic acid was exchanged with diluted PBS and the solution was concentrated (1 mg/mL streptavidin). 200 µl of 100 nM biotinylated capture probe was given to 50000 streptavidin coupled microbeads. After incubation for 1 h at 37 °C, the microbeads were washed three times with 200 µl hybridization buffer (Hy-buffer: 67 mM Tris/HCl (pH 8,5), 16 mM (NH<sub>4</sub>)<sub>2</sub>SO<sub>4</sub>,

15 mM MgCl<sub>2</sub>, 0.01% Tween-20). For multiplexing analysis, different microbead populations presenting different capture probes on their surface were mixed together.

For hybridization analysis dilutions of target oligonucleotides with the desired concentrations were prepared by use of Hy-buffer. 100 µl were given to a microbead mixture containing approximately 100 microbeads per population. After one hour of incubation at 25 °C, excess oligonucleotides were removed by washing the microbeads three times with 200 µL Hy-buffer. The detection of hybridized oligonucleotides was done by resuspension of the microbeads in 10 µL of 2.5 nM Atto647N-labeled 40-nt Poly T oligonucleotide or 10 µL of 2.5 nM Atto647N-labeled DNA origami nanostructure in Hy-buffer. The incubation time was one hour at room temperature and then overnight at 4°C. For quantification of the surface fluorescence of each microbead population, the microbeads were transferred to a well of a 96-well-microtiter plate that had been filled with 150 µl PCR-buffer previously. After the microbeads had settled down to the transparent bottom of the well (10 min), the microbeads were analyzed with VideoScan-technology.

<sup>1</sup> Rödiger, S. et. al. *Anal. Chem.* 83 (2011) 3379–3385.

<sup>2</sup> Gallizia, A. et. al., *Protein. Expr. Purif.* 14 (1998) 192-196.

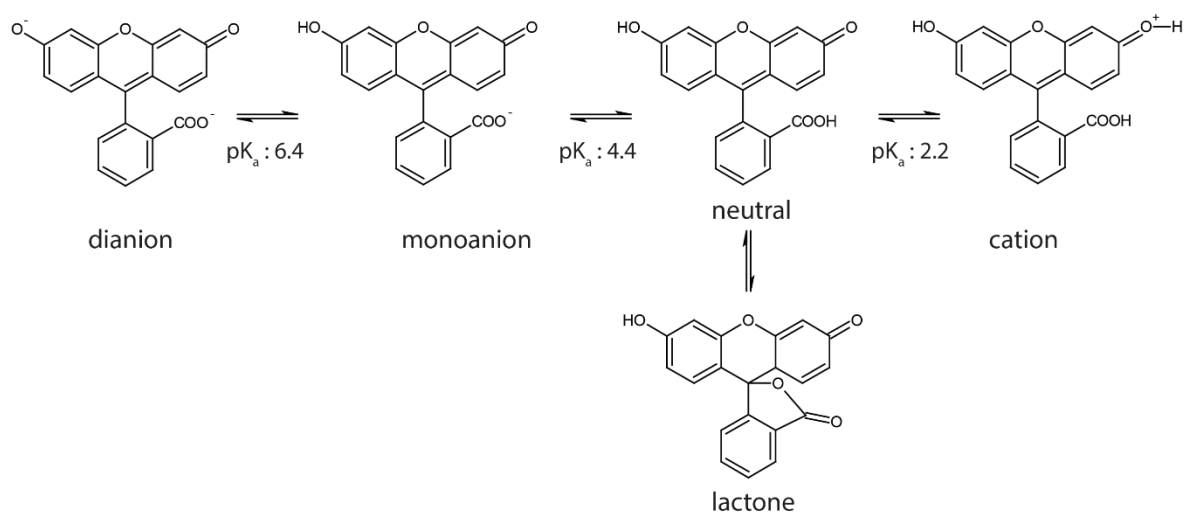


**Figure A.2.:** Fluorescein ionization equilibria. The different ground state structures lead to different absorption, and can be seen in the absorption spectra. Only the monoanion and dianion of fluorescein are fluorescent with the emission spectra dominated by the dianion with small contributions from the monoanion<sup>3</sup>.

<sup>3</sup> Matin, M. Lindqvist, L. The pH dependence of fluorescein fluorescence, J. Lumin. 1975 10 381-390  
113

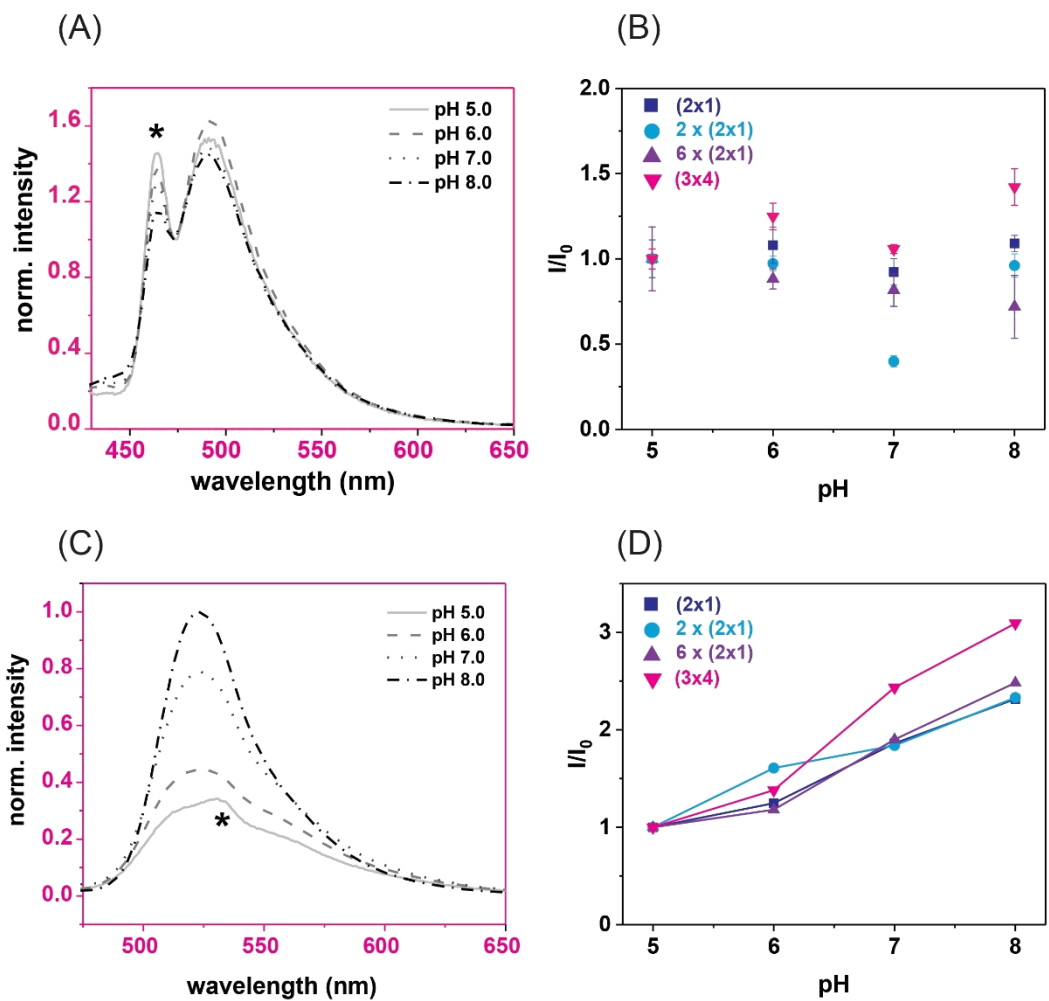


**Figure A.3.:** Normalized steady-state emission spectra C343 and FAM at different pH values. (A) C343 only (**3x4**) nanoarray at four different pH ( $\lambda_{exc} = 400$  nm). (B) Intensity ratio at 487 nm of all nanoarrays ( $I$  at given pH and  $I_0$  at pH 5), showing no trend in the change of emission. (C) FAM only (**3x4**) nanoarray at four different pH ( $\lambda_{exc} = 450$  nm). (D) Intensity ratio at 487 nm ( $I$  at given pH and  $I_0$  at pH 5), showing an increasing trend as the fluorescence is recovered at pH 8. Water Raman peaks are marked with an asterisk.



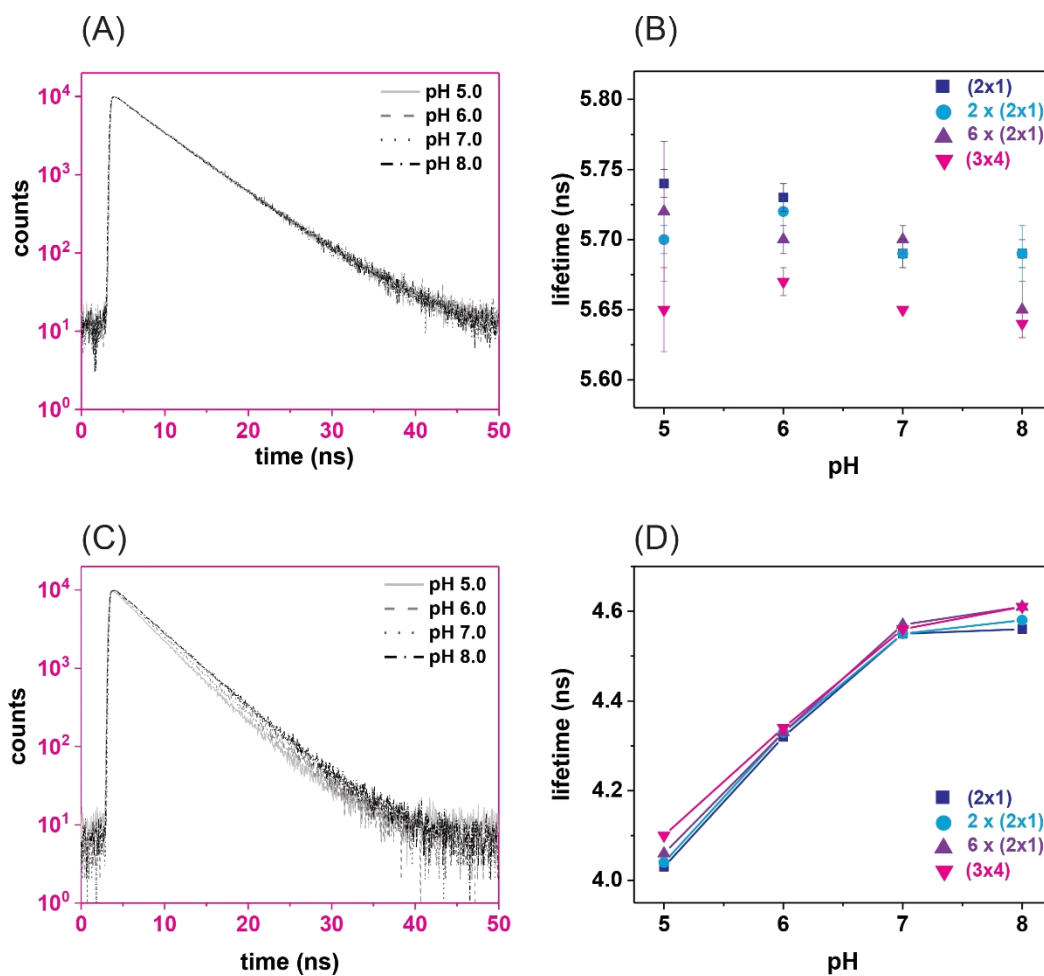


**Figure A.4.:** Fluorescence lifetime decay curves of C343 and FAM at different pH values. (A) C343 only **(3x4)** nanoarray at four different pH ( $\lambda_{exc} = 450 \text{ nm}$ ,  $\lambda'_{emi} = 490 \text{ nm}$ ). (B) Average fluorescence lifetimes of C343 for all nanoarrays showed no trend. (C) FAM only **(3x4)** nanoarray at four different pH ( $\lambda_{exc} = 490 \text{ nm}$ ,  $\lambda'_{emi} = 520 \text{ nm}$ ). (D) Average FAM fluorescence lifetime for all nanoarrays showed an increasing trend proportional to pH.

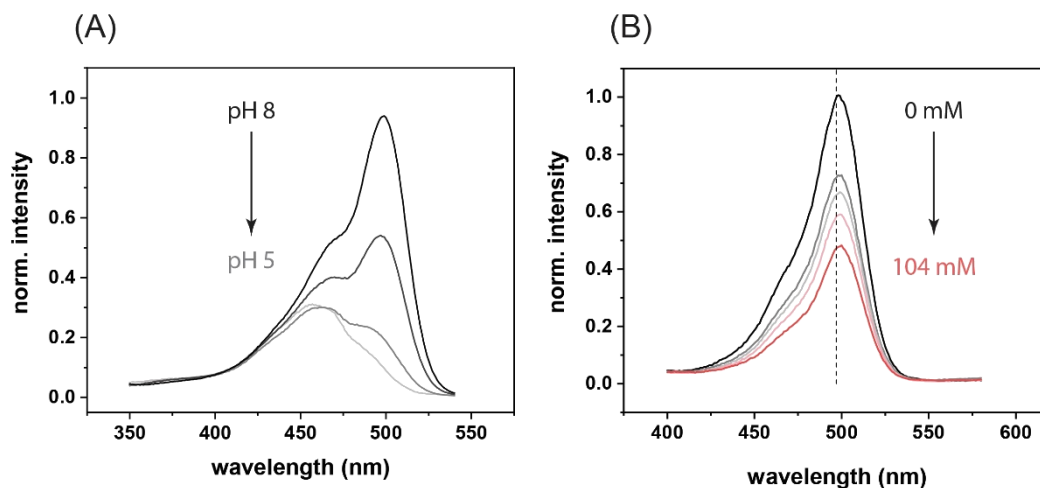


**Figure A.5.:** Excitation spectra of FAM only (3x4) array. (A) FAM excitation spectra ( $\lambda'_{exc} = 560$  nm). A clear profile change could be observed with the change in the pH of the solution. (B) FAM excitation spectra ( $\lambda'_{exc} = 600$  nm). The excitation spectra shape did not change its profile.

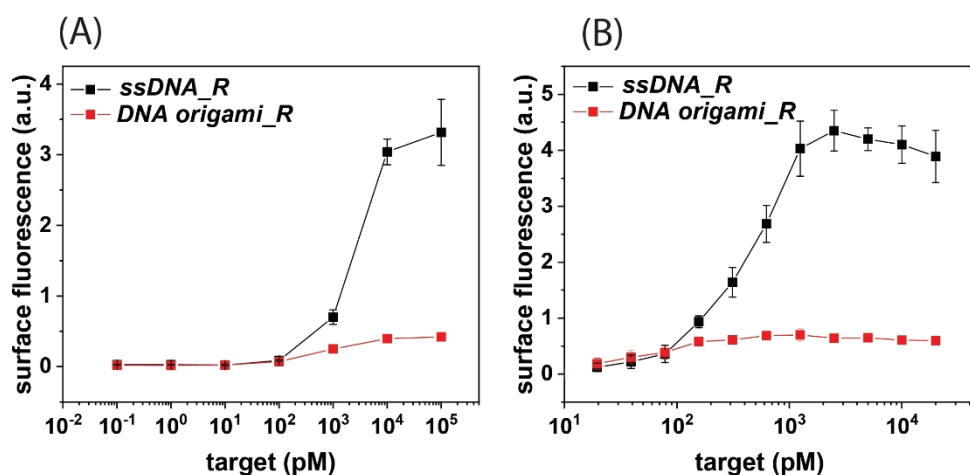


**Figure A.6.:** Surface fluorescence intensity of the microbead without normalization using both  $ssDNA\_R$  (black) and  $DNA\ origami\_R$  (red). (A) The fluorescence intensity using  $ssDNA\_R$  was approximately 10 fold higher than when using  $DNA\ origami\_R$ . (B) A concentration dependent response, at smaller concentration steps. The maximum intensity was reached before reaching 10 nM. This set of data was obtained two weeks after preparing the microbeads, showing a time dependent efficiency when using microbeads.

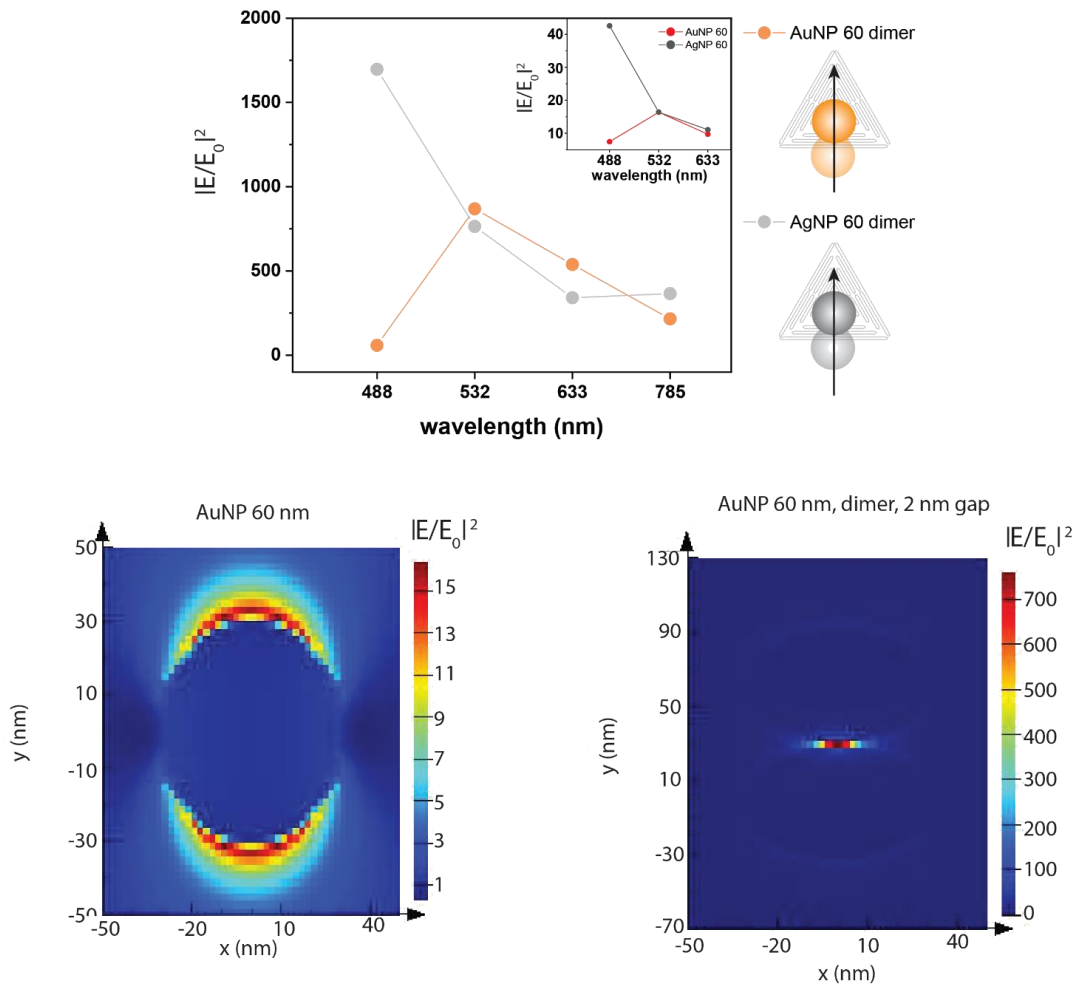


**Figure A.7.:** Electromagnetic field enhancement based on Finite difference time domain (FDTD) simulations at four different excitation wavelengths with excitation polarization along the y axis. Upper panel shows field enhancement at different excitation wavelengths with a 2 nm gap . Interestingly, AgNP shows a much higher enhancement at 488 nm. Illustration of the formed structure is shown on the right side, with black arrows indication the polarization of the excitation light. Bottom panel shows the simulation of 60nm AuNP with 2 nm gap on the left and 6 nm gap on the right. The field enhancement, as can be seen, is larger for the 2 nm gap ( $|E/E_0| = 869$ ) than the 6 nm gap ( $|E/E_0| = 548$ ).

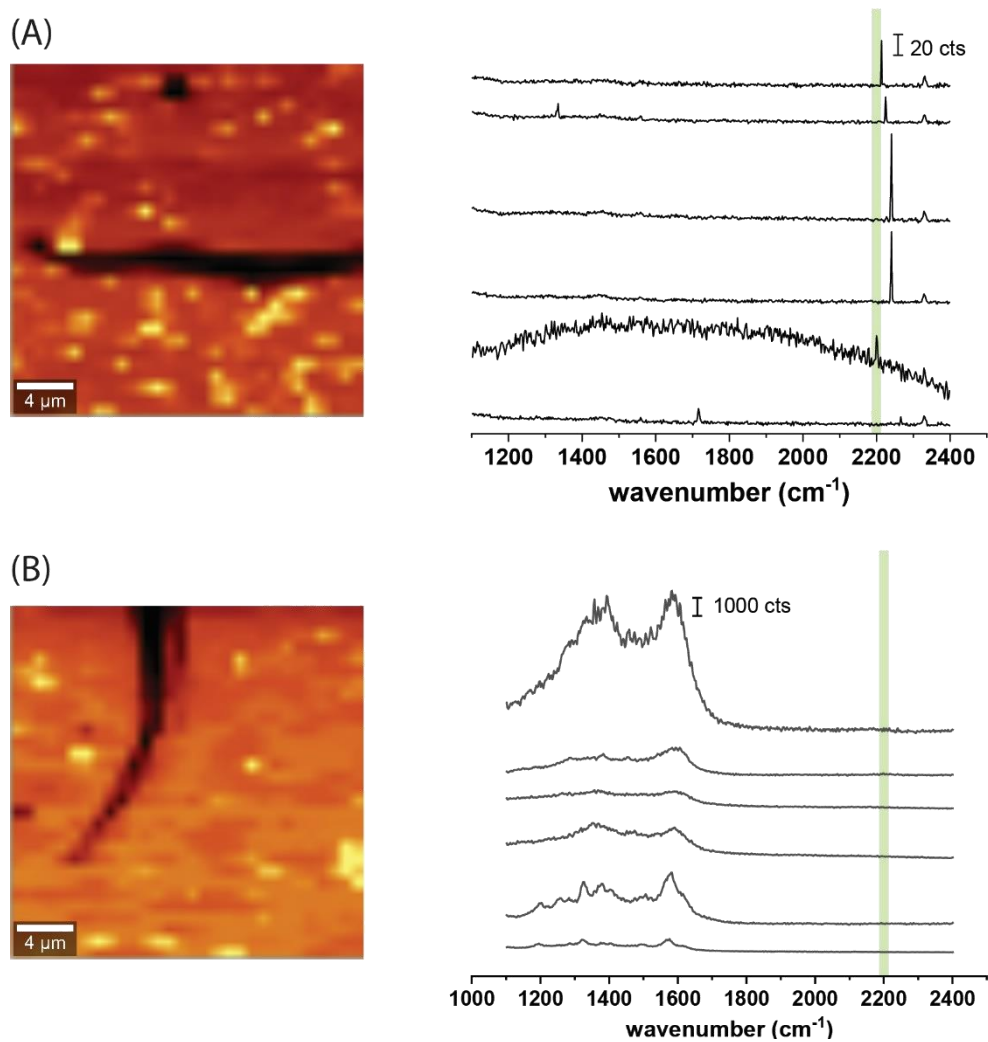


**Figure A.8.:** SERS spectra of SH-dT(PEPY) $T_3$ (TTT) $_8$ T $_3$ dT(PEPY)-SH coated nanoparticle dimers on DNA origami nanostructures. (A) Raman map and spectra of 60 nm AuNP dimers and (B) of 60 nm AgNP dimers. . One spectrum showing a peak at 2200  $\text{cm}^{-1}$  for the AuNP dimers, however there was no dimer structure found on the corresponding AFM image. AgNP dimers showed characteristic amorphous carbon Raman peaks (as was seen by Dr. Christian Heck).

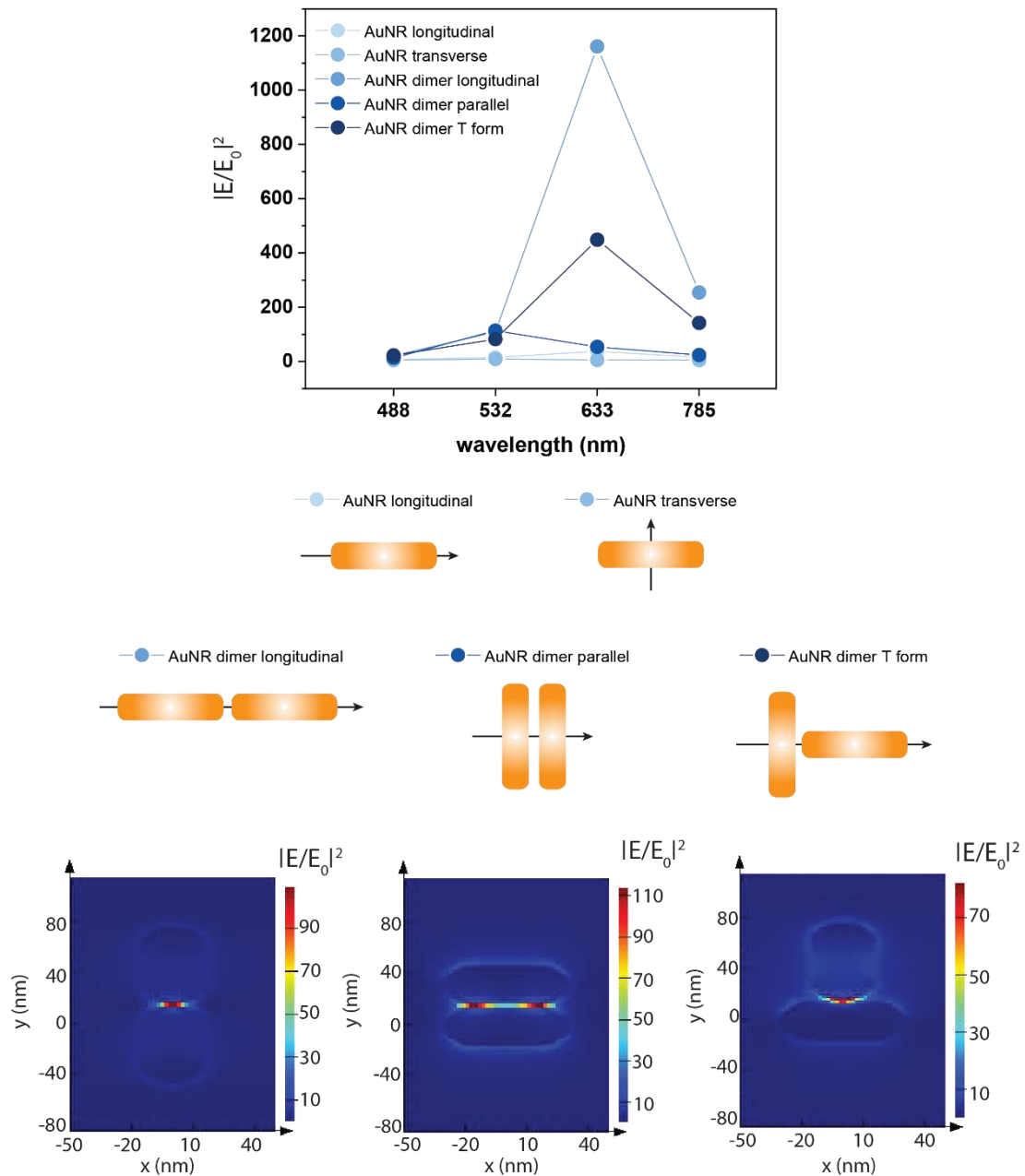


**Figure A.9.:** Electromagnetic field enhancement based on Finite difference time domain (FDTD) simulations at four different excitation wavelengths. Upper panel shows field enhancement at different excitation wavelengths (with dimer structures assembled with a 2 nm gap). Middle panel illustrates the excitation polarization along the structures. Bottom panel shows the three different dimer structures with excitation wavelength of 532 nm (longitudinal, parallel, and T form), with polarization along the y axis.

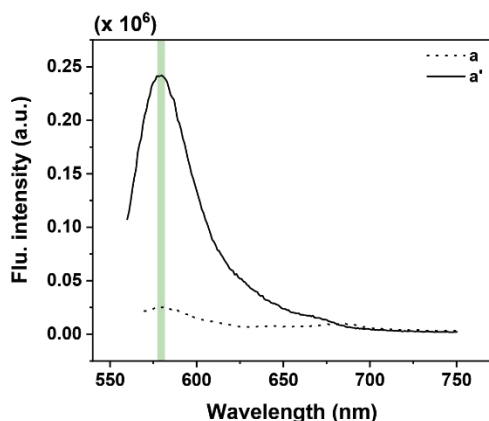


**Figure A.10.:** Fluorescence intensity of TAMRA labeled DNA (**a** and **a'**) after DTT treatment, releasing the surface bound dsDNA (DNA sequences listed in Figure 4.19). The Fluorescence intensity is much lower than for the other sequences (compared to an intensity maximum of  $54.2 \times 10^6$  for sequence **b'**), especially for sequence **a**. The spectra show that the coating the AuNR with these sequences are very inefficient.

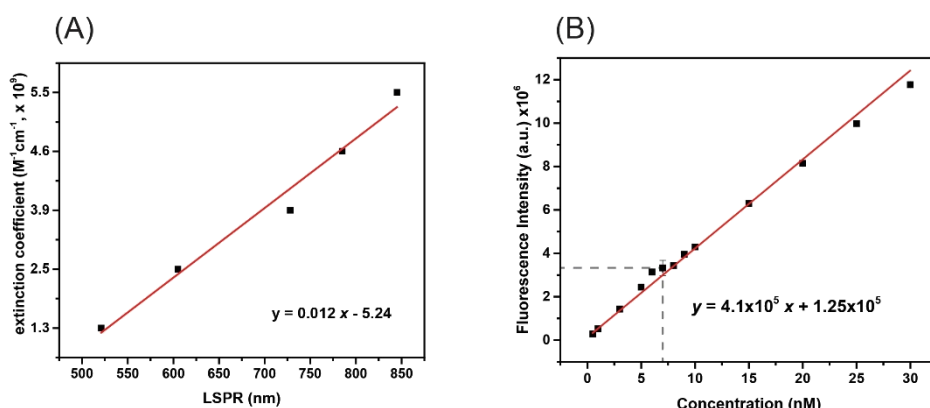


**Figure A.11.:** dsDNA coverage on AuNR. (A) Determined extinction coefficient according to the AuNR longitudinal LSPR. Using this, the concentration of the AuNR was determined. (B) After treating the dsDNA coated AuNR with DTT, fluorescence emission intensity at 580 nm was measured and plotted against the calibration curve ( $\lambda_{\text{exc}} = 540$  nm).

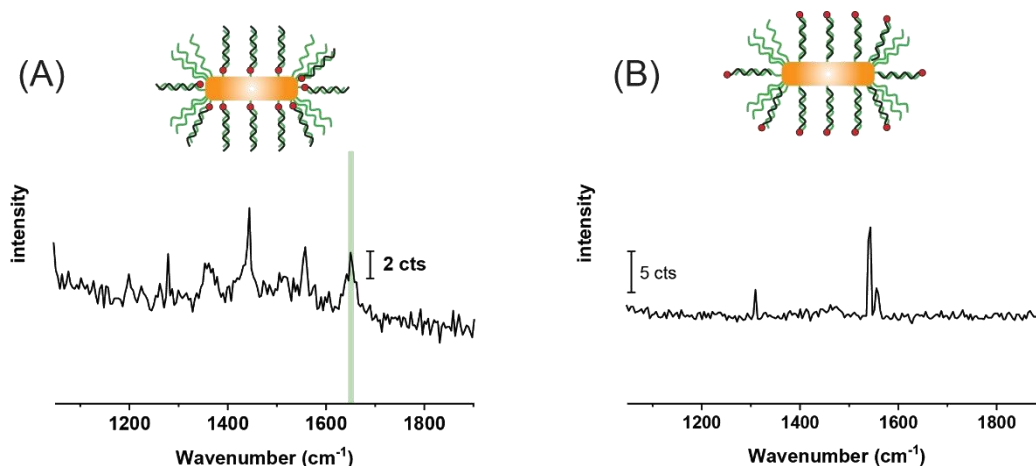


**Figure A.12.:** SERS spectra of dsDNA coated AuNR ( $\lambda_{\text{exc}} = 532$  nm, 30 s integration time, 10 accumulation). (A) AuNR coated with  $(\text{TTT})_8\text{T}_4\text{-SH}$  and hybridized with  $(\text{AAA})_7\text{A}_4\text{-(TAMRA)}$  showed characteristic TAMRA peak at  $1650\text{ cm}^{-1}$  (highlighted in green). (B) AuNR coated with  $(\text{ATT})_7\text{T}_7\text{-SH}$  and hybridized with  $(\text{TAMRA})\text{-(AAT)}_7\text{-A}_7$  showed no characteristic peaks for TAMRA.

**Table A.7.:** List of unmodified staple strands for the triangular DNA origami nanostructure.

<b>Staple name</b>	<b>Sequence (5' → 3')</b>
t 11s18h	AAT ACT GCG GAA TCG TAG GGG GTA ATA GTA AAA TGT TTA GAC T
t 11s28h	TCT TTG ATT AGT AAT AGT CTG TCC ATC ACG CAA ATT AAC CGT T
t 11s8h	CAG AAG GAA ACC GAG GTT TTT AAG AAA AGT AAG CAG ATA GCC G
t 1s10g	GAC GGG AGA ATT AAC TCG GAA TAA GTT TAT TTC CAG CGC C
t 1s12i	TCA TAT GTG TAA TCG TAA AAC TAG TCA TTT TC
t 1s14i	GTG AGA AAA TGT GTA GGT AAA GAT ACA ACT TT
t 1s16i	GGC ATC AAA TTT GGG GCG CGA GCT AGT TAA AG
t 1s18i	TTC GAG CTA AGA CTT CAA ATA TCG GGA ACG AG
t 1s20g	GAA TAC CAC ATT CAA CTT AAG AGG AAG CCC GAT CAA AGC G
t 1s22i	TCG GGA GAT ATA CAG TAA CAG TAC AAA TAA TT
t 1s24i	CCT GAT TAA AGG AGC GGA ATT ATC TCG GCC TC
t 1s26i	GCA AAT CAC CTC AAT CAA TAT CTG CAG GTC GA
t 1s28i	CGA CCA GTA CAT TGG CAG ATT CAC CTG ATT GC
t 1s2i	CGG GGT TTC CTC AAG AGA AGG ATT TTG AAT TA
t 1s30g	TTG ACG AGC ACG TAT ACT GAA ATG GAT TAT TTA ATA AAA G
t 1s4i	AGC GTC ATG TCT CTG AAT TTA CCG ACT ACC TT
t 1s6i	TTC ATA ATC CCC TTA TTA GCG TTT TTC TTA CC
t 1s8i	ATG GTT TAT GTC ACA ATC AAT AGA TAT TAA AC
t 2s11g	AGA AAA GCC CCA AAA AGA GTC TGG AGC AAA CAA TCA CCA T
t 2s13g	ACA GTC AAA GAG AAT CGA TGA ACG ACC CCG GTT GAT AAT C
t 2s15f	ATA GTA GTA TGC AAT GCC TGA GTA GGC CGG AG
t 2s17f	AAC CAG ACG TTT AGC TAT ATT TTC TTC TAC TA
t 2s1g	GAT AAG TGC CGT CGA GCT GAA ACA TGA AAG TAT ACA GGA G
t 2s21g	CCT GAT TGC TTT GAA TTG CGT AGA TTT TCA GGC ATC AAT A
t 2s23g	TGG CAA TTT TTA ACG TCA GAT GAA AAC AAT AAC GGA TTC G
t 2s25f	AAG GAA TTA CAA AGA AAC CAC CAG TCA GAT GA
t 2s27f	GGA CAT TCA CCT CAA ATA TCA AAC ACA GTT GA
t 2s3g	TTT GAT GAT TAA GAG GCT GAG ACT TGC TCA GTA CCA GGC G
t 2s5f	CCG GAA CCC AGA ATG GAA AGC GCA ACA TGG CT
t 2s7f	AAA GAC AAC ATT TTC GGT CAT AGC CAA AAT CA
t 3s10g	GTC AGA GGG TAA TTG ATG GCA ACA TAT AAA AGC GAT TGA G
t 3s14e	CAA TAT GAC CCT CAT ATA TTT TAA AGC ATT AA
t 3s16e	CAT CCA ATA AAT GGT CAA TAA CCT CGG AAG CA
t 3s18g	AAC TCC AAG ATT GCA TCA AAA AGA TAA TGC AGA TAC ATA A
t 3s20g	CGC CAA AAG GAA TTA CAG TCA GAA GCA AAG CGC AGG TCA G
t 3s24e	TAA TCC TGA TTA TCA TTT TGC GGA GAG GAA GG
t 3s26e	TTA TCT AAA GCA TCA CCT TGC TGA TGG CCA AC
t 3s28g	AGA GAT AGT TTG ACG CTC AAT CGT ACG TGC TTT CCT CGT T
t 3s30g	AGA ATC AGA GCG GGA GAT GGA AAT ACC TAC ATA ACC CTT C
t 3s4e	TGT ACT GGA AAT CCT CAT TAA AGC AGA GCC AC
t 3s6e	CAC CGG AAA GCG CGT TTT CAT CGG AAG GGC GA
t 3s8g	CAT TCA ACA AAC GCA AAG ACA CCA GAA CAC CCT GAA CAA A
t 4s11g	GCA AAT ATT TAA ATT GAG ATC TAC AAA GGC TAC TGA TAA A
t 4s13g	CGT TCT AGT CAG GTC ATT GCC TGA CAG GAA GAT TGT ATA A
t 4s15f	CAG GCA AGA TAA AAA TTT TTA GAA TAT TCA AC

t 4s17f GAT TAG AGA TTA GAT ACA TTT CGC AAA TCA TA  
t 4s1g TAG CCC GGA ATA GGT GAA TGC CCC CTG CCT ATG GTC AGT G  
t 4s21g GCG CAG AGG CGA ATT AAT TAT TTG CAC GTA AAT TCT GAA T  
t 4s23g GAT TAT ACA CAG AAA TAA AGA AAT ACC AAG TTA CAA AAT C  
t 4s25f TAG GAG CAT AAA AGT TTG AGT AAC ATT GTT TG  
t 4s27f TGA CCT GAC AAA TGA AAA ATC TAA AAT ATC TT  
t 4s3g TTT AAC GGT TCG GAA CCT ATT ATT AGG GTT GAT ATA AGT A  
t 4s5f CTC AGA GCA TAT TCA CAA ACA AAT TAA TAA GT  
t 4s7f GGA GGG AAT TTA GCG TCA GAC TGT CCG CCT CC  
t 5s10g GAT AAC CCA CAA GAA TGT TAG CAA ACG TAG AAA ATT ATT C  
t 5s14e TTA ATG CCT TAT TTC AAC GCA AGG GCA AAG AA  
t 5s16e TTA GCA AAT AGA TTT AGT TTG ACC AGT ACC TT  
t 5s18g TAA TTG CTT TAC CCT GAC TAT TAT GAG GCA TAG TAA GAG C  
t 5s20g AAC ACT ATC ATA ACC CAT CAA AAA TCA GGT CTC CTT TTG A  
t 5s24e AAT GGA AGC GAA CGT TAT TAA TTT CTA ACA AC  
t 5s26e TAA TAG ATC GCT GAG AGC CAG CAG AAG CGT AA  
t 5s28g GAA TAC GTA ACA GGA AAA ACG CTC CTA AAC AGG AGG CCG A  
t 5s30g TTA AAG GGA TTT TAG ATA CCG CCA GCC ATT GCG GCA CAG A  
t 5s4e CCT TGA GTC AGA CGA TTG GCC TTG CGC CAC CC  
t 5s6e TCA GAA CCC AGA ATC AAG TTT GCC GGT AAA TA  
t 5s8g TTG ACG GAA ATA CAT ACA TAA AGG GCG CTA ATA TCA GAG A  
t 6s15g ATA AAG CCT TTG CGG GAG AAG CCT GGA GAG GGT AG  
t 6s17f TAA GAG GTC AAT TCT GCG AAC GAG ATT AAG CA  
t 6s25g TCA ATA GAT ATT AAA TCC TTT GCC GGT TAG AAC CT  
t 6s27f CAA TAT TTG CCT GCA ACA GTG CCA TAG AGC CG  
t 6s5g CAG AGC CAG GAG GTT GAG GCA GGT AAC AGT GCC CG  
t 6s7f ATT AAA GGC CGT AAT CAG TAG CGA GCC ACC CT  
t 7s10g ATA AGA GCA AGA AAC ATG GCA TGA TTA AGA CTC CGA CTT G  
t 7s14e ATG ACC CTG TAA TAC TTC AGA GCA  
t 7s16e TAA AGC TAT ATA ACA GTT GAT TCC CAT TTT TG  
t 7s18g CGG ATG GCA CGA GAA TGA CCA TAA TCG TTT ACC AGA CGA C  
t 7s20g GAT AAA AAC CAA AAT ATT AAA CAG TTC AGA AAT TAG AGC T  
t 7s24e ACA ATT CGA CAA CTC GTA ATA CAT  
t 7s26e TTG AGG ATG GTC AGT ATT AAC ACC TTG AAT GG  
t 7s28g CTA TTA GTA TAT CCA GAA CAA TAT CAG GAA CGG TAC GCC A  
t 7s30g GAA TCC TGA GAA GTG TAT CGG CCT TGC TGG TAC TTT AAT G  
t 7s4e GCC GCC AGC ATT GAC ACC ACC CTC  
t 7s6e AGA GCC GCA CCA TCG ATA GCA GCA TGA ATT AT  
t 7s8g CAC CGT CAC CTT ATT ACG CAG TAT TGA GTT AAG CCC AAT A  
t 8s17g TAA TTG CTT GGA AGT TTC ATT CCA AAT CGG TTG TA  
t 8s27g CGC GAA CTA AAA CAG AGG TGA GGC TTA GAA GTA TT  
t 8s7g AGC CAT TTA AAC GTC ACC AAT GAA CAC CAG AAC CA  
t 9s10h TAT CTT ACC GAA GCC CAA ACG CAA TAA TAA CGA AAA TCA CCA G  
t 9s16e ACT AAA GTA CGG TGT CGA ATA TAA  
t 9s18g TGC TGT AGA TCC CCC TCA AAT GCT GCG AGA GGC TTT TGC A  
t 9s20h AAA GAA GTT TTG CCA GCA TAA ATA TTC ATT GAC TCA ACA TGT T  
t 9s26e ACC ACC AGC AGA AGA TGA TAG CCC



t 9s28g	TAA AAC ATT AGA AGA ACT CAA ACT TTT TAT AAT CAG TGA G
t 9s30h	GCC ACC GAG TAA AAG AAC ATC ACT TGC CTG AGC GCC ATT AAA A
t 9s6e	CCA TTA GCA AGG CCG GGG GAA TTA
t 9s8g	GAG CCA GCG AAT ACC CAA AAG AAC ATG AAA TAG CAA TAG C
t-10s17h	ACC AAC CTA AAA AAT CAA CGT AAC AAA TAA ATT GGG CTT GAG A
t-10s27h	AAC TCA CAT TAT TGA GTG TTG TTC CAG AAA CCG TCT ATC AGG G
t-10s7h	ACG ACA ATA AAT CCC GAC TTG CGG GAG ATC CTG AAT CTT ACC A
t-12s19h	CCT GAC GAG AAA CAC CAG AAC GAG TAG GCT GCT CAT TCA GTG A
t-12s29h	ACG TGG ACT CCA ACG TCA AAG GGC GAA TTT GGA ACA AGA GTC C
t-12s9h	TGC TAT TTT GCA CCC AGC TAC AAT TTT GTT TTG AAG CCT TAA A
t-1s10e	AGA GAA TAA CAT AAA AAC AGG GAA GCG CAT TA
t-1s12i	AGG GAT AGC TCA GAG CCA CCA CCC CAT GTC AA
t-1s14e	ATT TTC TGT CAG CGG AGT GAG AAT ACC GAT AT
t-1s14i	CAA CAG TTT ATG GGA TTT TGC TAA TCA AAA GG
t-1s16e	ATT CGG TCT GCG GGA TCG TCA CCC GAA ATC CG
t-1s16i	GCC GCT TTG CTG AGG CTT GCA GGG GAA AAG GT
t-1s18g	CGA CCT GCG GTC AAT CAT AAG GGA ACG GAA CAA CAT TAT T
t-1s18i	GCG CAG ACT CCA TGT TAC TTA GCC CGT TTT AA
t-1s20e	ACA GGT AGA AAG ATT CAT CAG TTG AGA TTT AG
t-1s22i	CGC GTC TGA TAG GAA CGC CAT CAA CTT TTA CA
t-1s24e	CAG TTT GAC GCA CTC CAG CCA GCT AAA CGA CG
t-1s24i	AGG AAG ATG GGG ACG ACG ACA GTA ATC ATA TT
t-1s26e	GCC AGT GCG ATC CCC GGG TAC CGA GTT TTT CT
t-1s26i	CTC TAG AGC AAG CTT GCA TGC CTG GTC AGT TG
t-1s28g	TTT CAC CAG CCT GGC CCT GAG AGA AAG CCG GCG AAC GTG G
t-1s28i	CCT TCA CCG TGA GAC GGG CAA CAG CAG TCA CA
t-1s2i	CCT TTT TTC ATT TAA CAA TTT CAT AGG ATT AG
t-1s30e	CGA GAA AGG AAG GGA AGC GTA CTA TGG TTG CT
t-1s4e	TTA TCA AAC CGG CTT AGG TTG GGT AAG CCT GT
t-1s4i	TTT AAC CTA TCA TAG GTC TGA GAG TTC CAG TA
t-1s6e	TTA GTA TCG CCA ACG CTC AAC AGT CGG CTG TC
t-1s6i	AGT ATA AAA TAT GCG TTA TAC AAA GCC ATC TT
t-1s8g	TTT CCT TAG CAC TCA TCG AGA ACA ATA GCA GCC TTT ACA G
t-1s8i	CAA GTA CCT CAT TCC AAG AAC GGG AAA TTC AT
t-2s11g	CCT CAG AAC CGC CAC CCA AGC CCA ATA GGA ACG TAA ATG A
t-2s13g	AGA CGT TAC CAT GTA CCG TAA CAC CCC TCA GAA CCG CCA C
t-2s15f	CAC GCA TAA GAA AGG AAC AAC TAA GTC TTT CC
t-2s17f	ATT GTG TCT CAG CAG CGA AAG ACA CCA TCG CC
t-2s1g	AAA ACA AAA TTA ATT AAA TGG AAA CAG TAC ATT AGT GAA T
t-2s21g	GCT CAT TTT TTA ACC AGC CTT CCT GTA GCC AGG CAT CTG C
t-2s23g	GTA ACC GTC TTT CAT CAA CAT TAA AAT TTT TGT TAA ATC A
t-2s25f	ACG TTG TAT TCC GGC ACC GCT TCT GGC GCA TC
t-2s27f	CCA GGG TGG CTC GAA TTC GTA ATC CAG TCA CG
t-2s3g	AGA GTC AAA AAT CAA TAT ATG TGA TGA AAC AAA CAT CAA G
t-2s5f	ACT AGA AAT ATA TAA CTA TAT GTA CGC TGA GA
t-2s7f	TCA ATA ATA GGG CTT AAT TGA GAA TCA TAA TT
t-3s10g	AAC GTC AAA AAT GAA AAG CAA GCC GTT TTT ATG AAA CCA A

t-3s14e GTT TTG TCA GGA ATT GCG AAT AAT CCG ACA AT  
t-3s16e GAC AAC AAG CAT CGG AAC GAG GGT GAG ATT TG  
t-3s18g TAT CAT CGT TGA AAG AGG ACA GAT GGA AGA AAA ATC TAC G  
t-3s20g TTA ATA AAA CGA ACT AAC CGA ACT GAC CAA CTC CTG ATA A  
t-3s24e TGT AGA TGG GTG CCG GAA ACC AGG AAC GCC AG  
t-3s26e GGT TTT CCA TGG TCA TAG CTG TTT GAG AGG CG  
t-3s28g GTT TGC GTC ACG CTG GTT TGC CCC AAG GGA GCC CCC GAT T  
t-3s30g TAG AGC TTG ACG GGG AGT TGC AGC AAG CGG TCA TTG GGC G  
t-3s4e GAT TAA GAA ATG CTG ATG CAA ATC AGA ATA AA  
t-3s6e CAC CGG AAT CGC CAT ATT TAA CAA AAT TTA CG  
t-3s8g AGC ATG TAT TTC ATC GTA GGA ATC AAA CGA TTT TTT GTT T  
t-4s11g AGG TTT AGT ACC GCC ATG AGT TTC GTC ACC AGG ATC TAA A  
t-4s13g AGC GTA ACT ACA AAC TAC AAC GCC TAT CAC CGT ACT CAG G  
t-4s15f TAG TTG CGA ATT TTT TCA CGT TGA TCA TAG TT  
t-4s17f GTA CAA CGA GCA ACG GCT ACA GAG GAT ACC GA  
t-4s1g GAG CAA AAG AAG ATG AGT GAA TAA CCT TGC TTA TAG CTT A  
t-4s21g GTT AAA ATT CGC ATT AAT GTG AGC GAG TAA CAC ACG TTG G  
t-4s23g GGA TAG GTA CCC GTC GGA TTC TCC TAA ACG TTA ATA TTT T  
t-4s25f AGT TGG GTC AAA GCG CCA TTC GCC CCG TAA TG  
t-4s27f CGC GCG GGC CTG TGT GAA ATT GTT GGC GAT TA  
t-4s3g ACA TAG CGC TGT AAA TCG TCG CTA TTC ATT TCA ATT ACC T  
t-4s5f GTT AAA TAC AAT CGC AAG ACA AAG CCT TGA AA  
t-4s7f CCC ATC CTC GCC AAC ATG TAA TTT AAT AAG GC  
t-5s10g TCC CAA TCC AAA TAA GAT TAC CGC GCC CAA TAA ATA ATA T  
t-5s16e AAC AGC TTG CTT TGA GGA CTA AAG CGA TTA TA  
t-5s18g CCA AGC GCA GGC GCA TAG GCT GGC AGA ACT GGC TCA TTA T  
t-5s20g ACC AGT CAG GAC GTT GGA ACG GTG TAC AGA CCG AAA CAA A  
t-5s26e TGC TGC AAA TCC GCT CAC AAT TCC CAG CTG CA  
t-5s28g TTA ATG AAG TTT GAT GGT GGT TCC GAG GTG CCG TAA AGC A  
t-5s30g CTA AAT CGG AAC CCT AAG CAG GCG AAA ATC CTT CGG CCA A  
t-5s6e GTG TGA TAA GGC AGA GGC ATT TTC AGT CCT GA  
t-5s8g ACA AGA AAG CAA GCA AAT CAG ATA ACA GCC ATA TTA TTT A  
t-6s13f ACA GAC AGC CCA AAT CTC CAA AAA AAA ATT TCT TA  
t-6s15c CGA GGT GAG GCT CCA AAA GGA GCC  
t-6s17f ACC CCC AGA CTT TTT CAT GAG GAA CTT GCT TT  
t-6s23f CGG CGG ATT GAA TTC AGG CTG CGC AAC GGG GGA TG  
t-6s25c TGG CGA AAT GTT GGG AAG GGC GAT  
t-6s27f TGT CGT GCA CAC AAC ATA CGA GCC ACG CCA GC  
t-6s3f TCC CTT AGA ATA ACG CGA GAA AAC TTT TAC CGA CC  
t-6s5c GTT TGA AAT TCA AAT ATA TTT TAG  
t-6s7f AAT AGA TAG AGC CAG TAA TAA GAG ATT TAA TG  
t-7s10g GCC AGT TAC AAA ATA ATA GAA GGC TTA TCC GGT TAT CAA C  
t-7s18g AAA ACA CTT AAT CTT GAC AAG AAC TTA ATC ATT GTG AAT T  
t-7s20g ACC TTA TGC GAT TTT ATG ACC TTC ATC AAG AGC ATC TTT G  
t-7s28g TTC CAG TCC TTA TAA ATC AAA AGA GAA CCA TCA CCC AAA T  
t-7s30g CAA GTT TTT TGG GGT CGA AAT CGG CAA AAT CCG GGA AAC C  
t-7s8g GCG CCT GTT ATT CTA AGA ACG CGA TTC CAG AGC CTA ATT T

t-8s15f	CGG TTT ATC AGG TTT CCA TTA AAC GGG AAT ACA CT
t-8s17c	GGC AAA AGT AAA ATA CGT AAT GCC
t-8s25f	TCT TCG CTA TTG GAA GCA TAA AGT GTA TGC CCG CT
t-8s27c	GCG CTC ACA AGC CTG GGG TGC CTA
t-8s5f	TTC TGA CCT AAA ATA TAA AGT ACC GAC TGC AGA AC
t-8s7c	TCA GCT AAA AAA GGT AAA GTA ATT
t-9s10g	ACG CTA ACG AGC GTC TGG CGT TTT AGC GAA CCC AAC ATG T
t-9s20g	TGG TTT AAT TTC AAC TCG GAT ATT CAT TAC CCA CGA AAG A
t-9s30g	CGA TGG CCC ACT ACG TAT AGC CCG AGA TAG GGA TTG CGT T
ts-rem1	GCG CTT AAT GCG CCG CTA CAG GGC
t-5s2e-t6s23c	TTA ATT AAT TTT TTA CCA TAT CAA A
t-7s4e-t8s25c	TTA ATT TCA TCT TAG ACT TTA CAA
t-9s6e-t10s27c	CTG TCC AGA CGT ATA CCG AAC GA
t-11s8e-t12s29c	TCA AGA TTA GTG TAG CAA TAC T
t-5s12e-t6s3c	TGT AGC ATT CCT TTT ATA AAC AGT T
t-7s14e-t8s5c	TTT AAT TGT ATT TCC ACC AGA GCC
t-9s16e-t10s7c	ACT ACG AAG GCT TAG CAC CAT TA
t-11s18e-t12s9c	ATA AGG CTT GCA ACA AAG TTA C
t-5s22e-t6s13c	GTG GGA ACA AAT TTC TAT TTT TGA G
t-7s24e-t8s15c	CGG TGC GGG CCT TCC AAA AAC ATT
t-9s26e-t10s17c	ATG AGT GAG CTT TTA AAT ATG CA
t-11s28e-t12s19c	ACT ATT AAA GAG GAT AGC GTC C

---

# Acknowledgements

Firstly, I would like to thank my supervisor Prof. Dr. Ilko Bald for his fantastic guidance during my doctoral work. With his expertise, assistance, and enthusiasm, I was able to navigate through this exciting and challenging time. I am very thankful to my second supervisor Dr. Ute Resch-Genger for her unlimited support as well as great discussions, always accompanied by delicious cookies. I would also like to thank Dr. Carsten Schmidt and Dr. Stefan Rödiger for the opportunity to work with VideoScan. I would like to thank Lisa Kotthoff for all the great work she did with regards to all the pH ratiometric sensing. I would also like to thank the Biophotonics group at BAM for stimulating discussions, especially regarding fluorescence analysis.

I would like to thank my graduate school (SALSA) for the scholarship as well as the Bundesanstalt für Materialforschung und –prüfung (BAM) and University of Potsdam for the finances, including the many conferences I was able to attend.

And of course without the wonderful OSCI group I would not have had such a great time over the past few years. I would like to especially thank Dr. Lydia Olejko for her many advice on working with FRET, Dr. Christian Heck for his many advice on working with the Raman microscope, Dr. Julia Prinz for the great discussions we had working with nanoparticles, Stefanie Vogel for the great support (including the harsh weekends we spent writing), Dr. Till Meiling, Dr. Robin Schürmann, and Kenny Ebel for the great scientific discussions. I would like to thank everyone for not only being colleagues but true friends whom I could share this experience with.

To my friends outside of the university, who stuck by my side through good and bad times, I would like to thank all of you. Thank you for keeping me laughing, bringing me baked goods, and reminding me to enjoy life.

I am also deeply thankful to my parents and Tom for their endless love and support. I am who I am because of you and I wouldn't have it any other way. Thank you for everything.

# Declaration

I declare that this thesis has been composed solely by myself and that it has not been submitted, in whole or in part, in any previous application for a degree. Except where states otherwise by reference or acknowledgement, the work presented is entirely my own.

Potsdam,

Youngeun Choi